



HAL
open science

Simultaneous measurements of velocity and temperature by non-intrusive optical methods in a complex geometry: Application to the upper plenum of the sodium cooled reactor ASTRID

Mira Chitt

► **To cite this version:**

Mira Chitt. Simultaneous measurements of velocity and temperature by non-intrusive optical methods in a complex geometry : Application to the upper plenum of the sodium cooled reactor ASTRID. Mechanics [physics.med-ph]. Université Paris Saclay (COmUE), 2019. English. NNT : 2019SACLS598 . tel-02534247

HAL Id: tel-02534247

<https://theses.hal.science/tel-02534247>

Submitted on 6 Apr 2020

HAL is a multi-disciplinary open access archive for the deposit and dissemination of scientific research documents, whether they are published or not. The documents may come from teaching and research institutions in France or abroad, or from public or private research centers.

L'archive ouverte pluridisciplinaire **HAL**, est destinée au dépôt et à la diffusion de documents scientifiques de niveau recherche, publiés ou non, émanant des établissements d'enseignement et de recherche français ou étrangers, des laboratoires publics ou privés.



Simultaneous measurements of velocity and temperature by non-intrusive optical methods in a complex geometry: Application to the upper plenum of the sodium cooled reactor ASTRID.

Thèse de doctorat de l'Université Paris-Saclay
Préparée à l'Université Paris Sud
et au CEA Cadarache

École doctorale n°579 Sciences mécaniques
et énergétiques, matériaux et géosciences

Spécialité de doctorat: Mécanique des fluides

Thèse présentée et soutenue à Cadarache, le 19/12/2019, par
Mira CHITT

Composition du Jury :

Chantal STAQUET Prof, Université Grenoble Alpes (– LEGI)	Président
Alexandre LABERGUE MCF, HDR, Université Lorraine (– LEMTA)	Rapporteur
Fabrice ONOFRI DR, Aix-Marseille Université (– CNRS)	Rapporteur
DAVID GUENADOU IR, CEA Cadarache (– DTN)	Examineur
Frédéric MOISY Prof, Université Paris Saclay (–FAST)	Examineur
Lionel ROSSI IR, HDR, Université Paris Saclay, CEA Cadarache, (– DTN)	Directeur de thèse
Nathalie MARIE IR, CEA Cadarache (– DTN)	Invité
Guillaume RICCIARDI IR, HDR, CEA Cadarache (– DTN)	Invité

Titre : Mesures simultanées non-intrusive de vitesse et température par méthode optique dans une géométrie complexe: application au collecteur chaud du réacteur refroidi au sodium ASTRID

Mots clés : Expériences, Mesure, Jets, Vitesse, Température et Fluorescence

Résumé: Des problématiques thermo-hydrauliques du plénum supérieur d'ASTRID ne peuvent être étudiés à partir du retour d'expérience des réacteurs et des simulations numériques puisque les codes de calcul ne permettent pas de modéliser ces problèmes avec une confiance suffisante.

Pour valider les approches numériques et la conception d'ASTRID, il a été identifié des besoins en maquettes expérimentales. La maquette MICAS représentative du plénum supérieur a été conçue à cette fin.

Pour valider les codes numériques, les champs de vitesse et de température sont très importants.

Si la mesure de champ de vitesse par PIV est fréquemment utilisée au LTHC, la méthode LASER Induced Fluorescence (LIF) a nécessité de développement et mise en œuvre. La fluorescence induite par laser consiste en l'émission spontanée de photons par les molécules d'un traceur, à la suite de l'absorption d'un rayonnement laser. Des expériences d'étalonnage de LIF à un colorant ont été réalisées pour étudier leur réponse en fluorescence. La LIF à deux colorants est très intéressante aussi. PIV et LIF à deux colorants sont appliquées sur une nouvelle installation expérimentale (géométrie complexe à deux jets) conçue pendant cette thèse afin de permettre une représentative de la maquette MICAS.

Title: Simultaneous measurements of velocity and temperature by non-intrusive optical methods in a complex geometry: Application to the upper plenum of the sodium cooled reactor ASTRID

Keywords: Experiments, Measurement, Jets, Velocity, Temperature and Fluorescence.

Abstract: Thermal hydraulic problems of the upper plenum of ASTRID cannot be studied from the feedback of the reactors and the numerical simulations since the codes do not make it possible to model these problems with a sufficient confidence.

To validate the numerical approaches and the design of ASTRID, needs have been identified for experimental models.

The representative MICAS model of the upper plenum has been designed for this purpose. To validate the numeric codes, the velocity and temperature fields are must be measured.

While PIV technique is frequently used at the LTHC, the LASER Induced Fluorescence (LIF) method required development and implementation.

The principle of LIF is based on the spontaneous emission of photons by the molecules of a tracer, as a result of the absorption of laser radiation. LIF calibration experiments with a dye were performed to study their fluorescence response. The LIF with two dyes is very interesting too. PIV and LIF with two dyes are applied on a new experimental installation (complex geometry with two jets) conceived during this thesis in order to allow a representative of the model MICAS.



*Dédié à ma mère et mon frère
à mon grand-père, tu me manques*

*Dedicated to my mom and my brother
To my grand-pa, I miss you*

ACKNOWLEDGEMENT

Three years of the thesis passed very quickly at CEA in Cadarache, yet I can still remember so many details. I am very grateful to the team I worked with, my supervisor David GUENADOU, my thesis director Lionel ROSSI, Guillaume RICCIARDI, Benjamin CARITEAU, Philippe AUBERT and Jean-Philippe DESCAMPS.

I am very thankful to my supervisor David, the mentor during this period. Thank you for being optimistic and always finding solutions to the problems we faced during the thesis. Thank you again for so many reasons, the advice you gave during the PhD, the technical assistance, the conference suggestions and attendances, the comments for my presentation skills and preparations, always checking if I'm still motivated. Thank you a lot for your support. It was really my honor working with you.

Lionel, thank you a lot for being always available when I had questions, thank you for your answers and suggestions. Thank you for your comments during the team meetings. I am very grateful to Guillaume for the detailed comments you gave during this period and for arranging the scientific meetings in the laboratory for the PhD students. Benjamin, thank you for your suggestions and your support during this period. It is with you that I started the first LIF experiments.

Philippe and Jean-Philippe, thank you a lot for your help during the experimental work. Philippe, I am grateful for your support especially during the PIV experiments and the software debugging. Jean-Philippe, thank you for your help in particular during the mechanical part in the experiments. Thank you both for always making me laugh even during the worst moments of our experiments. I learned from you that things are easy going, you are the best team anyone can work with. I will really miss passing by your office each morning laughing and saying our usual list of words and then going to spend the whole day at the experimental facility.

I am very thankful to all the workers in the two laboratories LTHC and LETH. You were my family during this period of time. I will never forget our morning coffee breaks, the funny chats, and our outings. A special thanks to Fabrice FRANCOIS for his support during the last year of my thesis. I would also like to thank Amine KOCHED and Jean STEFANINI from TSI Incorporate for their assistance during the optical setup installation of our experiments. I am also grateful to my colleagues at CEA and my friends.

Thanks to Alexandre LABERGUE for being a reporter for this thesis and thanks for the corrections and help after the thesis defense. Also, I would like to thank Fabrice ONOFRI his comments and the members of the jury Chantal STAQUET and Frédéric MOISY.

Finally, family is always my priority; my mother and my brother, I dedicate this work to you; you mean everything to me. You are the reason behind the motivation for this work. A thought for my grand father, who passed away during the second year of my thesis. This was your dream. I hope you were still alive to see it coming true.

*The best preparation for tomorrow is doing your
best today.*

H. Jackson BROWN

*La raison c'est la folie du plus fort.
La raison du moins fort c'est de la folie.*

Eugène IONESCO

*Progress is made by trial and failure;
The failures are generally a hundred times more
numerous than the successes; yet they are usually
left unchronicled.*

William RAMSAY

Résumé étendu

Cette section présente un résumé étendu en français du document suivant, rédigé en anglais.

Le développement économique mondial sera confronté à des problématiques de croissance significative des besoins en énergie, à l'épuisement progressif des ressources fossiles et à la logique de réduction des émissions de gaz à effet de serre. C'est pourquoi de nombreux pays souhaitent se tourner vers l'énergie nucléaire.

Les professionnels distinguent quatre générations de réacteurs à fission nucléaire. Chaque génération répondait à des objectifs liés aux enjeux majeurs de l'époque de leur conception.

La 4ème génération correspond aux réacteurs, actuellement en conception, qui pourraient voir un déploiement industriel à l'horizon 2040-2050. Les recherches sur ces systèmes du futur a établi les quatre critères auxquels ils devront répondre : la durabilité, la sûreté, la compétitivité économique et la résistance à la prolifération nucléaire. Dans ce contexte, le réacteur prototype ASTRID (Advanced Sodium Technological Reactor for Industrial Demonstration) devrait répondre aux critères précédents. ASTRID est de type réacteur rapide refroidi au sodium et porté par le CEA (Commissariat à l'énergie atomique et aux énergies alternatives).

Tout d'abord, les réacteurs à neutrons rapides sont capables d'utiliser de manière plus efficace la ressource en uranium et de recycler complètement le plutonium.

Ce qui concerne le choix du fluide, le sodium est un bon liquide de refroidissement. Il ne ralentit pas les neutrons et il a une bonne disponibilité industrielle. En plus, il y a une expérience de fond pour son utilisation en France. Dans le cadre des études de R&D pour le réacteur ASTRID certaines problématiques de thermohydraulique du collecteur chaud ne peuvent pas être validées uniquement à partir de simulations numériques et du retour d'expérience. Cela nécessite des expérimentations dans ce domaine.

Par contre, l'utilisation du sodium présente des inconvénients, en particulier au niveau de la sécurité et de la sûreté. La forte réactivité chimique avec l'eau, est susceptible de libérer de grandes quantités d'énergie si elle met en jeu des quantités de sodium importantes. Aussi dans le cadre d'expérimentations, le sodium présente également l'inconvénient d'être opaque.

En conséquence, un programme expérimental en similitude sur un fluide simulant (comme l'eau) a été mis en place sur des maquettes du collecteur chaud d'ASTRID. En particulier, la maquette MICAS, fabriquée à l'échelle 1/6 en matériau transparent (PMMA), a pour but de valider d'une part les approches numériques et d'autre part les concepts des composants et systèmes du collecteur chaud d'ASTRID. Les essais permettront de mieux comprendre les chargements thermiques associés aux phénomènes de fuites thermiques à la périphérie du cœur et de jets induit par le bouchon couvercle cœur. Les

phénomènes étudiés pouvant avoir un caractère transitoire il apparaît nécessaire de mesurer les champs de vitesse et de température simultanément.

L'objet de cette thèse est de mettre en œuvre un moyen de mesure optique pour répondre à ce besoin correspondant à l'étude simultanée des champs de vitesse et température dans les géométries complexes des maquettes en eau associées au projet ASTRID (maquette MICAS du collecteur chaud en particulier).

Pour atteindre cet objectif, les mesures doivent être effectuées en utilisant des techniques non intrusives (pour ne pas affecter le débit de fluide) et appliquées sur une maquette intermédiaire de deux jets (un chaud et un froid) qui présente le débit dans la maquette MICAS.

Le champ de vitesse sera mesuré par PIV (Particule Image Velocimetry) et cette technique a été utilisée avant dans notre laboratoire. D'une manière générale, la technique de PIV consiste à suivre le mouvement de traceurs dispersés dans le fluide.

Le champ de température pourra être obtenu par LIF (Laser Induced Fluorescence), une technique à mettre en œuvre à partir de zéro dans notre laboratoire. Dans ce cadre, le LIF doit être appliqué d'abord sur une géométrie simple puis sur la géométrie à échelle intermédiaire (entre la maquette simple et la maquette MICAS). La LIF consiste en l'émission spontanée de photons par les molécules d'un traceur, à la suite de l'absorption d'un rayonnement laser accordé sur une transition de l'espèce sondée. Un traceur fluorescent est utilisé pour absorber la lumière du laser et la réémettre vers un collecteur.

Comme première étape de notre démarche, la technique LIF a été appliquée (pour la première fois dans notre laboratoire) sur une géométrie simple de volume 30 L avec un laser Nd:YAG pulsé à 532 nm. Nous avons étudié la réponse de cinq colorants fluorescents: Fluorescéine classique, FL27, RhWT, Rh6G et Ch-Na. Ces colorants sont très solubles dans l'eau, leur spectre d'absorption est compatible avec une excitation à 532 nm et ils sont non toxiques.

Puisque le laser utilisé est pulsé, donc l'énergie peut rapidement être supérieure aux énergies de saturation des colorants fluorescents. Il existe trois régimes caractéristiques en fonction de l'intensité de l'excitation du laser:

- Régime linéaire où le signal de fluorescence est linéaire avec l'intensité d'excitation.
- Régime partiellement saturé où le signal de fluorescence ne dépend plus linéairement de l'intensité de l'excitation.
- Régime saturé où le signal de fluorescence ne dépend plus l'intensité de l'excitation.

En régime linéaire, il existe différentes atténuations subies par le signal de fluorescence sur le chemin optique. Donc, il faut connaître précisément la concentration des colorants et le coefficient d'absorption molaire des espèces présentes. Par contre, en régime saturé, seule la réabsorption de la fluorescence sur le chemin optique est à prendre en compte.

D'une manière générale, L'étude des colorants a été effectuée pour trouver la variation de leur réponse en fonction de la température. Dans ce cadre, trois types de comportements peuvent être observés:

- Les colorants dont l'intensité de fluorescence décroît avec la température
- Les colorants dont l'intensité de fluorescence croît avec la température
- Les colorants dont l'intensité est insensible à la température.

Le but était de trouver deux colorants adéquats pour la technique ratiométrique du LIF (2c/2d). Les principaux avantages de cette technique sont la correction des fluctuations de puissance du laser et l'absorption du colorant. Dans cette technique, il faut deux colorants de différents comportements.

Concernant les colorants sensible à la température, le FL27 et la fluorescéine classique ont montré une augmentation de leur réponse en fonction de la variation de température.

Nous avons obtenu un coefficient de sensibilité pour FL27 de $3.02\%/^{\circ}C$ à une concentration de $10^{-7}mol/L$. Nous avons également ré-appliqué la même expérience de la même solution de FL27 mais au bout de deux jours pour étudier son influence du vieillissement. Nous avons réalisé que les deux montrent une très bonne réponse en fonction de la variation de température mais celle de la première expérience est beaucoup plus stable que la deuxième. La raison derrière cela est la photo-dégradation du FL27 avec le temps; c'est pourquoi les expériences doivent être effectuées directement et la solution de fluorescéine doit être agitée fréquemment.

Pour la fluorescéine classique, le coefficient de sensibilité était de $3.38\%/^{\circ}C$ à une concentration de $10^{-4}mol/L$. La réponse de la fluorescéine classique était nulle à des concentrations plus faibles. Cette réponse est due à la composition de la fluorescéine classique qui dépend du pH. Cependant, dans nos expériences, nous ne pouvons pas ajouter de solutions chimiques qui peuvent stabiliser le pH car plus tard, nos expériences sont appliquées sur une géométrie complexe.

Les résultats étaient plus intéressants lors de l'utilisation de FL27 car il montre plus de stabilité dans les valeurs. Le FL27 a été choisi comme colorant dépendant de la température pour la technique LIF 2c/2d.

Concernant les colorants insensible à la température, nous avons étudié la réponse du Ch-Na et de deux rhodamines non toxiques: RhWT et Rh6G. Nous avons obtenu un coefficient de sensibilité pour Rh6G de $-0.56\%/^{\circ}C$ à une concentration de $10^{-5}mol/L$. Cependant, la réponse n'était pas stable lors de la variation de température. On remarque une diminution de cette réponse après $40^{\circ}C$. En ce qui concerne RhWT, la sensibilité du coefficient est de $-0.50\%/^{\circ}C$ à une concentration de $10^{-6}mol/L$. La réponse est approximativement stable pendant la variation de température même à des valeurs élevées. Pour Ch-Na, il ne montre aucune variation de sa réponse de fluorescence en fonction de la température. Cependant, la réponse est très faible, même à forte concentration. Nous avons augmenté la concentration à $10^{-5}mol/L$ jusqu'à ce que la couleur de la solution soit vert foncé. La sensibilité du coefficient était alors de $-0.36\%/^{\circ}C$. Les résultats les plus intéressants ont été ceux utilisant RhWT.

Ainsi, pour l'application de la technique LIF 2c/2d dans nos expériences, le couple de colorants choisi était FL27 et RhWT. Par contre,

Pour passer d'une géométrie simple (volume de 30 L) à une géométrie complexe (maquette MICAS), une maquette représentative à échelle intermédiaire a été conçue (TABOULE) au cours de la première année de thèse. Il se compose de deux jets dans lesquels il est possible de faire varier plusieurs paramètres pour étudier l'interaction entre différents écoulements de fluide. Deux campagnes expérimentales ont été réalisées sur TABOULE; une étude hydrodynamique et l'application simultanée de 2c/2d LIF et PIV pour les mesures simultanées de la température et de la vitesse.

Dans la première étude, nous avons utilisé un colorant fluorescent non réactif RhWT à une très faible concentration afin que l'écoulement ne soit pas affecté du fait de la présence du colorant. Le milieu d'expérimentation est illimité pour avoir les mêmes conditions de sortie. Quatre flux de fluides différents représentant ceux de MICAS ont été étudiés et comparés à la littérature. Nous avons comparé la propagation d'un seul et de deux jets flottants négatifs dans un milieu chaud. Le jet pénètre à sa hauteur maximale dans le milieu environnant, puis diminue et fluctue finalement autour d'une valeur moyenne de la hauteur maximale de pénétration. Les résultats que nous avons obtenus étaient comparables à ceux trouvés dans la littérature concernant les valeurs de la hauteur maximale de pénétration h_m et la largeur de l'écoulement de fluide b_j . Dans le cas de deux jets flottants négatifs, la hauteur maximale de pénétration du premier jet a diminué de moitié par rapport à la première expérience en raison de son interaction avec le second jet.

Ensuite, nous avons comparé deux cas; un jet flottant positif et neutre aux nombres de Reynolds bas et élevés. Trois phases de propagation ont été identifiées dans le cas d'un jet à flottabilité positive. Dans la région proche de la sortie de la buse, le momentum du jet domine et l'écoulement est similaire à un jet flottant neutre. Loin de la sortie du jet, la flottabilité domine et l'écoulement agit comme un panache. Cependant, la région intermédiaire est une transition entre le jet et le panache. Cependant, la deuxième et la troisième phase de propagation dépendent du débit d'injection qui affecte directement la force d'impulsion de la propagation. Par exemple, si le débit est faible, alors la force de flottabilité est dominante, de sorte que le débit agit comme un panache. Ce fut le cas dans la troisième expérience à faible nombre de Reynolds (2640). Cependant, si le débit est élevé, la quantité de mouvement est importante, de sorte que le débit est un certain jet à flottabilité positive. Ce fut le cas dans la quatrième expérience à haut nombre de Reynolds (14000).

Pour les mesures de température et de vitesse sur TABOULE; nous n'avons pas pu appliquer 2c/2d LIF et PIV sur tous les cas comme indiqué dans la campagne expérimentale. Leur application était possible dans le cas de jets flottants simples et de deux jets négatifs. Pour l'analyse du champ de vitesse, les vitesses moyennes dans le temps le long de la ligne médiane et de la direction axiale ont été tracées. Pour l'analyse du champ de température, la moyenne mobile de l'espace de la température le long de la ligne centrale de la buse a été tracée. Dans chaque cas, la diffusion des jets a été étudiée. Nous remarquons que la

variation de température est constante le long de la hauteur par rapport à celle de la vitesse qui diminue rapidement en raison de la compétition entre le moment et le flux de flottabilité. De plus, la technique LIF a été appliquée à quatre autres cas à différents nombres de Reynolds et Froude couvrant une gamme qui nous a permis de comparer nos résultats à ceux trouvés dans la littérature. Cependant, le calcul de la densité de puissance a montré que les manipes se situaient entre la régime partiellement saturé et la régime saturé. De plus, le système optique (filtres et miroirs) n'a pas évité les conflits spectraux entre les deux colorants. C'est pourquoi les résultats étaient biaisés. Ainsi, il était difficile de traiter efficacement les images. De plus, l'apparition de stries due à la variation de l'indice de réfraction a augmenté le niveau d'incertitude dans nos mesures. Cependant, la présence de stries est réduite lorsque la différence de température entre le fluide et l'environnement est faible. Cela peut expliquer pourquoi la qualité de l'image LIF est meilleure lorsque cette technique est utilisée pour une étude hydrodynamique. En conclusion, la complexité des expériences augmente avec l'augmentation de l'échelle de l'installation car nous devons contrôler et gérer de nombreux paramètres pour obtenir des résultats précis. Bien que nous ayons réussi à appliquer les mesures simultanées de température et de vitesse par LIF et PIV sur une géométrie complexe ($V = 1000$ L), la précision des résultats n'était pas élevée par rapport à celles effectuées sur des volumes inférieurs à 30 L. Cela montre la nécessité de travailler en régime saturé et d'utiliser un autre filtre qui évite le chevauchement entre l'absorption du FL27 et l'émission de RhWT.

Contents

1	General Introduction	25
1.1	Nuclear Reactors and their evolution over time	25
1.2	Fourth generation nuclear reactors	27
1.2.1	Different designs of reactors	27
1.2.2	Advantage of fourth generation fast reactors concerning uranium resources	28
1.2.3	Sodium-cooled fast reactor (SFR)	29
1.3	The ASTRID integrated technology demonstrator project	30
1.4	The Upper Plenum, MICAS Mock-up	32
1.4.1	Dimensional analysis between sodium and water	32
1.4.2	Design of MICAS Mock-up	33
1.5	Interest of the thesis subject	35
2	Literature Review	38
2.1	Non intrusive temperature measurement techniques	38
2.1.1	Thermo-chromic liquid crystals (TLC)	39
2.1.2	Laser Induced Fluorescence Technique (LIF)	39
2.2	Non-intrusive velocity measurement techniques	55
2.2.1	Introduction	55
2.2.2	Laser Doppler Velocimetry	55
2.2.3	Particle Image Velocimetry	57
2.3	Fluid dynamics and two jet flow study	61
2.3.1	Navier-Stokes equation and dimensionless numbers	61
2.3.2	Fluid Flows	64
2.3.3	Single and parallel jets	66
3	Protocols for optical methods: PIV & LIF	73
3.1	Functional Devices	73
3.1.1	Laser	73
3.1.2	Camera	74
3.2	Synchronizer and Software	75
3.3	Particles, dyes and optical filters	76
3.3.1	PIV Particles	76
3.3.2	Fluorescent dyes	78
3.3.3	Optical Filters	86
4	Experiments of LIF calibration on a simple geometry	90
4.1	Technical description of the simple geometry	90
4.2	The approach to measurements	91
4.3	Temperature dependent fluorescent dyes: Classical fluorescein and FL27	93

4.4	Temperature independent fluorescent dyes: Rh6G, RhWT and Ch-Na	98
4.5	Conclusion	99
5	TABOULE & OLYMPE Facility	101
5.1	Purpose of the facility	101
5.2	Construction of the facility	103
5.2.1	Geometry and specifications	103
5.2.2	Immersion heater and sensors	105
5.2.3	Pumps used in the facility	105
5.2.4	PID and notations	106
5.3	Functioning of the loop	108
6	Hydrodynamics and phenomenology of different fluid flows	111
6.1	Introduction and objectives	111
6.2	Initial conditions and calculations	114
6.3	Results	116
6.3.1	Experiment 1: Single negative buoyant jet at $Re = 2640$ and $Fr_d = -21.2$	117
6.3.2	Experiment 2: Two negative buoyant jets both at $Re_1 = 2640$, $Fr_{d1} = -21.2$ and $Re_2 = 3000$, $Fr_{d2} = -17.47$	119
6.3.3	Experiment 3: Positive and neutral buoyant jets at $Re_1 = 2640$ and $Re_2 = 4773$, $Fr_{d2} = 21.2$	121
6.3.4	Experiment 4: Positive and neutral buoyant jets at $Re_1 = 14000$ and $Re_2 = 25400$, $Fr_{d2} = 289$	122
6.4	Analysis and comparison with literature	124
6.4.1	Experiment 1: Single negative buoyant jet at $Re = 2640$ and $Fr_d = -21.2$	124
6.4.2	Experiment 2: Two negative buoyant jets both at $Re_1 = 2640$, $Fr_{d1} = -21.2$ and $Re_2 = 3000$, $Fr_{d2} = -17.47$	129
6.4.3	Experiment 3: Positive and neutral buoyant jets at $Re_1 = 2640$ and $Re_2 = 4773$, $Fr_{d2} = 21.2$	132
6.4.4	Experiment 4: Positive and neutral buoyant jets at $Re_1 = 14000$ and $Re_2 = 25400$, $Fr_{d2} = 289$	133
7	LIF and PIV on the complex geometry (TABOULE)	136
7.1	Installation of LIF & PIV and the complexities faced:	136
7.2	Experiments and processing of the results	140
7.2.1	The experimental protocol	140
7.2.2	The experimental matrix	141
7.2.3	Treatment of the LIF and PIV results	143
7.3	Experimental Results and analysis	149
7.3.1	PIV and LIF on a negative buoyant jet at $Re = 3930$ and $Fr_d = -24.5$	149
7.3.2	PIV and LIF on two negative buoyant jets at $Re = 5400$ and $Fr_d = -62.2$	155

7.3.3	LIF on a negative buoyant jet at $Re= 2000$ and $Fr_d= -6.72158$	
7.3.4	LIF on a negative and a neutral buoyant jets at $Re_1 = 2000$, $Fr_{d1} = -6.72$ and $Re_2 = 40000$, $Fr_{d2} = 2071$. . .	160
7.3.5	LIF on two negative buoyant jets at $Re= 2222$ and $Fr_d= -9.41$	165
7.3.6	LIF on a buoyant jet at $Re= 25555$ and $Fr_d= -1785$. . .	168
7.4	Conclusion	170
8	Conclusions and Perspectives	172
8.1	Summary and Conclusions	172
8.2	Perspectives	176

List of Figures

1	A nuclear reactor	26
2	Generations of nuclear reactors [1]	27
3	The sodium cooled fast design	30
4	Cut view of the ASTRID primary circuit [6]	31
5	The main issues of ASTRID [6]	32
6	The MICAS mock-up [6]	34
7	Cross-view of the MICAS mock-up [6]	34
8	Schematics of several liquid crystals phases [12]	39
9	Diagram illustrating the possible mechanisms of an excited electron [113]	41
10	Schematic diagram of the fluorescence intensity measurement [26]	43
11	The LIF setup	44
12	Basic laser principle	45
13	Absorption and emission spectra measured at 25°C (pH=5.6 for FL and pH=6.5 for RhB) [114]	47
14	Relative absorption and emission spectra of FL27 at 23°C [32]	48
15	Two color one dye technique [23]	49
16	Two color two dye technique [19]	51
17	Type I spectral conflict [18]	53
18	Type II spectral conflict [18]	54
19	Type III spectral conflict [18]	54
20	Laser Doppler Velocimetry principle	56
21	Set up of the PIV technique	57
22	Sketch of a self-similar turbulent jet [73]	66
23	Radial profiles of mean axial velocity in a turbulent round jet [73]	67
24	Schematic representation of a negative buoyant jet [76]	68
25	Variation of penetration height [76]	70
26	Sketch of an inclined buoyant jet (a) and a rosette buoyant jet (b) [83]	71
27	Overview of the test section and zoom on the jet slits and test plate [84, 85]	72
28	Nd:YAG Ever Green Laser	74
29	PowerView Cameras (TSI Incorporate)	74
30	The LASERPULSE synchronizer	75
31	The Timing Setup	76
32	PIV Particles	78
33	Molecular formula of Classical fluorescein	79
34	Absorption and emission spectra of classical fluorescein, based on [114]	80
35	Molecular formula of FL27	81
36	Absorption and emission spectra of FL27, based on [114]	81

37	Molecular formula of Rh6G	82
38	Absorption and emission spectra of Rh6G, based on [114]	83
39	Molecular formula of RhWT	83
40	Absorption and emission spectra of RhWT, based on [117]	84
41	Absorption and emission spectra of Ch-Na, based on [116]	85
42	Fluorescent dyes	86
43	The role of the filter	87
44	The LIF measurement facility on the simple geometry	90
45	Calibration facility	92
46	Transmission pass bands of the notch filter	93
47	Response of FL27 at temperature 59.2°C	94
48	Response of FL27, influence of aging	95
49	Response of FL27 at temperature 59.2°C	95
50	Response of classical fluorescein in three experiments	96
51	Normalized response of FL27	97
52	Normalized response of Classical fluorescein	97
53	Response of Rh6G as function of temperature	98
54	Response of RhWT and Ch-Na as function of temperature	99
55	The experimental facilities TABOULE & OLYMPE	103
56	Geometry of the test section	104
57	Specifications of the test section	105
58	PID of the test section	107
59	Test section TABOULE	108
60	Electrical Bay	109
61	The test section zoomed at the two nozzles	111
62	An experimental graph for different fluid flows	113
63	Variation of density of water as function of temperature (Engineering toolbox)	114
64	Variation of viscosity of water as function of temperature (Engineering toolbox)	115
65	Evolution of the negative buoyant jet	117
66	Evolution of the negative buoyant jet	118
67	Evolution of the two negative buoyant jets, part 1	119
68	Evolution of the two negative buoyant jets, part 2	120
69	Evolution of the two fluid flows	121
70	Evolution of the two fluid flows	122
71	Evolution of the two fluid flows	123
72	The jet penetration curve as function of time	125
73	Graph plotted along the x-axis at time 0.6 s, position red line	127
74	The time average over 75 images during the established phase	128
75	The lines indicate the position of graphs along the y-axis	129
76	Plot of values along the x-axis at positions 15 and 40 mm	130
77	Plot of values along the x-axis at positions 85 and 135 mm	130
78	Evolution of the two fluid flows at the centerline of each nozzle	131
79	Evolution of the two fluid flows	133
80	Evolution of the two fluid flows	134

81	Image on the left without a filter, image on the right with a filter	137
82	The setup of cameras and optics	138
83	Example of the reduced optical field of view for the second LIF camera	139
84	Emission and absorption spectra of dyes (FL27 and RhWT)	140
85	The processing procedure	143
86	Average reference images captured at 50°C	144
87	The calibration facility	144
88	Before and after calibration (to the left: first camera; to the right: second camera)	145
89	The results of calibration for each dye	147
90	The LIF and PIV time average field profiles	150
91	The plot of the time average velocity along different positions	151
92	The plot of the average velocity and its vertical component at position Y_B	152
93	The space moving average of temperature and the centerline velocity	153
94	The space moving average of temperature and the centerline velocity	154
95	LIF and PIV time average field profiles	155
96	The plot of the average velocity along different positions	156
97	The average time temperature profile along the centerline of the nozzle 1 and 2	157
98	The average time LIF image on a negative buoyant jet at $Re=2000$ and $Fr_d=-6.72$	158
99	The space moving average of temperature along the centerline of the nozzle 1	159
100	The time average LIF image on a negative and a neutral buoyant jets at $Re_1=2000$, $Fr_{d1}=-6.72$ and $Re_2=40000$, $Fr_{d2}=2071$	160
101	The space moving average of temperature along the centerline of nozzle 1	161
102	The space moving average of temperature along the centerline of nozzle 2	162
103	Plot of temperature profiles along the different positions Y_A	163
104	Plot of temperature profiles along the different positions Y_B	164
105	The time average LIF image on two negative buoyant jets at $Re=2222$ and $Fr_d=-9.41$	165
106	The space moving temperature profile along the centerline nozzle	1166
107	The space moving temperature profile along the centerline nozzle	2166
108	The time average LIF profile on a buoyant jet at $Re=25555$ and $Fr_d=-1785$	168
109	The temperature profile along the centerline of the nozzle 2	169

List of Tables

1	Specifications of different designs of reactors [1]	28
2	Physical properties of Sodium and Water	33
3	Table showing three types of spectral conflicts	52
4	Typical seeding PIV particles	58
5	Dimensionless numbers	64
6	Different fluid flows [115].	65
7	Characteristics of the cameras used	75
8	Emission spectra of dyes	87
9	The different facilities ASTRID, MICAS mock-up and TABOULE	102
10	Dimensions of the tanks	104
11	Symbols of the equipment used in this diagram	106
12	Experimental matrix with some parameters	116
13	Literature review	124
14	The experimental matrix of velocity and temperature measurements	142
15	Experimental values of jet width with height of penetration . . .	152
16	Summary of the results of experiments 7.3.1, 7.3.3 and 7.3.6 . . .	170

Nomenclature

List of Acronyms

ASTRID	Advanced Sodium Technological Reactor for Industrial Demonstration
ABWR	Advanced Boiling Water Reactor
IHTS	Intermediate Heat Transfer System
LWR	Light Water Reactor
LMFBR	Liquid Metal Fast Breeder Reactor
PHTS	Primary Heat Transfer System
PHWR	Pressurized Heavy Water Reactor
PMMA	Poly Methyl Methacrylate
SCWR	Super Critical Water Cooled Reactor
VHTR	Very High Temperature Reactor
CCD	Charge-Coupled Device
CMOs	Complementary Metal-Oxide Semiconductor
CEA	Commissariat a l'Energie atomique et eux Energie Alternatives
EPR	European Power Reactor
GFR	Gas Cooled Fast Reactor
IHX	Intermediate Heat Exchangers
LFR	Lead Cooled Reactor
LIF	Laser Induced Fluorescence
LPD	Laser Pulse Delay
MOX	Mixed Uranium and plutonium oxide
MSR	Molten Salt Reactor
PIV	Particle Image Velocimetry
PMT	Photo multiplier

RGB Red Green Blue
SFR Sodium Fast Cooled Reactor
SNR Signal to Noise Ratio
TKE Turbulent Kinetic Energy
TRL Technology Readiness Level
UCS Upper Core Structure
1c/1d LIF One color one dye Laser Induced Fluorescence
2c/1d LIF Two color one dye Laser Induced Fluorescence
2c/2d LIF Two color two dye Laser Induced Fluorescence
Fr Froude number
 Fr_d Discharge Froude number
Re Reynolds number
Ri Richardson number
Sc Schmidt number

Greek Symbols

α Molecular diffusivity ($\frac{cm^2}{s}$)
 β Thermal expansion coefficient ($\frac{1}{K}$ or $\frac{1}{C}$)
 ε Dissipation rate of turbulent kinetic energy ($\frac{m^2}{s^3}$)
 ε_1 Molar absorption coefficient of laser light ($L.mol^{-1}cm^{-1}$)
 ε_2 Molar absorption coefficient of fluorescence ($L.mol^{-1}cm^{-1}$)
 η Kolmogorov length scale
 λ Thermal conductivity ($\frac{W}{m.K}$)
 μ Dynamic viscosity ($\frac{kg}{m.s}$)
 ν Kinematic viscosity ($\frac{m^2}{s}$)
 ρ Density of the fluid ($\frac{kg}{m^3}$)
 φ Quantum efficiency

Latin Symbols

b	Laser path (m)
b_j	width of the jet (m)
b_u	width of the up flow (m)
B	Buoyancy flux ($\frac{m^4}{s^3}$)
C	Concentration (M: $\frac{mol}{L}$)
C_p	Specific heat ($\frac{J}{kg.K}$)
D	Diameter (m)
e	Fluorescence path (m)
F_B	Basset force (N)
F_{ext}	External forces (N)
g	Gravity ($\frac{m}{s^2}$)
g'	Reduced gravity ($\frac{m}{s^2}$)
h	Penetration height (m)
h_m	maximum height of penetration (m)
H	Height scale
I_f	Fluorescence intensity ($a.u$)
$I_{f,1}$	Fluorescence intensity of dye 1 ($a.u$)
$I_{f,2}$	Fluorescence intensity of dye 2 ($a.u$)
I_0	Incident intensity of laser beam ($a.u$)
K_{opt}	Optical calibration constant
L_B	Batchelor scale
M	Momentum flux ($\frac{m^4}{s^2}$)
p	Pressure ($bars$)
Q	Flow rate ($\frac{m^3}{s}$)
r	Radial distance & radius of nozzle (m)
R	Ratio

s Sensitivity coefficient ($\%/^{\circ}C$)
T Temperature ($^{\circ}C$)
T' Time scale
U Velocity ($\frac{m}{s}$)
U_g Falling velocity of PIV particles ($\frac{m}{s}$)
u Velocity profile for jet study ($\frac{m}{s}$)
*X** Dimensionless quantity
V_c Collection volume

Indices (Subscripts and superscripts)

0 Initial or input
1 first jet
2 second jet
 $\frac{1}{2}$ half width
a ambient
e surrounding
f fluid
j jet
p particle
u up flow

SUMMARY

Many countries worldwide have recognized the importance of clean emission-free nuclear energy due to the fast increase in energy demand. Thus, a huge effort is given for researches and experiments in this field to achieve as possible a compromise between the technical parameters such as production efficiency, cost and safety in nuclear reactor's technology. This thesis is a part project of the development of a fast neutron reactor cooled by sodium. It is a fourth generation nuclear pool type reactor having advantages of saving uranium resources and of course meeting the worldwide increase for energy demand. From the state of art of the past and foreign reactors, issues have been identified. The numerical codes can't address some of them with a sufficient level of confidence. Thus, a model is needed. A dimensional analysis was done between sodium and water regarding the numbers of Reynolds, Richardson and Froude. Also, the similitude between water and sodium in terms of physical properties encourages the usage of a water model. Due to the optical access in water models, optical measurement techniques using laser can be implemented. This is a big advantage in such cases since optical methods are known to have a good accuracy in measurements. Temperature and velocity field measurements are important to validate the numerical approach. Temperature measurements were done using thermocouples on the model but this approach is intrusive and punctual. So, a non-intrusive method is preferred and it is Laser Induced Fluorescence (LIF). In all forms of LIF, a laser is used to excite a fluorescent species within the flow. Typically, the tracer, an organic fluorescent dye such as Fluorescein or Rhodamine, absorbs a portion of the excitation energy and spontaneously re-emits a portion of the absorbed energy as fluorescence. Regarding velocity measurements, Particle Image Velocimetry was implemented. In this technique, the fluid is seeded with tracer particles then illuminated so that particles are visible. The motion

of the seeding particles is used to calculate speed and direction of the flow being studied. The goal of the thesis is to implement and develop the simultaneous application of LIF and PIV on a complex geometry to accomplish a thermal hydraulic study of the different phenomenology present. Through a survey in literature, the LIF technique is limited to simple volume geometries (less than 30 Liters) and not so many experiments were done on a huge volume due to the complexities that arise in a large scale facility. In this work, we present the experiments done using LIF and PIV measurement techniques on a large scale geometry (1000 Liters). This geometry consists of two jets separated by 5cm, several parameters were varied to study different cases such as the injection flow rate and temperatures. The following is a simple description of each chapter followed by a sketch that summarizes the thesis objectives and methodology.

Chapter 1, General Introduction: This chapter is a general introduction about nuclear reactors, their evolution passing to the fourth generation of nuclear reactors. Then, a part is dedicated to the water model MICAS mock up to end up by the interest of the thesis subject.

Chapter 2, Literature review: This chapter is dedicated to bibliography and analysis done during the thesis. It features non intrusive optical techniques for measurements of temperature and velocity. It is divided into three parts. The first is dedicated to non intrusive temperature measurement techniques, the second to non intrusive velocity measurement techniques and the last part is dedicated to two jet flow analysis by showing most of the articles done in this field.

Chapter 3, Protocols for optical measurements: This chapter presents in details the protocols of velocity

and temperature measurements by PIV and LIF respectively. It shows all the devices, explains the role of each device and its compatibility with the conditions in our experiments.

Chapter 4, Experiments of LIF on a simple geometry: This chapter is dedicated to show the calibration experiments of LIF done using several fluorescent dyes on a small volume. It presents the variation of fluorescence of each dye as function of temperature variation. Some dyes have a positive response and others are temperature independent. It then ends by a conclusion concerning the couple of dyes chosen for the experiments on the complex geometry.

Chapter 5, TABOULE & OLYMPE facility: This chapter is dedicated to show the experimental facility that was constructed on which the simultaneous measurements of temperature and velocity by LIF and PIV respectively were applied. It focuses on the concept of the facility, the reason behind it, the materials and equipment used and shows in details all the geometrical specifications.

Chapter 6, Hydrodynamics and phenomenology of different fluid flows: In chapter 6, experiments and results are shown concerning different fluid flows and the interaction between two injections. It is a hydrodynamic study based on visual analysis using a dye that does not respond to temperature.

Chapter 7, LIF and PIV on a complex geometry (TABOULE): LIF and PIV methods are applied on the complex test section. In this chapter, difficulties of passing from a simple geometry to a complex one are explained, the experimental matrix is shown and the results are analyzed.

Chapter 1

General Introduction

1 General Introduction

This chapter presents a general introduction related to the field of nuclear reactors. It is divided into several sections to approach the thesis subject.

1.1 Nuclear Reactors and their evolution over time

This paragraph discusses several points starting with nuclear fission, nuclear reactors, their components and then their evolution in terms of generations. In fact, when an atom undergoes fission, it releases a large amount of energy which is transformed into heat. In a nuclear reactor, this heat is recovered to generate electricity. So neutrons are consumed and created during fission. Before getting into details, it is important to know that low energy neutrons are thermal, high energy neutrons are fast and that fission neutrons are born fast. That's why reactors were divided into either thermal or fast neutron reactors [1].

Figure 1 shows a nuclear reactor with some components such as the fuel, the control rods and the coolant. These are mainly the common components found in the core of neutron reactors. In addition to these, a moderator is usually added to a thermal neutron reactor to reduce the speed of the neutrons. In fact, as a result of the fission reactions of thermal neutrons, another neutrons are produced which typically escape from participating in another fission reactions. This is where the moderator slows down their speed so they can trigger multiple fission reactions. However, fast reactors keep their neutrons moving quickly. That is why they don't contain a moderator. Actually, they get more neutrons out of their primary fuel in comparison with thermal reactors. This is an advantage of fast reactors over thermal neutron reactors [2].

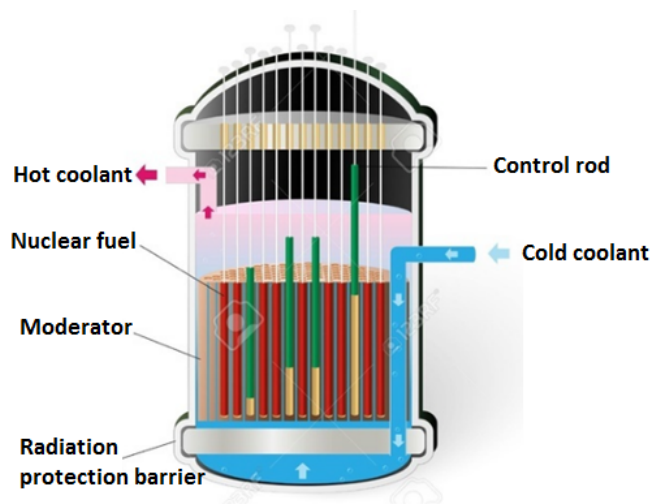


Figure 1: A nuclear reactor

Concerning the common components, the fuel usually used is Uranium. It contains fissile atoms whose energy is extracted by fission. It is inserted into fuel rods when pressed into pellets. These rods are then bundled together to form a fuel assembly which is placed in the core of the reactor. The control rods are used to trap neutrons so that the nuclear chain reaction taking place within the reactor core can be slowed down or stopped completely. Finally, the coolant which can be water, a liquid metal (sodium or lead) or a gas (carbon dioxide or helium) is used to transport heat during the fission of uranium nuclei which must be transferred from the reactor core to the systems designed to transform heat into electricity. This is a general explanation about the main components found in nuclear reactors. But these reactors were enhanced over time to correspond to specific requirement criteria. This is where the notion 'generation' comes from. Four generations of nuclear reactors have been defined as shown in figure

2. For instance, most of the reactors currently in service are second generation, while the third generation is only just starting to be deployed, and the fourth generation has just reached design phase.

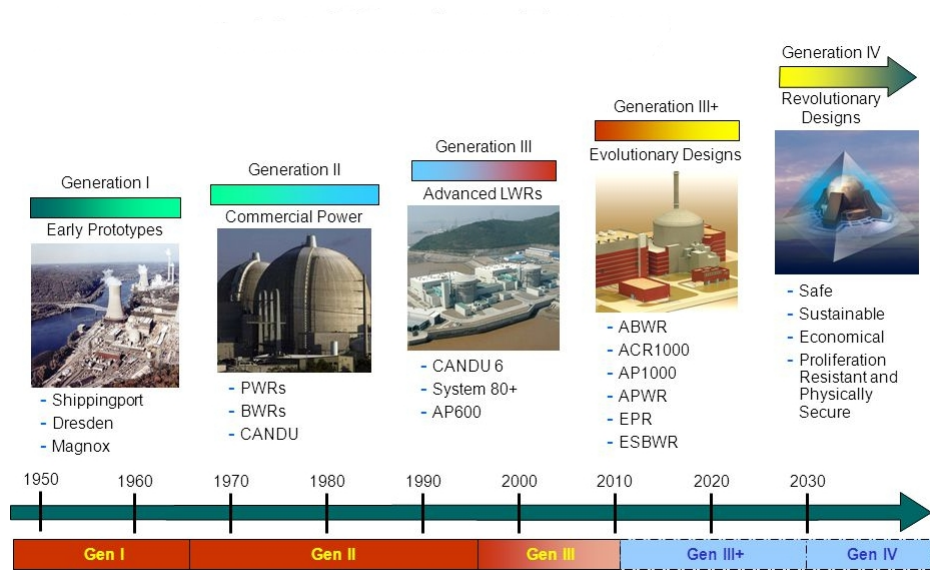


Figure 2: Generations of nuclear reactors [1]

The first generation included the first industrial prototypes, the second focused on energy independence in times of oil crisis whereas the third focused on safety and security requirements. But it is in the fourth generation where several criteria have been defined to be met such as sustainability, nuclear safety, waste minimizing and economic competitiveness. That is why huge effort is given to researches in this field since their design incorporates a number of technological breakthroughs with respect to what has been built so far.

1.2 Fourth generation nuclear reactors

This part is dedicated to explain the several designs of fourth generation reactors, their advantages and ends up by a detailed study about the choice of sodium fast reactors among others in France.

1.2.1 Different designs of reactors

Several reactor designs were selected at the outset. To better understand the differences between them, they are summarized in the table 1 including information

on the type of the reactor, coolants, and approximate core outlet temperatures.

Type	Neutron spectrum	Coolant	Temperature (°C)	Pressure	Fuel	Fuel cycle
Gas cooled fast reactors	Fast	Helium	850	High	U-238	Closed, on site
Lead cooled fast reactors	Fast	Lead or Lead-Bismuth	480-800	Low	U-238	Closed, regional
Molten salt fast reactors	Fast	Fluoride salts	700-800	Low	UF in salt	Closed
Molten salt reactor (Advanced high temperature reactors)	Thermal	Fluoride salts	750-1000	Low	UO ₂	Open
Sodium cooled fast reactors	Fast	Sodium	550	Low	U-238 & MOX	Closed
Traveling wave reactors	Fast	Sodium	510	Low	U-238 metal with U-235 igniter seed	Open
Supercritical water cooled reactors	Thermal or Fast	Water	510-625	Very high	UO ₂	Open
Very high temperature gas reactors	Thermal	Helium	900-1000	High	UO ₂ prism or pebbles	Open

Table 1: Specifications of different designs of reactors [1]

As seen, regarding neutron spectrum, reactors are divided between either fast or thermal reactors and the difference between the two is explained in section one. An interesting parameter is the core outlet temperature. In comparison with other reactors, gas reactors are characterized by the temperature reached which is minimum 850°C. This is in fact due to the material of the coolant used. When analyzing the table, it is shown the coolant chosen for gas reactors is Helium which is a single phase and an inert gas approaching more safety side. But the drawbacks of a gas are its low density and low calorific value. Now regarding the parameter fuel cycle, it consists of the several activities associated with the production of electricity from nuclear reactions starting with the mining of uranium and ending with the disposal of nuclear waste. So if spent fuel is not reprocessed, the fuel cycle is referred to as an open fuel cycle. It is a closed fuel cycle if the spent fuel is reprocessed. Most of the 4th generation reactors have a closed fuel cycle which contributes to lower mining and waste minimizing.

1.2.2 Advantage of fourth generation fast reactors concerning uranium resources

In fact, Fourth generation fast reactors have the advantage of saving on uranium resources and recycling recoverable materials, plutonium in particular.

Uranium-235, a fuel used in most reactors and a minor isotope of natural uranium is exploited to produce energy. In France, the stocks of Uranium currently amount to more than 270,000 tonnes according to a statistical study done by CEA (Commissariat à l'énergie atomique et aux énergies alternatives) [5]. This is due to a policy adopted by France in which 8,000 tonnes of natural uranium are imported yearly divided into 1,000 tonnes of enriched uranium to supply the power plants and the remainder 7,000 tonnes of depleted uranium stored for future use in fourth generation reactors. Additionally, materials like uranium and plutonium which are recovered from spent fuel produced by the current fleet are treated and can be recycled into fuel called MOX (Mixed uranium and plutonium oxide). This kind of fuel can be used efficiently in sodium fast cooled reactors (shown in Table 1).

Fast reactors can burn all of the natural uranium (including depleted uranium) whereas today's reactors only burn less than 1%. By utilizing all of the uranium in the core, fast reactors multiply the energy that can be extracted from a given mass of natural uranium by a factor of about 100. Thus, they could operate for several thousand years dispensing entirely with natural uranium. This is a general sum up of the evolution in the generations of nuclear reactors focusing more on the advantages of the fourth generation reactors. The CEA studied the advantages and drawbacks of these different reactors and stated that sodium and gas cooled fast reactors are the most promising ones. However, France has acquired a lot of knowledge regarding sodium cooled technology owing to the operation of the reactors Phénix and Superphénix. Thus, the preferred coolant is sodium over gas because of available data due to experiences over the past 40 years in such a field. So the next paragraph is dedicated to sodium cooled fast reactors.

1.2.3 Sodium-cooled fast reactor (SFR)

SFRs generally have three heat transfer systems, PHTS (Primary Heat Transfer System), IHTS (Intermediate Heat Transfer System) and energy conversion system. The PHTS has a role of cooling the core and the IHTS for transferring heat from the primary loop to the steam generator. They are both kept at low pressure (near ambient) since the boiling point of Na (882°C) is significantly higher than normal operational temperatures (550°C). The energy conversion system generates electricity with a turbine.

A SFR is divided into two main configurations: loop design and pool design. In the loop design, the primary coolant is allowed to leave the reactor vessel, and the IHX (Intermediate heat exchanger) is located in the containment area outside the vessel whereas in the pool design, the primary coolant is kept within the reactor vessel which also encompasses the intermediate heat exchangers. This reactor shown in figure 3 is supposed to be the reference technology for fourth generation systems in France.

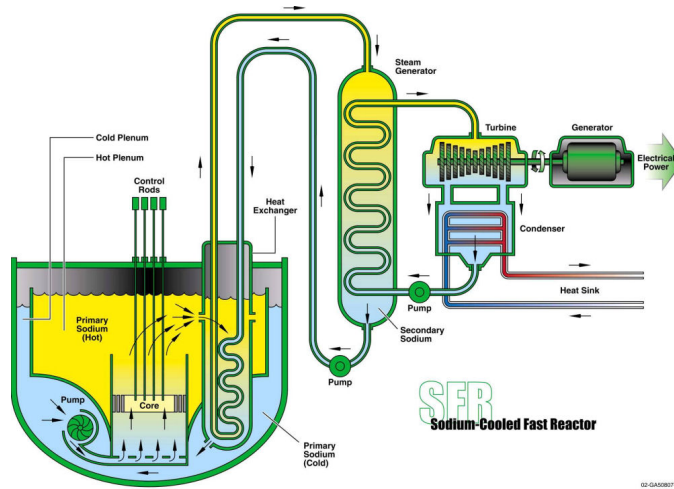


Figure 3: The sodium cooled fast design

1.3 The ASTRID integrated technology demonstrator project

In France, the experience accumulated from fast reactors has led to the technology demonstrator project of fourth generation called ASTRID (Advanced Sodium Technological Reactor for Industrial Demonstration). It is a pool type reactor designed by the CEA and its current design is shown in figure 4. ASTRID is the successor of the three French fast reactors Rapsodie, Phénix and Superphénix. The main goals of ASTRID are the multi-recycling of plutonium aiming at preserving natural uranium resources, minor actinide transmutation, reducing nuclear waste and an enhanced safety comparable to generation III reactors as previously explained.

This paragraph explains the design options of ASTRID starting from the fuel used ending by a brief explanation of its primary circuit. Due to the wide experience feedback in France on the oxide fuel, the reference fuel chosen for ASTRID is mixed oxide (U, Pu) O_2 . Sodium is used as a coolant and is maintained in one main vessel to reduce the risk of primary sodium leakage. From figure 4, the sodium flows from the external vessel to the upper plenum through the core where it is heated. Then around 90% of the sodium ejected from the core is deviated by the UCS (Upper Core Structure) to the upper plenum. The UCS due to its position sustains the control rods and drives sodium coolant toward the core in normal and accidental conditions. The other part flows across the UCS, then to the upper plenum. The hot sodium (550°C) of the upper plenum enters inside the IHX (Intermediate Heat Exchangers) to heat a secondary sodium circuit. This latter is connected to a steam generator. Such a scheme avoids the primary sodium to be in contact with water in case of leakage.

The outlet of the IHX is connected to the external vessel where the sodium is pumped and sent back to the core.

After this brief description, it is essential to state that there are main issues about this design as shown in figure 5. For instance, the oscillation of the surface flow can induce thermal oscillations on the Upper Core Structure and the heat exchangers. This can damage them by thermal fatigue. The other problems also identified for the upper plenum cannot be studied using numerical codes with enough confidence. Experiments should be carried out on a reduced scale mock-up to supply the validation data necessary for the numerical codes. The next section addresses the design of this mock-up in details.

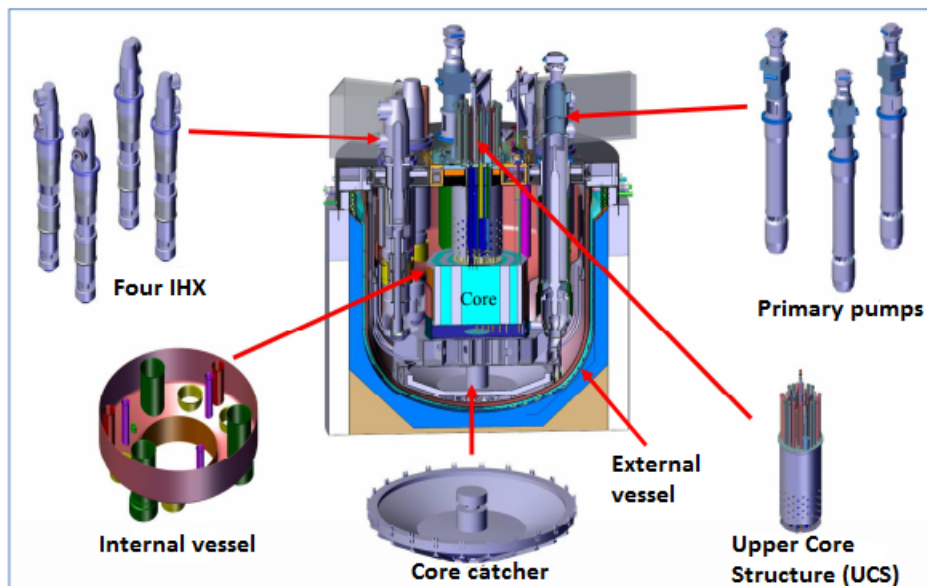


Figure 4: Cut view of the ASTRID primary circuit [6]

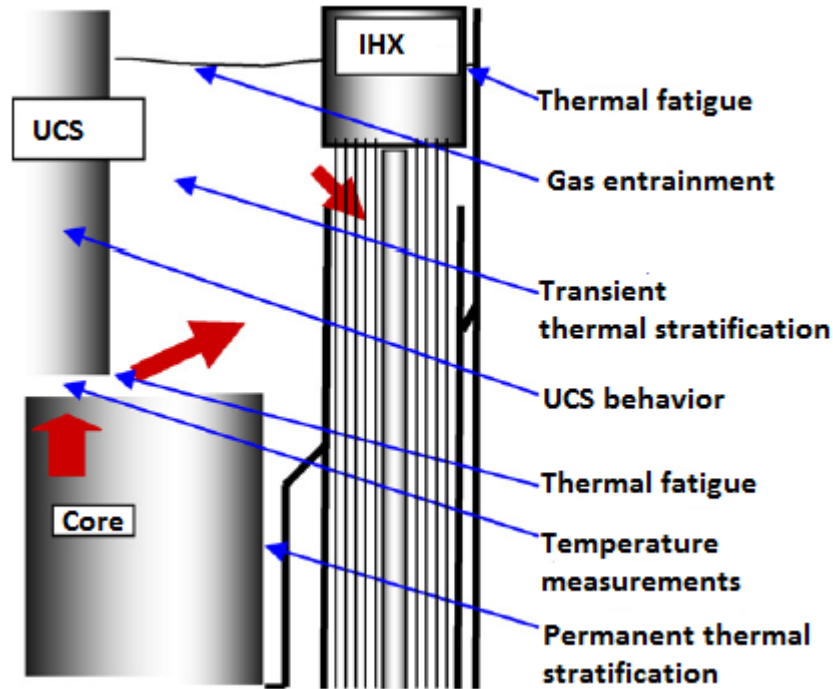


Figure 5: The main issues of ASTRID [6]

1.4 The Upper Plenum, MICAS Mock-up

The upper plenum of ASTRID cannot be studied from past reactors feedback and numerical simulations since the calculation codes do not allow to model these problems with sufficient confidence. Thus, in order to validate the numerical approaches and systems concept of ASTRID and to increase its TRL (Technology Readiness Level), experiments are needed. In terms of practice, sodium experiments are very complicated to perform since sodium is opaque and reacts with water. This part shows why water is chosen to implement the experiments and to validate the codes. It presents the dimensional analysis and shows the design of the MICAS mock-up.

1.4.1 Dimensional analysis between sodium and water

In terms of physical properties, both sodium and water are similar since they have approximately same viscosity and density at certain operating conditions as shown in table 2. Thus, we can study the hydraulic effects concerning the dimensionless numbers. The thermal conductivity in sodium is high compared

to that of water. So, the thermal effects such as the conduction at the walls cannot be studied however it is possible to study the effects of buoyancy.

Physical Properties	$\rho(kg/m^3)$	$\mu(10^{-7}m^2/s)$	$\lambda(W/m.K)$	$C_p(J/kg.K)$
Sodium at 550°C	845	3	69	1270
Water at 20°C	998	10	0.6	4180

Table 2: Physical properties of Sodium and Water

In such a case where sodium and water have the same physical properties, a reduced scale water mock-up can be used. This will give calculations of the operating conditions using dimensionless numbers.

1.4.2 Design of MICAS Mock-up

The MICAS mock-up is made up of PMMA (Poly methyl methacrylate) for optical measurements. Its size is 2.5 m diameter and 1.7 m height and the scale is 1/6 the ASTRID reactor (figure 6). This mock-up is built to study several issues such as free surface flow state due to the wake of the immersed components. The core is divided in three zones. The injection room is shown at the bottom of figure 7; the central zone corresponds to the core at high temperature (yellow zone); the intermediate one is related to the reflector; and the external zone represents the internal fuel assembly storage. These two external zones are supplied with low temperature water. However, the optical access in this geometry faces deformation due to the refractive index between the several mediums present. Thus, the mock-up is placed in an external vessel made up of plane walls. This enhances the optical access and increases the accessible laser domain. Such approach facilitates the measurements (temperature, velocity, ..) using optical techniques.

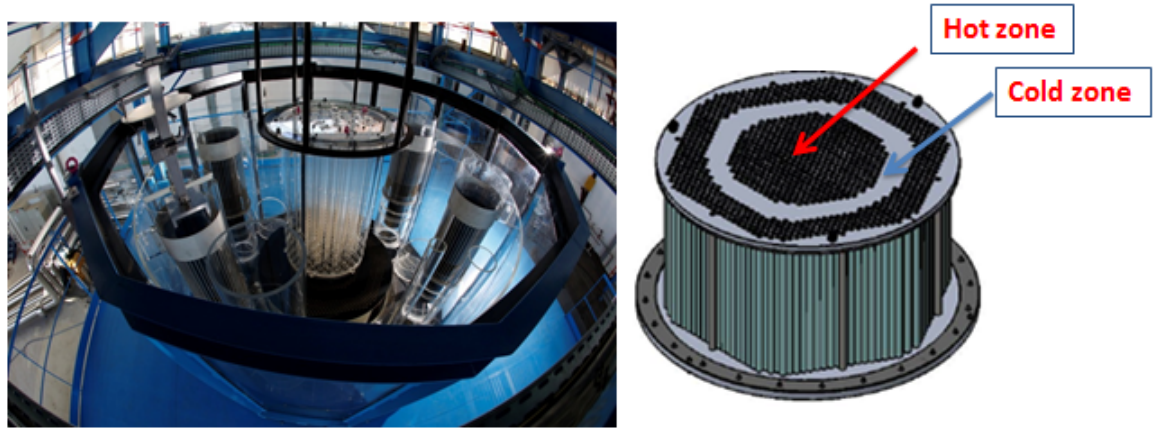


Figure 6: The MICAS mock-up [6]

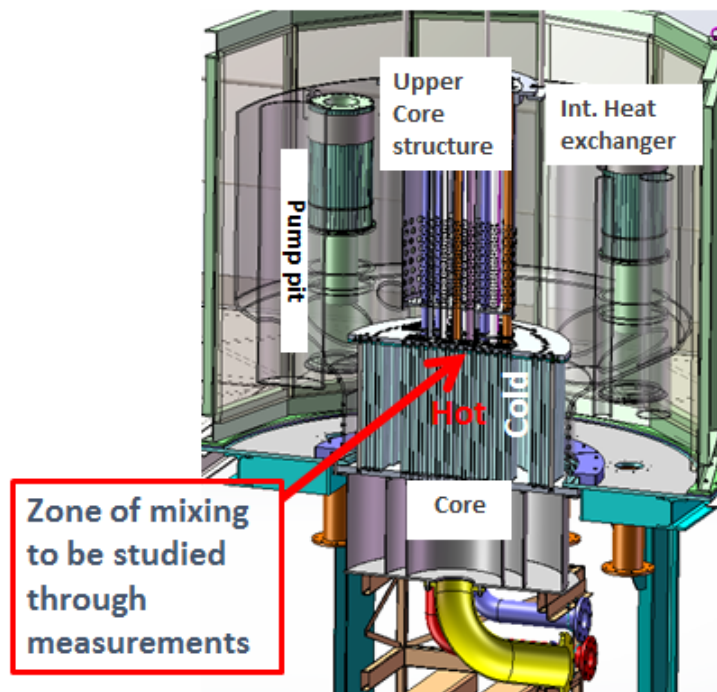


Figure 7: Cross-view of the MICAS mock-up [6]

1.5 Interest of the thesis subject

This thesis is a part project of the development of the fast neutron reactor cooled by sodium ASTRID which was presented before. From the state of art of the past and foreign reactors, issues have been identified. The numerical codes cannot address some of them with a sufficient level of confidence because it is not possible to model correctly all the physical phenomena. Also, there is a need to validate the design concepts and safety issues of ASTRID. For these reasons, an experimental program was developed. The experience in sodium is necessary in the case where the thermal effects play an important role. Experiments using water serve as a study for the hydraulic aspects because of the similitude between sodium and water in terms of physical properties (see section 1.4). Also, these experiments are practical to apply since water is transparent. This explains the design of the water model, the MICAS mock-up. One issue in the experimental program of the MICAS mock-up is to simultaneously measure the temperature and the velocity fields to validate the numerical approach. These measurements were done before using thermocouples and propeller probes respectively on the mock-up but these approaches are intrusive and punctual.

LIF (Laser Induced fluorescence) and TLC (Thermo-chromic liquid crystals) are both common techniques for non intrusive measurement of temperature. In TLC, when the liquid crystal particles are illuminated by white light, the color of the particles changes depending on the temperature of surrounding fluid. In LIF, a fluorescent dye is dissolved in a fluid and then illuminated by Laser. It absorbs a portion of the excitation energy and spontaneously re-emits a portion of the absorbed energy as fluorescence. This fluorescence emission is temperature dependent so this phenomenon can be used to derive the temperature field. The difference between these two techniques is in the range of temperature measurement. In LIF, the temperature range is greater than that of TLC and covers the range needed for the measurements in the MICAS mock-up.

Regarding velocity, PIV (Particle Image Velocimetry) is already implemented on the MICAS mock-up. In PIV, the fluid is seeded with tracer particles then illuminated with a laser sheet so that particles are visible. The motion of the seeding particles is used to calculate speed and direction of the flow being studied. LIF and PIV are both non intrusive measurement techniques that do not interfere with the flow pattern. These techniques can be easily extended to the simultaneous measurement of temperature and velocity. The goal of the thesis is to accomplish a thermal hydraulic study of the different phenomenology present in the MICAS mock-up; more precisely the interaction between the hot and cold fluid flows present at its core (figure 6). This interaction results in an another jet that leads the flow at the exit of the core which in turn controls the thermal hydraulic effects in the upper plenum. These temporal measurements will serve to study also the issues in the reactor. However, through a survey in literature,

the LIF technique is limited to simple volume geometries (less than 30 Liters) and few experiments are applied on large volume due to the complexities that arise on large scale facilities. For this purpose, a new water mock-up called TABOULE was designed during the first year of the thesis.

TABOULE is an intermediate scale between the simple and the complex water facilities. It is a simple representative of the mixing jets which occur in the MICAS mock-up. It consists of only two jets (one cold and the other hot) whereas that of the MICAS mock-up consists of 288 hot and 292 cold jets. Such a geometry makes it possible to vary several parameters to study the interaction between different fluid flows. The temperature between the cold and the hot jet varies from 20 to 50 °C similar to the case of the MICAS mock-up. This range allows a similitude between sodium and water (section 1.4). The simultaneous measurements using PIV and LIF will allow us to study the variation of temperature and velocity exchange between the fluid flow and its surrounding. TABOULE is a large geometry facility of about 1000 Liters. In this term, the application of such methods on large scale mock-up such as TABOULE is challenging and innovative. This work presents its concept design and a hydrodynamic study of different fluid flows. Then, the work presents the installation of the LIF and PIV measurement setups for a thermal hydraulic study. We also show the complexities faced during the experiments performed and the different approaches done to resolve them.

Chapter 2
Literature Review

2 Literature Review

This section features several topics concerning optical measurement techniques for temperature and velocity focusing on Laser Induced Fluorescence and Particle Image Velocimetry. Then, studies of single and two fluid flows are illustrated since the geometry of the water model MICAS is made up of many nozzles and exhibits similar flows. First, in the frame of measurement, one should distinguish between intrusive and non-intrusive techniques. For instance, in intrusive techniques, the measuring device is in direct contact with the medium of interest such as the case of thermocouples whereas in non-intrusive measurements (called non-invasive too), the medium of interest is observed remotely without any disturbance such as fluorescence techniques. Researchers also defined semi invasive measurements in which the technique involves modification of the component of interest and therefore some disturbance to the temperature field. Thermo-graphic phosphors and heat sensitive paints are examples of semi invasive measurements. Such techniques can be used to indicate temperatures from cryogenic levels to 2000 °C [7]. The following section will study different non-intrusive measurement techniques for temperature and velocity focusing on the choice of laser induced fluorescence and particle image velocimetry for the simultaneous measurement of temperature and velocity respectively.

2.1 Non intrusive temperature measurement techniques

One of the fundamental thermodynamic quantities is temperature. When measuring temperature, several points should be taken into consideration and they are classified as follows: the range of temperature, the what, the where, the when and finally the criteria of the method [8]. By the what, it is either point measurement or average indication, absolute measurement or reproducibility of thermal conditions. The where depends on the nature of medium (solid, liquid, gas), nature of flow and the surrounding environment in general. The when is whether the measurement is simultaneous or not, continuous or not and finally the choice depends on parameters such as reproducibility of a measure, stability, sensitivity and response time. The measurement of temperature field in liquids has evolved overtime. The first attempts were qualitative measurements such as Schlieren-methods or shadowgraphy [9]. But these techniques are one dimension [10]. Another one is the molecular tagging thermometry, which determines the temperature fields from the temperature-dependent phosphorescence lifetime of phosphor molecules in the particular liquid. This method is applied on surfaces and in sprays [11]. Thermocouples have been widely used in temperature measurements. While these measurements are easy to implement, such a technique is intrusive and punctual. It allows measurements at certain points in single phase flow experiments and does not give temperature field measurements. These are the main drawbacks of thermocouples. But to measure whole temperature field, two methods are now of a great interest; TLC (Thermo-chromic liquid crystals) and LIF (Laser Induced Fluorescence). Both techniques are non-intrusive too. Such advantages overcome the drawbacks of

using thermocouples. These two methods are explained in the coming sections.

2.1.1 Thermo-chromic liquid crystals (TLC)

This section explains the approach of TLC in temperature measurements. The technique has been widely used as a full field mapping measurement. It is the molecular structure of the crystals that show a distinctive dependency on temperature. The most popular crystals used are called cholesteric crystals shown in Figure 8 [12]. The observed color of a liquid crystal is a function of several variables including the orientation of the crystals, the spectral nature of the light illuminating the surface, and the spectral response of the sensing device. The molecular orientation of thermo-chromic liquid crystals is altered by temperature. A video camera is usually used to record the colors. Then, these records are stored in terms of the primary colors RGB: red, green, and blue. After analysis, the data is converted from RGB to values of hue, saturation, and intensity. It is also important to state that this technique can be combined with simultaneous measurements of velocity such as the experiments done by Schiepel et al. [13]. However, the main disadvantages of this technique is the relatively narrow temperature range depending on chosen liquid crystals, size of these particles and response time.

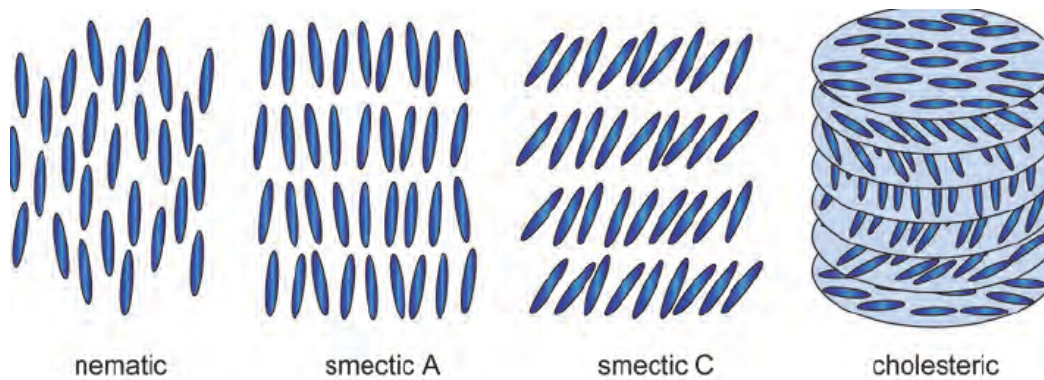


Figure 8: Schematics of several liquid crystals phases [12]

2.1.2 Laser Induced Fluorescence Technique (LIF)

This section covers several points regarding the LIF technique. It provides a review of its evolution throughout the history, then parts are dedicated to explain fluorescence, theoretical approach, types of LIF, basic set up and the sources of errors.

- **Review of LIF over history**

The purpose of this section is to review the evolution and development of this technique. It all started by visualizing flow using dyes. The first experiments were done in the 1970's. Nichols et al. [14] used the technique for measuring mass transfer and flow visualization in 1972. In 1977, Owen [15] did some basic experiments of laser velocimetry to measure structure of turbulent spray flames. In the 1980's, Koochesfahani and Dimotakis [16] were the first to provide a basis for modern LIF use which is explained in the next sections. They although used LIF to measure the concentration field in a liquid plane mixing layer. After this start, in 1987 Walker [17] measured the variation of fluorescence intensity with temperature, pH, concentration and laser intensity. He gave a detailed description of the principles of LIF concerning the experimental set-up. His main goal was to measure concentration field in mixing liquids. The technique continued to be developed at the end of 1990's by two major researchers Coppeta et al. and Sakakibara et al. [18, 19]. Coppeta et al. [18] focused on quantifying pH and introduced the ratio between laser intensities whereas Sakakibara et al. [19] focused on quantifying temperature and introduced types of errors in this technique which are explained later. Then in the 21st century, the LIF technique was divided into different types depending on the fluorescent dyes used. In principle, experiments were developed by Sakakibara [21] and Lemoine et al. [22, 23] especially in the study of combustion.

- **Fluorescence, a physics approach**

Figure 9 shows the different mechanisms for returning a molecule previously excited by laser radiation to its ground state. Fluorescence is among these different paths. Fluorescence is a radiative decay process that occurs by electronic transitions in molecules [19]. It is a molecule that absorbs light between a certain range of wavelengths and emits light at a different wavelength [25]. First, it becomes excited when the incoming light is absorbed [26]. Then, it can be translated as the spontaneous and poly chromatic light emission. The fluorescence phenomenon has two attractive characteristics:

- Fluorescent molecules have a large absorption cross section, almost 10 times larger than in the case of Raman scattering. Consequently, a few ppm of the fluorescent species is enough to obtain a signal of high intensity which is easy to use.
- Fluorescence has a very short lifetime, of order 10^{-6} to 10^{-9} seconds which makes it possible to observe the rapid phenomena.

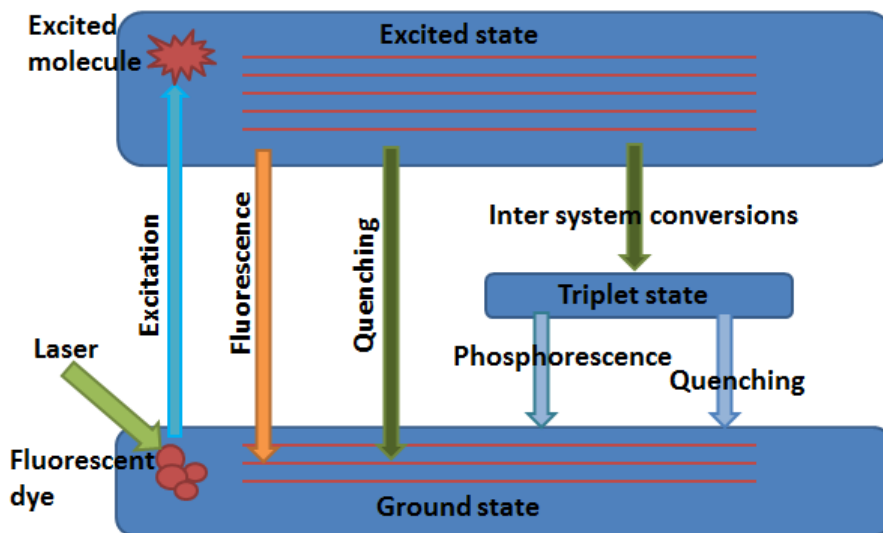


Figure 9: Diagram illustrating the possible mechanisms of an excited electron [113]

The different mechanisms shown in figure 9 compete with fluorescence. Quenching is an inelastic relaxation due to the shock from molecules and it depends

highly on the temperature of the surrounding liquid. The Inter system conversions correspond to the transition to different energy levels close to the excited state. Thus, the electron can return either rapidly or slowly. The rapid return may happen in one of two ways. It may simply return from the excited state through quenching, or it may fluoresce at a certain wavelength. A slow return from the triplet state results in phosphorescence whereby the absorbed radiation may be delayed and re-emitted at a lower intensity.

From these different mechanisms, it is possible to define the quantum fluorescence yield as being the ratio between the rate of spontaneous fluorescence transition (A_{21}) and the rates of competing mechanisms ($A_{21} + Q_{quenching} + Q_{triplet} + Q_{inter}$) [113].

In the condensed phase (liquid phase), the number of transitions between the excited and fundamental state is considerable. This leads to the poly chromatic character of absorption and emission spectra. Thus, fluorescence absorption and emission spectra give this appearance of signal extending over several tens of nanometers.

• Fluorescence, a mathematical approach

From a mathematical point of view, the fluorescence can be used either to measure temperature or concentration. When the temperature of the medium is constant, the local concentration of the fluorescent tracer can be measured and when the concentration of the fluorescent tracer is constant, the temperature of the liquid can be determined [27].

However, the equation of the fluorescence emission intensity is not unique. It depends on the regime of the laser excitation we are working on. There are three characteristic regimes defined through a comparison between the laser excitation intensity I_0 ($\frac{W}{m^2}$) and the saturation intensity of the fluorescent dye I_{sat} ($\frac{W}{m^2}$) [113].

If $I_0 \ll I_{sat}$, the regime is said to be linear. In this case, the fluorescence emission intensity is linear with the laser excitation intensity and it is expressed as follows:

$$I_f = K_{opt} V_c I_0 \varphi \varepsilon_1 C e^{-C(\varepsilon_1 b + \varepsilon_2 e)} \quad (1)$$

where K_{opt} is an optical calibration constant, V_c the collection volume, φ the fluorescence quantum yield, ε_1 the molar absorption coefficient of the laser light, C the concentration, ε_2 the molar absorption coefficient of the fluorescence, b the laser path and e the fluorescence path (figure 10). In this approach, we have two absorption coefficients because both the laser light and the fluorescence light are absorbed while they travel, according to the Beer-Lambert's law. The product $V_c C$ is proportional to the number of fluorescence photons emitted by the tracer molecules excited by the laser radiation and reaching the detector surface. In addition to this, the fluorescence light is reabsorbed before being collected by the recording devices due to the presence of liquid between the laser sheet plane and the cameras [26, 27]. This re-absorption differs between

they dyes and it depends on the overlapping between the absorption and the emission spectra.

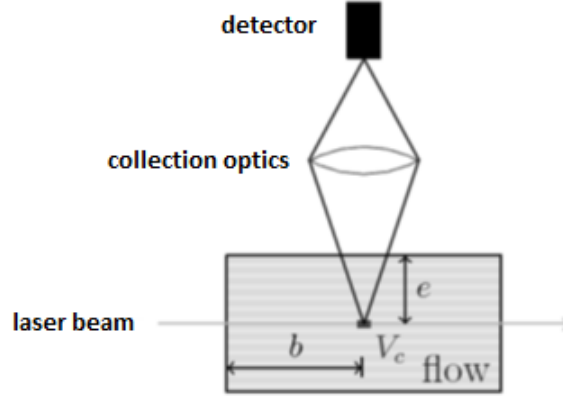


Figure 10: Schematic diagram of the fluorescence intensity measurement [26]

If $I_0 \approx I_{sat}$, the regime is said to be partially saturated. In this case, the fluorescence emission intensity no longer depends linearly on the laser excitation intensity.

If $I_0 \gg I_{sat}$, the regime is said to be saturated. In this case, the fluorescence emission intensity no longer depends on the laser excitation intensity. Only the reabsorption of fluorescence on the collection path is then taken into account. The fluorescence emission intensity is then expressed as follows:

$$I_f = V_c I_{sat} \varphi \varepsilon_1 C e^{-C \varepsilon_2 e} \quad (2)$$

The temperature dependence of the fluorescent emission appears in the absorption coefficient or in the fluorescence quantum yield depending on the dye used. For instance for RhB, the major part of the temperature dependence can be found in the fluorescence quantum yield [26]. In contrast, the absorption coefficient, ε_2 , does not have significant temperature dependence. It is less than 0.05% /°C as mentioned in the study of Sakakibara et al [19].

However for FL27, the temperature dependence of the emitted fluorescence is due to the absorption coefficient ε_2 since the quantum yield is greater than 0.9 at room temperature. So it is unlikely that the positive temperature dependence of the fluorescence signal of fluorescein is due to increased quantum yield effects (Sutton et al. [32]).

- **Basic set up of LIF**

The basic setup of a LIF experiment consists of a Laser source, a camera, fluorescent dyes and some sheet optics as shown in figure 11. This section will explain in details the role of each and the importance of a good synchronization between all the components.

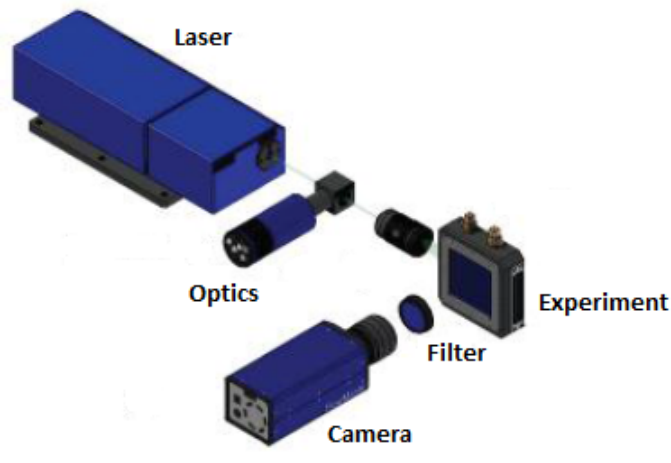


Figure 11: The LIF setup

Laser

The term “LASER” is an acronym for “Light Amplification by Stimulated Emission of Radiation”. A laser is created when the electrons in atoms in special glasses, crystals or gases absorb energy from an electrical current and become excited (figure 12). Then, the excited electrons move from a lower-energy orbit to a higher-energy orbit around the atom’s nucleus. When they return to their

ground state, the electrons emit coherent particles of light called photons. These photons are all at the same wavelength [28]. Most of the experiments done in this field used either continuous Argon Ion laser (488 or 514.5 *nm* wavelengths) or pulsed Nd:YAG laser at 532 *nm*. The laser is used to excite the fluorescent dyes in the flow. Starting from here, different parameters are taken into consideration when choosing the laser. For instance, ion lasers have continuous output which produces a beam that has a Gaussian distributed cross-section. This continuity leads to stability in its output power which simplifies the calibration procedure for the system. On the other hand, pulsed lasers have a much higher captured energy per image when compared to ion lasers. However, the power and distribution of the beam can vary from pulse to pulse. So, the main advantage of Nd:YAG lasers is their high power output around $10^7 W$ during the pulse.

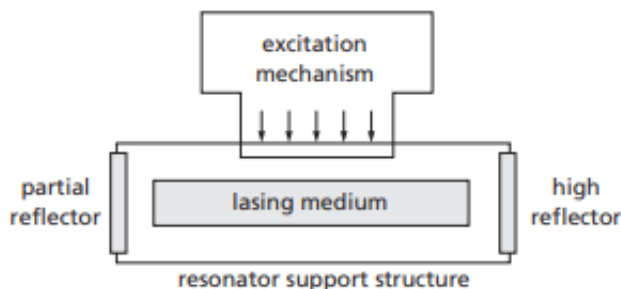


Figure 12: Basic laser principle

Camera

The camera is used to capture the signal of fluorescence. It can be either Coupled Charged Devices (CCD) or Complementary Metal Oxide devices (CMOS). In the LIF experiments, CCD digital cameras began being used in the 1990's. But recently, CMOS cameras have become popular and advantageous [25].

The main key features of any digital camera are pixel count, bit depth, and frame rate. The first feature is related to what is called the Full Well Capacity [29]. It is the maximum number of electrons that register a signal in a pixel. So, larger pixels have higher well capacity thus higher sensitivity,

better Signal to Noise Ratio (SNR), and increased dynamic range. Bit depth determines the resolution of the intensity. For example, a bit depth of N , resolves a 2^N gray scales. The latest technology nowadays allows for a bit depth of 16, or $2^{16} = 65,536$ gray scales. Finally, the frame rate determines how quickly successive images may be acquired. There are several differences between CCD and CMOS cameras. The main one is how they transfer the charge out of the pixel and into the camera's electronics. For example, in CCD, the charge is collected in pixels and then shifted on the imager surface to the output for sampling. Micro lenses, which increase the photon collection area of the pixel, are used in CCD whereas the layer stacks up in CMOS prevents its usage and thus lowers the charge conversion resulting in lower sensitivity [29]. On the other hand, CMOS is more resistant to Smearing or Blooming than a CCD. Both phases are due to over saturation of pixels. Blooming is shown as very bright spots in the image whereas smearing is shown as light spilling over into the vertical shift. Thus, CCD sensors create high-quality, low-noise images whereas CMOS sensors are more susceptible to noise and consume little power [30].

Fluorescent dyes

This part shows the important characteristics of dyes, their different types in LIF experiment and their absorption and emission spectra.

First, a fluorescent dye should be soluble in water when it is the liquid of interest in the experiments. The dye should have a high quantum efficiency so that signal strength is maximized. Its absorption and emission spectra must be separable. This is known as the Stoke's shift. There are many dyes used in LIF experiments. Mainly, when choosing them, the absorption spectrum should be compatible with the laser excitation wavelength. Most of the LIF experiments used either fluoresceins (FL, FL27) or rhodamines (RhB, Rh6G, RhWT, Rh101, Rh110, Rh640, SR101, SRh640, and KR).

Classical fluorescein is widely used as a tracer in aquatic studies for temperature measurements because of its water solubility, low cost and low toxicity [22]. Fluoresceins have shown positive temperature dependence as shown by Coppeta et al. [18] and Sutton et al. [32].

Regarding rhodamines, different results were obtained by researchers. For example RhB, there is a general agreement on its negative temperature dependence but the sensitivity changed from one study to the other. Saeki et al. [33] recorded it -1.34 % per °C, -0.8 by Bruchhusen et al. [23] and -1.82 by Sakakibara et al. [19]. It is important to state that RhB is toxic and leads to environmental problems. On the other hand, rhodamines such Rh6G and RhWT exhibit no temperature dependencies and are harmless. Figure 13 shows the absorption and emission spectra of several dyes while figure 14 shows only that for FL27. Details of some of the dyes stated above are explained later in Chapter 3.

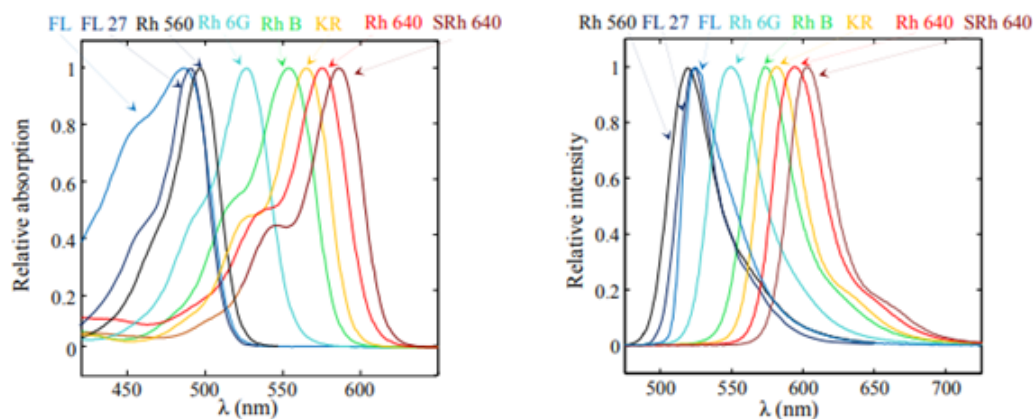


Figure 13: Absorption and emission spectra measured at 25°C (pH=5.6 for FL and pH=6.5 for RhB) [114]

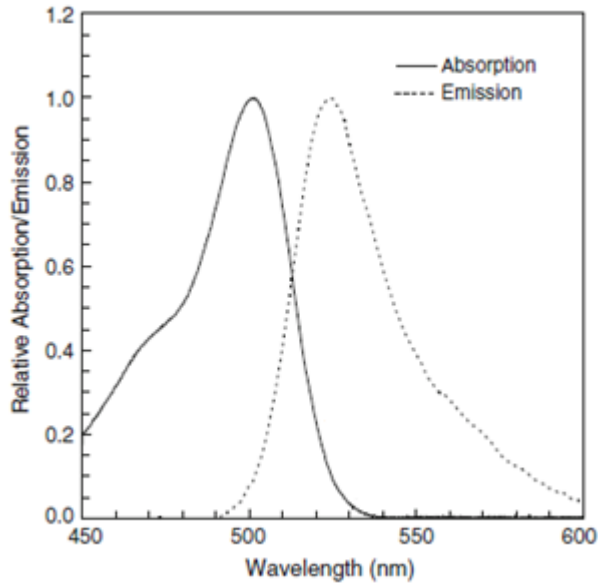


Figure 14: Relative absorption and emission spectra of FL27 at 23°C [32]

- **Methods of LIF**

In this section, different types of LIF applications are explained, showing the characteristics, advantages and the inconveniences of each. According to the articles and experiments done in this field, LIF can be divided into different methods. It is the number of dyes and the detection bands that specify these methods.

- *Using one dye*

When using one fluorescent dye, two types are defined: one color (single band), one dye LIF (1c/1d) and two color, one dye LIF (2c/1d). 1c/1d is the technique that usually all researchers start with. It is a calibration approach in which they identify their medium; that is the response of fluorescence intensity as function of dye concentration, laser power and temperature variation. The setup of this technique is simple and basic. It gives a good precision for the study of single-phase laminar and turbulent flows. However, it is sensitive to the laser power and the volume of collection of the fluorescence. 2c/1d LIF

was introduced in 2001 by Lavielle et al. [22] for droplet measurements. Only one dye with wavelength dependent temperature sensitivity is used. It depends on the spectral bands of the fluorescent dye. The measurements are done by determining the relative intensities on two adequate spectral bands of the same dye and a reference measurement at a known temperature (figure 15). Although this technique is insensitive to laser power, dye concentration and volume of collection, a reference spectral band is necessary for the conditions of absorbance.

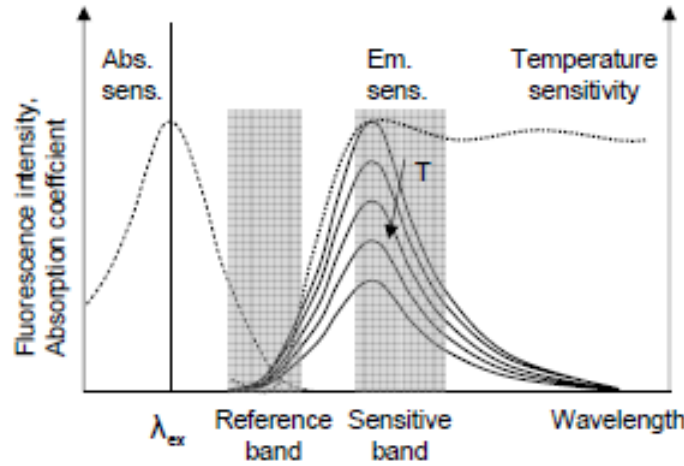


Figure 15: Two color one dye technique [23]

2c/1d LIF planar measurements were done by Bruchhausen et al. in 2005 [23]. They investigated the mean temperature field and temperature fluctuations on a heated turbulent jet into a co-flow jet at ambient temperature. Usually in such experiments, RhB is chosen. With two interference filters, the intensities of two small wavelength bands of 10 nm are captured. It was also extended to handle the case of multi-component droplets as in the studies of Depredurand et al. and Maqua et al. [34, 35, 36]. In this field of sprays and droplet studies, this technique has introduced a correction function in terms of size effect. For instance, the fluorescence ratio increases widely when the droplets diameter decreases. Moreover, when the tracer concentration increases, the size effect decreases [37]. This technique is highly applied when the dye concentration is not uniform, for example in the presence of mass transfers such as liquid evaporation or vapor condensation.

Using two dyes

Two color two dye 2c/2d LIF was introduced as an extension of fluorescence techniques to overcome the drawbacks of one color LIF such as laser power dependency. When two dyes are used, the ratio of their fluorescence emissions is taken as a measure of temperature reading. The two dyes need to have significantly different temperature dependencies (Sakakibara & Adrian [19]). For example, a temperature dependent dye can be selected and the second dye should at least be a temperature independent as proposed by Sutton et al. in 2008 [32]. In water facilities, application of the LIF technique requires both water-soluble organic dyes that have an absorption peak close to the laser excitation wavelength (Crimaldi et al. [38]). That's why most of the experiments in this field were done using RhB and Rh110 because both can be excited with the same laser source [39]. Figure 16 shows the emission and absorption spectra of a mixture of these two dyes.

Melton et al [40] proved great advantages of this technique over one color LIF. For instance, it corrects for laser power fluctuations, laser sheet non-uniformity and dye absorption since the ratio of the dye concentrations is constant. By referring also to equation (1) which is presented again below, Labergue et al. [112] illustrated that to properly measure the temperature, the influence of the unknown and variable parameters C , V_c and I_0 must be removed.

$$I_f = K_{opt} V_c I_0 \varphi \varepsilon_1 C e^{-C(\varepsilon_1 b + \varepsilon_2 e)}$$

Then, the fluorescence intensity of the first and the second dye (A and B) are presented by equations (3) and (4) respectively. The ratio, independent from the laser, is presented by equation (5).

$$I_{f,A} = K_{opt,A} V_c I_0 \varphi_A \varepsilon_1 C_A e^{-C_A(\varepsilon_1 b + \varepsilon_{2,A} e)} \quad (3)$$

$$I_{f,B} = K_{opt,B} V_c I_0 \varphi_B \varepsilon_1 C_B e^{-C_B(\varepsilon_1 b + \varepsilon_{2,B} e)} \quad (4)$$

$$R = \frac{I_{f,A}}{I_{f,B}} = \frac{K_{opt,1} \varphi_A C_A e^{-C_A(\varepsilon_1 b + \varepsilon_{2,A} e)}}{K_{opt,2} \varphi_B C_B e^{-C_B(\varepsilon_1 b + \varepsilon_{2,B} e)}} \quad (5)$$

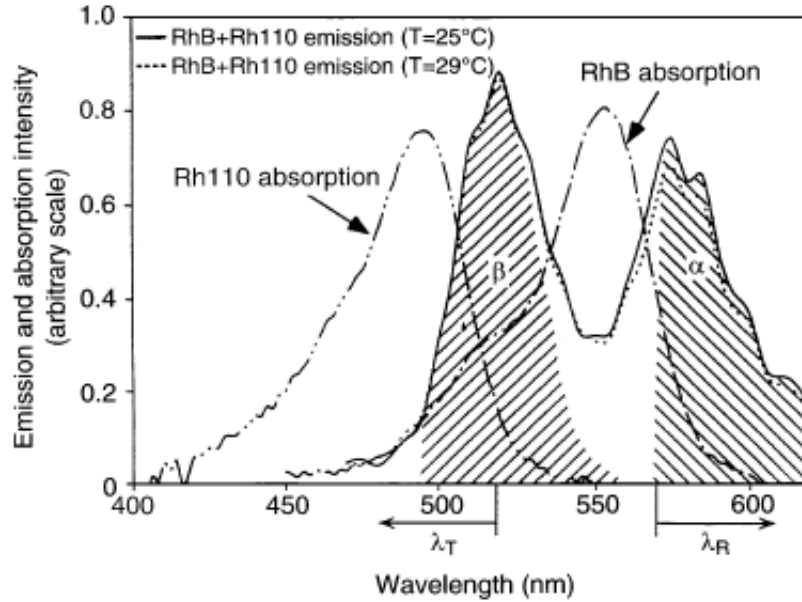


Figure 16: Two color two dye technique [19]

Typically two cameras are used to measure the individual intensities of the dyes. This technique is used in the field of single phase laminar and turbulent flows and also in that of sprays [35]. To sum up, fluorescence techniques using laser have shown great interest in measurements of field temperature due to its advantages over other techniques. For example, over Thermo-chromic liquid crystals (TLC), LIF method is used for measurements with a high temperature range while the TLC method is limited to a narrow temperature range. Other drawbacks of TLC are its strong non-linearity and the significant time response of the relatively large particles [41].

- **Sources of errors & Spectral conflicts**

Sources of errors:

There are three main sources of error in using spectral information to measure scalar behavior temperature. Errors result from photo-degradation of the dyes, optical limitations of the system, and from uncertainty in the camera response [18]. For instance, photo-degradation is a result of continued exposure of the dye to the chosen excitation frequency. Its effects can be minimized by frequent calibration, minimizing the exposure time of the dye to the excitation light, and using the longest excitation wavelength possible to excite the dye.

Spectral conflicts:

Spectral conflict is due to the overlaps between absorption and emission bands of two dyes. There are three main spectral conflicts summarized in Table 3; type I, II & III. They have been described by Coppeta and Rogers [18] and further by Lacassagne et al. [42]. In this section, each type is briefly explained along with figures that illustrate the overlap between the bands and the difference between each type.

Type	Summary of spectral conflicts
I	Emission overlap between the two dyes; dye 1 and dye 2
II	Dye 2 absorbs dye 1 emission; absorption is independent of scalar
III	Dye 2 absorbs dye 1 emission; absorption is dependent of scalar

Table 3: Table showing three types of spectral conflicts

Type I error refers to the two dyes that have an emission overlap as illustrated in figure 17 in which some of the fluorescence from dye 1 will appear in the intensity measurement of the second dye. Although the emission spectra of both dyes are separated, but the decaying of the first dye overlaps with the peak emission of the second dye.

In figures 18 and 19, the dashed line refers to the absorption band of dye 2 and the solid line to the emission band of dye 1. Type II and type III errors refer to the overlap between the emission band of one dye and the absorption band of the second dye. That is the second dye absorbs emitted light from the first dye so that the measured fluorescence of the first is smaller than expected. However the difference between type II and type III is the changes in the scalar being measured. As illustrated in table 3, type II spectral conflict is independent

of scalar. If we suppose the scalar is concentration (usually dyes are present in equal concentrations throughout the fluid); changes in the scalar being measured only produce changes in the fluorescence intensity. In contrast, for type III, the fluorescence intensity of the first dye is being attenuated as a function of path length due to the overlap between the emission of first and the absorption of the second dye (figure 19). Also, since the absorption band of the second dye varies with concentration, the attenuation of the emission of the first dye is now also a function of concentration.

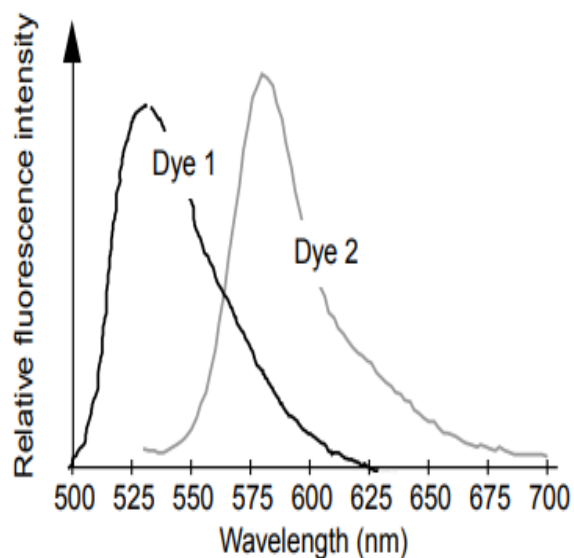


Figure 17: Type I spectral conflict [18]

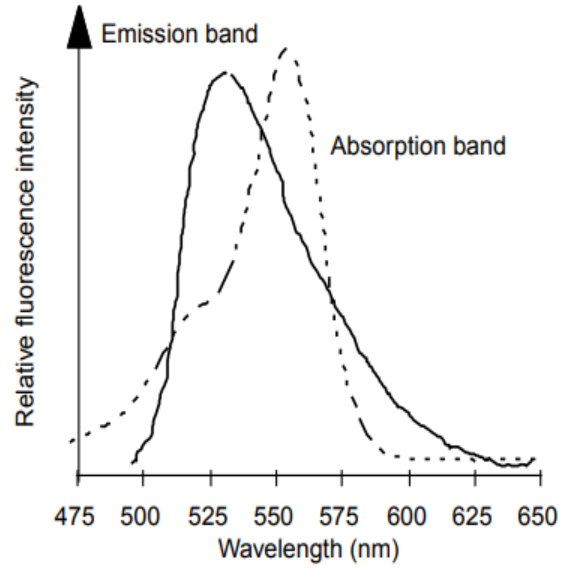


Figure 18: Type II spectral conflict [18]

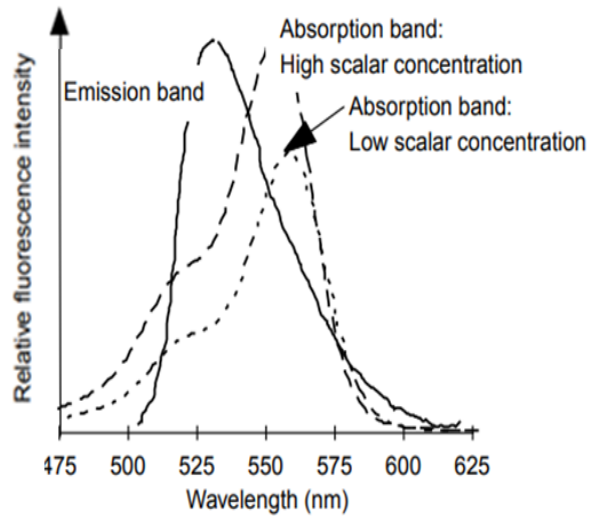


Figure 19: Type III spectral conflict [18]

2.2 Non-intrusive velocity measurement techniques

This section is dedicated to non-intrusive techniques for velocity measurements such as Laser Doppler Velocimetry (LDV) and Particle Image Velocimetry (PIV). It starts with a general definition about velocity measurement techniques and then explains the LDV method briefly whereas the PIV technique in details. It ends with a summary about most experiments found in literature that used combined velocity and temperature techniques simultaneously.

2.2.1 Introduction

In general, the methods of measuring the velocity of liquids are classified into three main groups: kinematic, dynamic and physical. In kinematic measurements, a specific volume, usually very small, is somehow marked in the fluid stream and the motion of this volume is captured by appropriate instruments. Dynamic methods make use of the interaction between the flow and a measuring probe or between the flow and electric or magnetic fields. And for physical measurements, various natural or artificially organized physical processes in the flow area under study, whose characteristics depend on velocity, are monitored [43]. Examples for kinematic velocity measurements are LDV and PIV which are explained in the next sections.

2.2.2 Laser Doppler Velocimetry

- **Setup and operating principles**

Laser Doppler Velocimetry (LDV) is a technique used to measure the instantaneous velocity of a flow field [44]. This technique has two forms regarding its operating principles. In the first which is most presently used, a single beam is split into two beams, thus ensuring coherence between the two as shown in figure 20. Then, the optics focuses the beams to intersect at the the focal point of the laser beam, where they interfere and generate a set of straight fringes. As particles entrained in the fluid pass through the fringes, they reflect light that is then collected by the receiving optics and focused on a photo-detector. The reflected light fluctuates in intensity, the frequency of which is equivalent to the Doppler shift between the incident and scattered light. This frequency is thus proportional to the particle velocity.

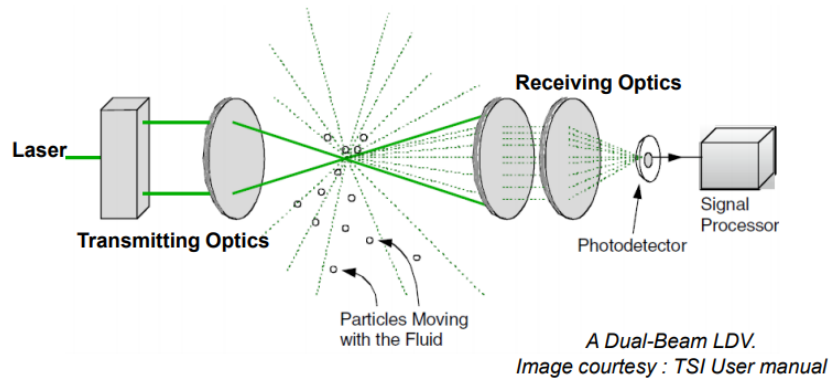


Figure 20: Laser Doppler Velocimetry principle

The second form is of a different approach. A single beam is split into two beams, the measurement beam is focused into the flow whereas the reference beam passes outside the flow. When particles pass through this volume, they will scatter light from the measurement beam with a Doppler shift too. The first portion of this light is collected by the receiving optics and transferred to the photo-detector. The reference beam is also sent to the photo-detector where the optical detection produces an electrical signal proportional to the Doppler shift, by which the particle velocity component perpendicular to the plane of the beams can be determined.

- **Comparison of LDV with other techniques:**

LDV just like other techniques has its advantages and disadvantages. It is a non-contacting measurement with a very high frequency response. On the other hand, a sufficient transparency is required between the laser source, the target surface, and the receiver. That's why its accuracy is highly dependent on the alignment of the emitted and reflected beams. Although this method is non-intrusive and has high accuracy, it is a single point measurement. This is the main drawback of this method. Thus, it can't be used in the measurements of velocity field. On the other hand, PIV overcomes this drawback. It is a non-intrusive technique that measures velocity field in a flow. The next paragraph is dedicated to explain in details all about the PIV technique.

2.2.3 Particle Image Velocimetry

The section starts with the principle of PIV, its setup, its main features and the combination of this method with optical techniques for measurement of velocity and temperature simultaneously.

- **Introduction**

The concept of PIV is traced back to over 100 years. It is Ludwig Prandtl who started it. He suspended mica particles in his water tunnel and could visually see how a fluid flowed around models [45]. Back then, this only provided qualitative information regarding the flow. But nowadays with the recent advances in cameras, lasers and computer processing, it is possible to extract instantaneous velocity information inside complex flows.

- **Principle and setup**

PIV is a non-intrusive velocity measurement technique. It provides instantaneous velocity information in fluids [46, 47]. The principle of PIV is simple. First, the flow is seeded with tracer particles. The laser sheet illuminates these particles at least twice within a short time interval. Then the camera takes images of the target area and captures each light pulse in separate frame images. The displacement of the particles between the light pulses is used to determine the velocity vectors.

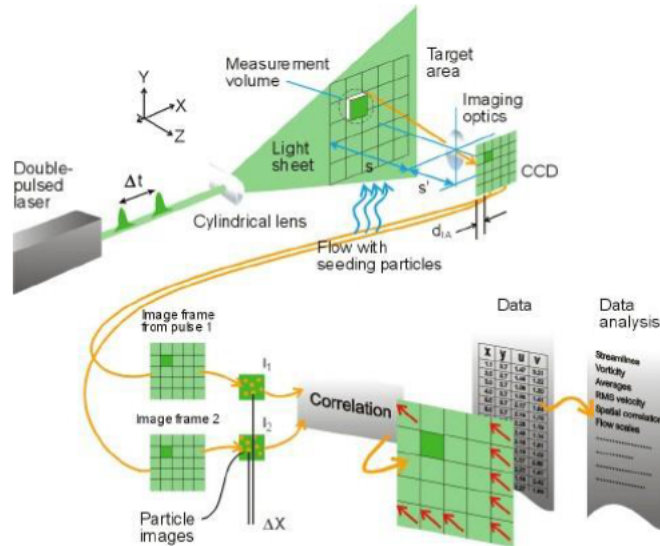


Figure 21: Set up of the PIV technique

The experimental setup of PIV (figure 21) consists of several subsystems: the tracer particles, the light source, the recording device and the image analysis [45]. Each subsystem should meet the minimum requirements for an optimal measurement of velocity. Starting with the tracer particles, they need to be small enough to accurately track the flow, yet large enough to be optically tracked. It is important to accurately choose an appropriate seeding material to obtain accurate PIV data [46]. Therefore there are some principles to take into consideration. For example, the tracer particles should be non-toxic, non-corrosive, non-abrasive and chemically inactive. They should also exhibit an ability to follow the flow and be good light scatters [48, 49] . Table 4 shows some typical seeding particles used in liquid flows.

Material	Particle diameter (μm)	Comments
Aluminum powder	< 10	Preserves polarization by scattering
Bubbles	5 to 500	Can only be used when the two-phase flow is acceptable. The bubbles must be in the spherical Re-Eo regime and the terminal rising velocity must be negligible to the fluid velocity
Glass spheres	10 to 150	
Latex beads	0.5 to 90	Delivered with narrow size distribution but expensive
Milk	0.3 to 3	Cheap and efficient but not popular
Pine pollen	30 to 50	Excellent marker with regard to relative particle density (Egg-shaped and swell somewhat after some time in water)

Table 4: Typical seeding PIV particles

Since the seeding particles should be illuminated in order to be captured and analyzed, a light source is needed. This light source is typically a laser. A laser is used because of its ability to emit monochromatic light with high energy density, which can easily be bundled into thin light sheets for illuminating and recording the tracer particles without chromatic aberrations [46, 50]. The most used laser types for PIV are Helium-neon, Argon-ion, and Nd:YAG lasers. To capture the position of seed particles in the flow field, either CCD or CMOS cameras are used. In order to compute flow velocities from particle images,

images must be compared and correlated. This correlation involves rigorous statistical computation. The characteristics of these correlation techniques and their limitations were reviewed by Adrian [51] and later expanded by Adrian and Keane [52] to include cross-correlation techniques. On the other hand, the software needs to cooperate with a synchronization unit. It is the synchronizer that makes the link between the software, the camera and the laser.

- **Main features of PIV**

This part studies the main features of PIV indicated and studied by Raffel et al. in 2007 [46]. Some features are common with Laser Doppler Velocimetry and others are unique for PIV. First, PIV is a non-intrusive velocity measurement technique. It also measures the velocity of a fluid element indirectly by means of the measurement of the velocity of tracer particles within the flow thus it is an indirect velocity measurement technique. A unique feature of PIV is its whole field measurement since it records images of large parts of flow fields in a variety of applications in gaseous and liquid media. Other features regarding the illumination pulse are its duration and the time delay between pulses. For instance, the duration must be short enough to “freeze” the motion of the particles during the pulse exposure. This avoids blurring of the image. Regarding the time delay between the illumination pulses, it must be long enough to determine the displacement between the images of the tracer particles with sufficient resolution and short enough to avoid particles with an out-of-plane velocity component leaving the light sheet between subsequent illuminations.

- **Experiments in simultaneous measurements of velocity and temperature**

Some experiments were done in the field of simultaneous measurements of velocity and temperature. Researchers combined PIV with TLC and others PIV with LIF. This part is dedicated to show the approaches done in these measurements. For instance, Sakakibara et al. [55] combined LIF with PIV for temperature and velocity measurements in thermo-fluid flow. They mixed fluorescent dyes with tracer particles in the flow. Two CCD cameras were used at the same time, one for LIF and other for PIV to image fluorescent intensity and particles’ scattering. The purpose was to clarify the heat transfer of stratified flow and natural convection. Petracci et al. [56] discussed the use of one-color/one-dye combined PIV/LIF as a measurement technique on a Rayleigh–Bénard convection cell. They used a Nd:YAG laser with Rhodamine B as fluorescent dye. Petracci et al. [56] pointed out that the use of a Nd:YAG laser combined with Rhodamine B in a combined PIV/LIF measurement technique simplifies the experimental setup compared to a two-color/two-dye setup. However, the use of a one-color/one-dye technique requires additional post-processing of images to remove striations caused by local changes in refractive index due to density differences, and to

correct for pulse-to-pulse laser sheet intensity variations. Grafsrønningen et al. [57] carried out simultaneously PIV and LIF measurements of a buoyant plume above an evenly heated horizontal cylinder with a Rayleigh number of $9.4 \cdot 10^7$. They used two high resolution CCD cameras in combination with a high energy Nd:YAG laser. The vertical velocity and temperature field in the plume was compared with similarity solutions from turbulent planar plumes. They also evaluated the production of Turbulent Kinetic Energy (TKE) due to mean shear. Lemoine et al. [58] carried out simultaneous measurements of temperature and velocity using LIF and LDV respectively. The goal was to characterize thermal transport properties in turbulent flows. RhB was used as a fluorescent dye in their experiments. The technique is demonstrated on a turbulent heated round jet: the mean and fluctuating dynamic and thermal fields are investigated, and the temperature-velocity cross correlations are determined in order to characterize the turbulent diffusivity and the turbulent dimensionless number such as Prandtl. However, the number of articles concerning simultaneous PIV/LIF measurements available in the literature is limited and focused only on simple geometry and small volume.

2.3 Fluid dynamics and two jet flow study

As stated previously in the general context, the objective of the thesis is to apply simultaneous measurements of temperature and velocity on a complex geometry. This complex geometry is a simplification of the mixing flows in the MICAS mock-up. It aims at studying the interaction between two jets at different temperatures and configurations. That is why this section is dedicated to a literature review about studies done in this field. It is divided into three subsections. First, it starts with a general introduction about Navier-Stokes equation, its dimensionless form, the derivation of Reynolds number from it and then presents other dimensionless numbers relative to our experimental approach. The second section treats fluid flows and turbulent mixing by presenting Kolmogorov and Batchelor length scales and their effect on tracking flow. The final subsection gives an overview about single jets and then explains in details the interaction between parallel jets. It ends by listing experiments from literature that applied measurement techniques of temperature and velocity in their studies.

2.3.1 Navier-Stokes equation and dimensionless numbers

The Navier-Stokes equation

The Navier-Stokes equations, named after Claude-Louis Navier and George Gabriel Stokes, describes the motion of viscous fluid substances. It is demonstrated from a momentum balance per unit volume for an incompressible fluid and newtonian fluid[123].

$$\vec{\nabla} \cdot \vec{v} = 0 \quad (6)$$

$$\rho \frac{\partial \vec{v}}{\partial t} + \rho (\vec{v} \cdot \vec{\nabla}) \cdot \vec{v} = -\vec{\nabla} p + \rho \vec{f}_{ext} + \mu \Delta \vec{v} \quad (7)$$

Equation (5) of zero divergence of the velocity field (\vec{v}) ensures the incompressibility of the flow. Each term in equation (6) is a force per unit volume.

ρ denotes the density of the fluid and p the pressure, which by definition is the isotropic part of the stress tensor. The term $-\vec{\nabla} p$ presents normal stresses related to pressure forces. The force per unit mass \vec{f}_{ext} gathers all the forces applied in the volume fluid and μ is the dynamic viscosity of the fluid. Often, only the gravitational forces are present, so $\vec{f}_{ext} = \vec{g}$.

p_0 is the value of the pressure in the absence of flow, so $\vec{v} = \vec{0}$ and $\vec{\nabla} p_0 = \rho \vec{g}$ which presents the hydro-static pressure.

By dividing equation (6) by the density ρ , we obtain the balance of forces per unit mass, which is also interpreted as a transport equation of the speed as shown in equation (7).

$$\frac{\partial \vec{v}}{\partial t} + (\vec{v} \cdot \vec{\nabla}) \cdot \vec{v} = -\frac{1}{\rho} \vec{\nabla} (p - p_0) + \nu \Delta \vec{v} \quad (8)$$

This form of the equation reveals the kinematic viscosity of the fluid ν , $\nu = \frac{\mu}{\rho}$. The term $\nu \Delta \vec{v}$ presents the momentum transport (per unit mass) by molecular diffusion. The term $(\vec{v} \cdot \vec{\nabla}) \cdot \vec{v}$ corresponds to the convective transport of the velocity.

The dimensionless Navier-Stokes equation and the derivation of Reynolds number

The goal of non-dimensionalizing the Navier-Stokes equation is to gain a greater insight into the relative size of various terms present in this equation. It also reduces the number of parameters present. In what follows, we write the Navier-Stokes equation using dimensionless combinations in which we define L by the length scale, U by the velocity scale and thus the time scale (t) becomes $\frac{L}{U}$. These dimensionless combinations noted by an apostrophe are listed in what follows.

$$\vec{r} = L \vec{r}' \quad (9)$$

$$\vec{v} = U \vec{v}' \quad (10)$$

$$p - p_0 = (\rho U^2) p' \quad (11)$$

$$t = \frac{L}{U} t' \quad (12)$$

Then, equation (7) becomes:

$$\frac{\partial \vec{v}'}{\partial t'} + (\vec{v}' \cdot \vec{\nabla}') \cdot \vec{v}' = -\frac{1}{\rho} \vec{\nabla}' p' + \frac{1}{Re} \Delta' \vec{v}' \quad (13)$$

$$Re = \frac{\rho U L}{\mu} = \frac{U L}{\nu} \quad (14)$$

In equations (12) and (13), the dimensionless Reynolds number Re is defined. It is named after Osborne Reynolds in 1895. The Reynolds number presents the ratio of inertia to viscosity and consequently quantifies the relative importance of these two terms for given flow conditions [62, 63]. Osborne Reynolds studied several critical Reynolds numbers in which they differ for each geometry [64, 65, 66]. For example, a flow in a pipe of diameter D , experimental observations

show that laminar flow occurs when Re is lower than 2300 and turbulent flow occurs when Re is greater than 2900.

The Richardson number

The Richardson number Ri is a dimensionless number that expresses the ratio of buoyancy to inertia. It is named after Lewis Fry Richardson (1881-1953), a meteorologist who defined the concept of turbulence energy cascade. He summed up his notion of cascade by the following well known summary:

*Big whorls have little whorls,
Which feed on their velocity ;
And little whorls have lesser whorls,
And so on to viscosity.*

In thermal convection problems, Richardson number represents the importance of natural convection relative to the forced convection. It is defined by equation (14):

$$Ri = \frac{g\beta(\Delta T)L}{U^2} \quad (15)$$

where g is the gravity, β is the thermal expansion coefficient, ΔT is the temperature difference between the fluid flow and its surrounding, L is the characteristic length and U is the characteristic velocity [67]. Typically, natural convection is negligible when $Ri < 0.1$ and forced convection is negligible when $Ri > 10$. When defining the laminar to turbulent transition of a mixed convection flow, buoyancy often plays a significant role [68].

The Froude number

The Froude number Fr is a dimensionless number defined as the ratio of inertia to gravity. It is named after William Froude and presented by equation (15).

$$Fr = \frac{U}{\sqrt{Lg}} \quad (16)$$

where U is a characteristic flow velocity, L is a characteristic length (hydraulic depth) and g is gravity.

The Froude number describes different flow regimes of an open channel flow. However, Mizushima et al. [76] defined the discharge Froude number presented by equation (16) to study the effect of buoyancy and density difference in fluid flows.

$$Fr_d = \frac{U^2}{g\beta(T_0 - T_s)L} \quad (17)$$

where T_0 is the temperature of the fluid flow and T_s is the temperature of its surrounding. It can be seen that Fr_d is the inverse of Ri in their study.

To summarize up, Reynolds, Richardson, Froude and discharge Froude numbers are used to study hydraulic, thermal, free surface and buoyancy aspects respectively. These dimensionless numbers are summarized in table 5 and they are used to describe the features of jets.

Dimensionless numbers	Notation	Definition
Reynolds	Re	$\frac{\rho UL}{\mu} = \frac{UL}{\nu}$
Richardson	Ri	$\frac{g\beta(\Delta T)L}{U^2}$
Froude	Fr	$\frac{U}{\sqrt{Lg}}$
Discharge Froude	Fr_d	$\frac{U^2}{g\beta(T_0 - T_s)L} = \frac{1}{Ri}$

Table 5: Dimensionless numbers

This was a brief summary about the dimensionless numbers which are of a key importance in the parametric analysis of many engineering problems.

2.3.2 Fluid Flows

Historically, turbulent flows were treated according to the orientation of the flow. Some are either predominantly vertical or predominantly horizontal. This actually depends on the buoyancy force which is aligned either parallel or perpendicular to the main stream wise direction [59]. But later, other parameters were identified which led to several types of a fluid intrusion. The first parameter is the source of the driven flow which can be momentum, density differences or both together. For instance, a jet is driven by momentum of the source, a plume by density differences (buoyancy), whereas a buoyant jet is driven by a combination of both momentum of the source and density. Another parameter is the type of injection which can be continuous or intermittent. Table 6 summarizes the different types of fluid flows.

	Continuous injection	Intermittent injection
Momentum only	Jet 	Puff 
Buoyancy only	Plume 	Thermal 
Both momentum and buoyancy	Buoyant jet or forced plume 	Buoyant puff 

Table 6: Different fluid flows [115]

The common characteristics between turbulent jet and plume are the efficient turbulent mixing with the ambient fluid, the loss of kinetic energy due to turbulence and the conservation of momentum. Just in plumes, the kinetic energy is converted into potential energy. Turbulent mixing is the process by which a fluctuating turbulent flow dilutes and homogenizes certain quantities such as mass concentration, heat, and momentum [60, 61]. Two primary parameters that compete to control mixing are kinematic viscosity ν and molecular diffusivity α . In the following, we present the length scales of turbulence used in this approach and the relation between them.

First, the dissipation of turbulent kinetic energy to heat occurs at the Kolmogorov microscale η which is presented in the equation below:

$$\eta = \left(\frac{\nu^3}{\varepsilon} \right)^{1/4} \quad (18)$$

where ε is the dissipation rate of the turbulent kinetic energy.

Second, the molecular diffusion α which acts to smooth the steep concentration gradients [25] occurs at the Batchelor length scale L_B which is presented in the following equation:

$$L_B = \left(\frac{\nu\alpha^2}{\varepsilon} \right)^{1/4} \quad (19)$$

From (6) and (7), the Kolmogorov and Batchelor length scales are related to Schmidt number as presented below:

$$\frac{\eta}{L_B} = \left(\frac{\nu}{\alpha}\right)^{1/2} = (Sc)^{1/2} \quad (20)$$

$$Sc = \frac{\nu}{\alpha} \quad (21)$$

The molecular diffusivity of fluorescent dyes in water is about order $10^{-10}m^2/s$ as shown by Crimaldi et al. [38] and the kinematic viscosity is about $10^{-6}m^2/s$. So, the value of Schmidt number (ratio of viscous to mass diffusion rate) is order of 10^4 . Thus, referring to equation (19), the smallest concentration scales in the flow (L_B) are roughly 100 times smaller than the smallest scales of motion (η) so we can track the flow due to the concentration.

2.3.3 Single and parallel jets

Starting with a single jet, it is usually produced whenever a fluid is ejected from a round nozzle. The geometrical characteristics of the nozzle affect to a large extent the exit velocity profiles. For instance, if the contraction ratio of the nozzle is large enough the velocity distribution is more or less constant over the cross-section and is commonly denoted as a ‘top-hat’ profile [69].

Due to the high velocity gradient behind the nozzle, an axisymmetric shear layer forms and develops between the jet and the ambient fluid. It is within this region that the velocity of the jet will gradually approach that of the ambient fluid and where the initial phases of the mixing process occurs.

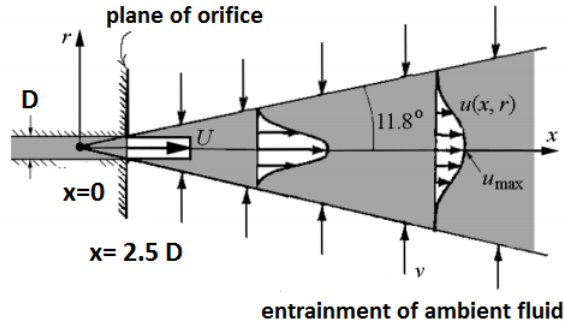


Figure 22: Sketch of a self-similar turbulent jet [73]

In figure 22, the fluid flow studied is injected steadily from a small nozzle into an unbounded surroundings, at distances large compared to the nozzle diameter D . Turbulent jets are observed to develop along their x-axis in a self-similar way, which means that all the flow properties, including turbulent fluctuations, remain the same along the axis after proper normalization by the length and time scales. The origin of the x-axis is at a distance about $2.5D$ upstream the nozzle edge [70]. For the following figures, the velocity profile across the jet is denoted by u and the maximum speed at the centerline is denoted by u_{max} . Figure 23 shows the radial profiles of mean axial velocity in a turbulent round jet at a high Reynolds value of 95500 in which the dashed lines indicate the half-width of the profiles. As can be seen, the jet decays and spreads with the increasing axial distance x . The velocity u decreases while the jet's half-width $r_{1/2}$ increases.

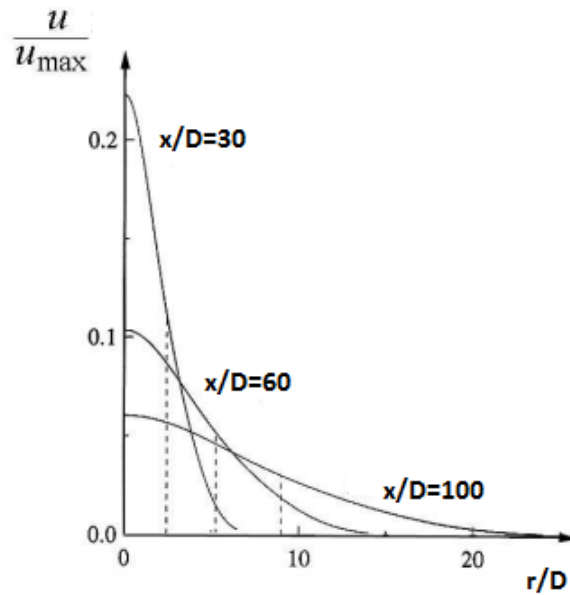


Figure 23: Radial profiles of mean axial velocity in a turbulent round jet [73]

Turbulent jets with negative buoyancy seem of great interest. This interest arises from the fact that these flows are found in many industrial applications such as the injection of reactants in combustion chambers or in nature [75]. A

negative buoyant jet occurs when a jet fluid is heavier than an ambient fluid with an initial momentum being upward. The momentum is continually being decreased by the buoyancy force until it becomes zero. Then, the heavy fluid falls back in an annular region surrounding the up flow. Usually in such a case, the discharge Froude number is considered negative [76]. The next part shows the experiments done in the field of single and parallel negative buoyant jets. It summarizes the goal behind these experiments. Turner measured the penetration distance of salt water jet injected into fresh water in a range of small discharge Froude numbers [77]. Seban et al. [79] measured temperatures in a heated turbulent air jet discharged downward into an air environment and showed that centerline temperatures and the penetration depth are predicted adequately by constant property theories for the downward flow alone. Fleischhacker and Schneider [80] presented very limited experimental results on the centerline velocity and temperature. T. Mizushima et al. [76] presented descriptive experimental results. They proposed mathematical expressions on the spread of the up flow, the width of the down flow and the penetration distance of the jet discharged upward into an ambient of higher temperature than that of the jet fluid (figure 24).

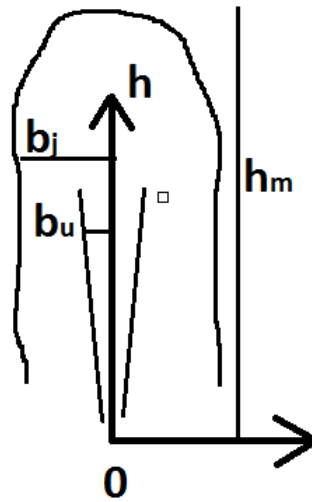


Figure 24: Schematic representation of a negative buoyant jet [76]

They identified b_u as the width of the up flow, b_j as the width of the jet, h as the penetration height and h_m as the maximum height reached. Then, they presented these parameters as function of the discharge Froude number as

shown in equations (22) and (23). The discharge Froude number was identified as the inverse of Richardson number in their study as was defined in equation (16).

$$b_u = 0.17h \quad (22)$$

$$\frac{b_j}{D} = 0.37\sqrt{Fr_d} = 0.37\sqrt{\frac{1}{Ri}} \quad (23)$$

$$\frac{h_m}{D} = 1.66\sqrt{Fr_d} = 1.66\sqrt{\frac{1}{Ri}} \quad (24)$$

However the constant value 1.66 in equation (23) changed between studies. Mizushina et al. [76] added their work to the studies previously done in the same field as shown in figure 25.

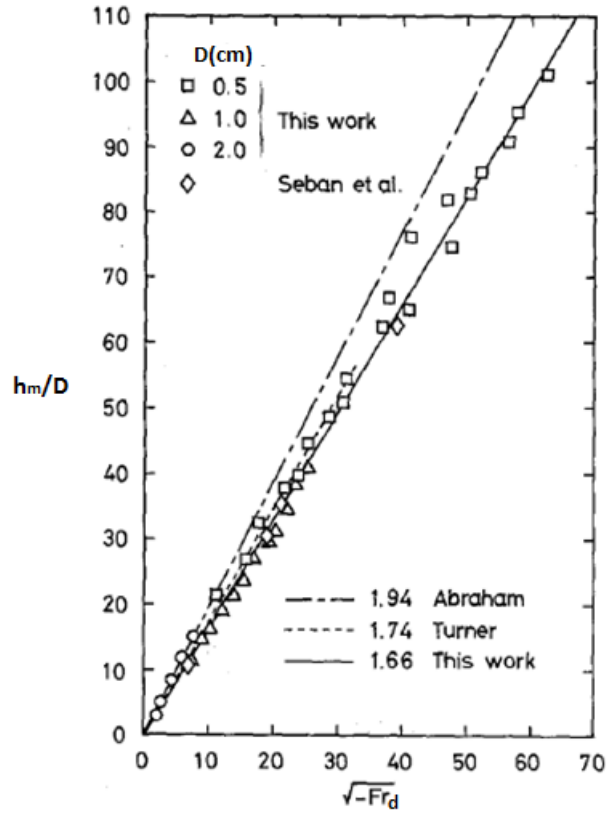


Figure 25: Variation of penetration height [76]

Next section focuses on dual-jet formed by combining a circular swirl jet with a round straight jet. LI et al. [81] studied the case of dual jet in terms of pressure. They designed a new developed system by dividing the pressurized water into two streams: one flow through the swirling path to get the swirling velocity then flows out the annular orifice and form the swirling jet, and the second flows directly through the inner round orifice to form the central straight jet. They concluded that the oriented abrasive jet perforating could reduce the initiation fracture pressure.

Dimotakis [82] studied the dynamics of round turbulent jets in the near and far field. A jet of diameter 0.75 cm and $Re=2500$ and their goal was to study fully turbulent jets. Regarding their conclusions, large scale vertical structures dominate the dynamics of fully developed turbulent jets and not only in the transition region.

A number of studies attempted to account for the interaction of an array of round buoyant jets. Some studied this interaction by applying optical measurement techniques and others by modeling supported by CFD. For example, an interesting study was done by Adrian et al. [83]. They considered group of multiple buoyant jets, each with nozzle diameter D , initial velocity U_0 , concentration C_0 , source fluid density ρ_0 , discharging into an otherwise stagnant ambient with uniform density ρ_a and depth H (figure 26).

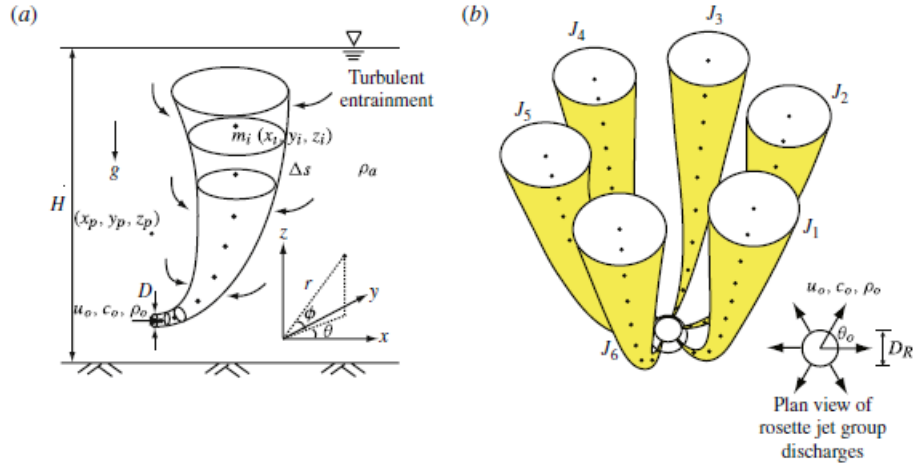


Figure 26: Sketch of an inclined buoyant jet (a) and a rosette buoyant jet (b) [83]

They studied the dynamic interaction of multiple buoyant jets in stagnant ambient conditions by a semi-analytical model. They computed the jet-induced external flow by a distribution of point sinks along multiple free jet trajectories obtained using integral jet models.

In the nuclear reactors field, there are also approaches to evaluate the mixing process along the jets. The reason is to study the phenomena of thermal stripping. It is due to the high cycle thermal fatigue caused by the temperature fluctuation in the regions where hot and cold fluids are mixed. The first fluid is the hot sodium from fuel sub assemblies and the second is the cold sodium from control rod channels and blanket fuel sub assemblies. The water experiment is called WAJECO and the liquid sodium experiment is called PLAJEST as shown in figure 27. The latter consists of three parallel jets used to examine the intensity of the attenuation process of temperature fluctuations from the fluid to a metal test plate set along the flow. Thus, another metal test plate was added

to the water experiment WAJECO to compare the results between water and sodium for the transfer characteristics of temperature fluctuations from fluid to structure [84, 85].

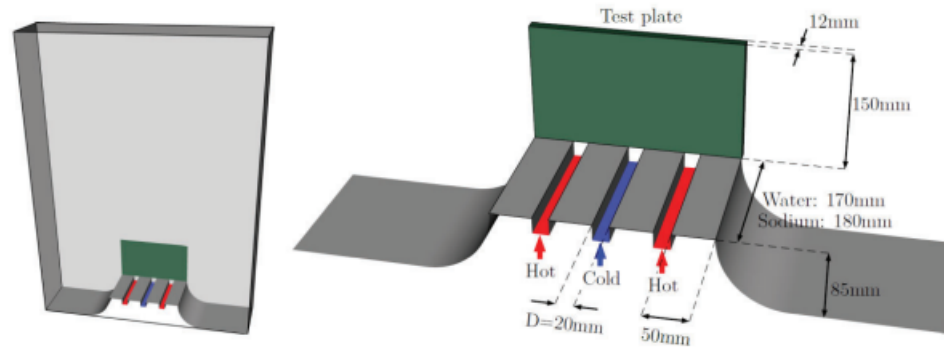


Figure 27: Overview of the test section and zoom on the jet slits and test plate [84, 85]

The Reynolds number values are about 15,000 for PLAJEST and 26,000 for WAJECO. Now regarding the measurements of velocity and temperature, the velocity field is measured by PIV only in WAJECO whereas the temperature in the mixing area is measured by movable thermocouples in both facilities. In the water experiment, the temperature fluctuation intensity increased once as the measured point approached to the wall. However, the temperature fluctuation intensity decreased in the area of the wall surface. Kimura [86] explained this profile due to the influence of the boundary layer from the wall. Then, numerical calculations were applied to validate and verify the coding.

3 Protocols for optical methods: PIV & LIF

This part is an overview of the materials used for the application of the optical methods Laser Induced Fluorescence (LIF) and Particle Image Velocimetry (PIV) in our experiments. In general, the setup of these two methods consists of basic devices of two types. The first is functional such as the camera, the laser, synchronizer, software and fluorescent dyes for LIF whereas particles for PIV. The second type is optical devices such as filters. Starting with the functional devices, many principles are taken into consideration when choosing the right materials. In other words, a compromise is done between the physics of the laser used, the accuracy of the camera and the chemistry of the fluorescent dyes for LIF and particles for PIV. The following section explains in details the functions and the compatibility of the materials used starting with the laser, the cameras, the synchronizer and the software. Then, a section is dedicated to explain the choice of fluorescent dyes and PIV particles and their compatibility with the optical devices.

3.1 Functional Devices

3.1.1 Laser

The laser used in our approach is a 532 *nm* Nd-YAG Quantel EverGreen laser. It is a dual pulsed laser common for both PIV and LIF applications. Its maximum output energy is about 200 mJ per pulse at frequency of 15 Hz. It has actually two laser cavities mounted on the same laser head so it is a dual pulsed laser. The Q-Switch Delay is about 135 μ s. It is the time between the excitation of the Crystal Nd-YAG and the opening of the Q-Switch for Laser 1 and Laser 2. Physically, this value corresponds to the time required to reach the peak of energy in the cavity after the excitation of the Crystal Nd-YAG by the flash lamp. So, the Q-switch is thus triggered to open at the moment when the maximum is reached. This laser has a pulse to pulse energy stability less than 2% RMS. This factor is very important when calculating the sensitivity of our measurement. The use of dual pulsed Nd:YAG lasers operating at 532 *nm* has become increasingly common in recent years. The wavelength plays an important role in the choice of the fluorescent dyes because the LIF system requires an appropriately paired laser and fluorescent dye combination where at least part of the laser power is within the absorption band of the dye. Figure 28 shows the laser used in our experiments.



Figure 28: Nd:YAG Ever Green Laser

3.1.2 Camera

In order to measure simultaneously temperature and velocity fields using $2c/2d$ LIF and PIV techniques, three cameras are needed. One camera serves for the PIV measurements and two cameras serve for the two color LIF technique in which each camera records the response of one fluorescent dye. Table 7 shows these cameras with their characteristics. For PIV measurement, a CCD PowerView 8MP camera, 12 bit having resolution of 3320 by 2496 pixels is used. However, two identical CCD PowerView 4MP-HS cameras, 12 bit of resolution 2048 by 2048 pixels are used in the LIF setup. We chose the identical cameras having same resolution for the LIF setup. All the cameras require special attention during cable connections and frame grabber installation. Figure 29 shows on the left the PowerView 8 MP camera and on the right the PowerView 4MP-HS camera.



Figure 29: PowerView Cameras (TSI Incorporate)

Camera Name	Resolution	Gray Scale	Frequency(Hz)	Technique
PowerView 8 MP	3320*2496	12 bit	4	PIV
PowerView 4MP-HS	2048*2048	12 bit	15	LIF

Table 7: Characteristics of the cameras used

3.2 Synchronizer and Software

The synchronizer used is a 610036 LASERPULSE™ and the software is IN-SIGHT 4G. The synchronizer shown in figure 30 plays the role of communication between the laser, the cameras and the software.



Figure 30: The LASERPULSE synchronizer

The timing setup of the camera capture and the laser pulse are adjusted so that the laser pulse coincides with the camera capture. The Insight software displays the timing settings for the synchronizer, laser and the camera in a graphical form as shown in figure 31.

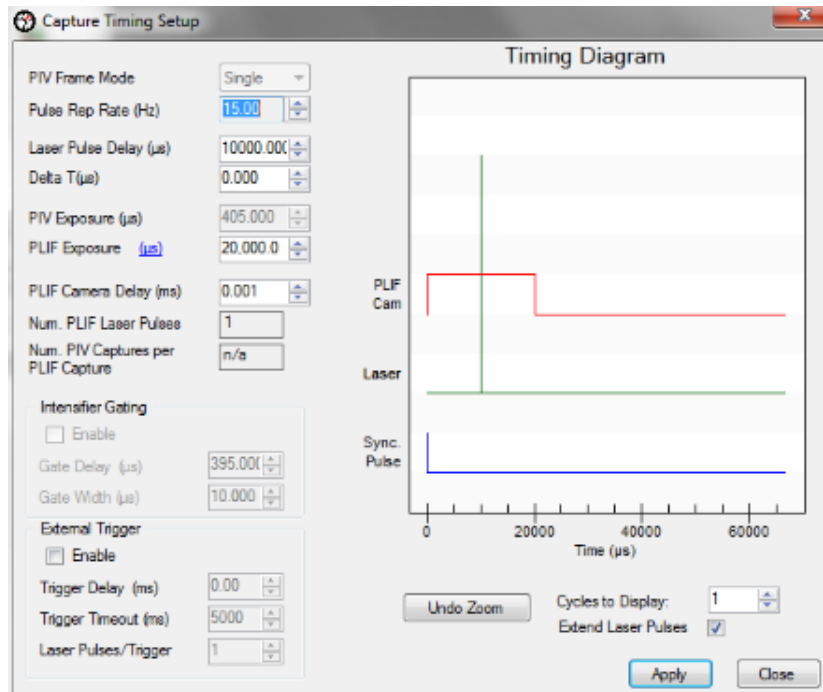


Figure 31: The Timing Setup

This paragraph explains briefly the role of each parameter indicated in figure 31. The Pulse Rep Rate specifies the timing from the start of one laser pulse sequence to the start of the next laser pulse sequence. The Laser Pulse Delay (LPD) is the amount of time to wait from the start of a pulse sequence until the first laser pulse and the PLIF exposure is the time the shutter of the LIF camera is open. The delta T is the time of pulse separation. Since there is a Laser Pulse Delay that takes into account the pumping time in the cavity, the camera sensor exposure time must be set to a value greater than the LPD so that the laser pulse coincides with the image captured by the camera. Thus in the previous figure, the green pulse must coincide with the upper part of the red signal of the camera. This explains the choice of such values.

3.3 Particles, dyes and optical filters

3.3.1 PIV Particles

In general, the tracer particles have sizes that range in microns. They are neutrally buoyant and small enough to follow the flow perfectly and big enough to

scatter the illumination lights efficiently. Thus, the size of the tracer particles should be well chosen. To better understand this effect, an analysis is shown starting from the equation for unsteady motion of a suspended sphere, as given by Basset-Boussinesq-Oseen. It relates the instantaneous relative velocity between the particle and the fluid ($U_p - U_f$) to the instantaneous velocities of the particle U_p and the fluid U_f respectively.

$$\frac{\pi D_p^3}{6} \rho_p \frac{dU_p}{dt} = 3\pi\mu D_p (U_f - U_p) - \frac{\pi D_p^3}{6} \rho \frac{dU_f}{dt} + \frac{\pi D_p^3}{12} \rho \left(\frac{dU_f}{dt} - \frac{dU_p}{dt} \right) + F_B + F_{ext} \quad (25)$$

where D_p is the diameter of the tracer particle, ρ_p is the particle density and ρ is the fluid density.

Equation (24) is composed of 6 terms as listed below.

- Term 1: The product of mass by acceleration.
- Term 2: Stokes drag (it is considered to apply when the particle Reynolds number is smaller than about unity)
- Term 3: Influence of pressure gradient
- Term 4: Inertia effects due to the mass of the entrained fluid
- Term 5: Basset Force
- Term 6: External forces such as electrostatic forces,...

By neglecting terms 5 and 6, the equation of the tracer particle becomes:

$$\frac{dU_p}{dt} = \frac{1}{a} (U_f - U_p) \quad (26)$$

where a is a time constant of the particle and is given by:

$$a = \frac{D_p^2 (2\rho_p + \rho)}{36\mu} \quad (27)$$

When the density of the particle is very close to that of the fluid, this constant becomes:

$$a = \frac{D_p^2 \rho_p}{18\mu} \quad (28)$$

Thus, the falling velocity of a tracer particle in a continuous acceleration fluid denoted by U_g becomes:

$$U_g = ag = D_p \frac{\rho_p}{18\mu} g \quad (29)$$

So from equation 28, the most important features of PIV particles are density and dimension. The former determines the influence of gravitational force that can be neglected if the densities of the tracer particle and working fluid are very similar. The latter determines the light scattering behavior of the particles. Both the features have also a strong influence on the capability of the particles to correctly follow the main flow [46].

The tracer particles used for PIV measurements in our experiments are Nylon particles having diameter of 4 microns and density $1g/cm^3$ very close to that of water. So, the particles are small enough not to affect the mechanical properties of the fluid since their falling velocity calculated is very small compared to that of the fluid flow.

For the preparation method, a very small amount of the particles dissolved in a solution of ethanol (half a cup) is well mixed. Then this solution is immersed in the testing section for measurements. Figure 32 shows the Nylon particles used in our experiments. The number of particles in the flow is of some importance in obtaining a good signal peak in the cross-correlation. As a rule of thumb, 10 to 25 particle images should be seen in each interrogation area.



Figure 32: PIV Particles

3.3.2 Fluorescent dyes

This part explains the reason behind the choice of certain dyes in our LIF experiments, their characteristics and the preparation method of each solution. In our experiments, different dyes are used for the application of LIF. They are classified as two fluoresceins: Classical fluorescein FL & FL27, two rhodamines: Rh6G and RhWT and de-copperized Chlorophyll. The choice of these dyes is first due to their suitability with our 532 nm Nd:YAG Laser since the absorption spectra of these dyes is compatible with this laser excitation. Also, these

dyes have in common that they are all soluble in water, non-toxic and have high quantum efficiency with maximal signal strength. The following sections explain in details the characteristics of each dye divided into parts. The first focuses on the chemistry of each dye which enables us to understand its stability during the experiments and the effects of photo-degradation. The second part is related to the physics of the dye by showing its absorption and emission spectra which decides the choice of filters during the experiments. Then a paragraph is dedicated to explain the choice of pair of dyes needed for the two color LIF approach.

Classical fluorescein

Classical fluorescein FL is the disodium fluorescein and is also called Uranine. Its molecular formula is : $C_{20}H_{10}Na_2O_5$ and has a molecular weight of 376.28 g/mol (figure 33).

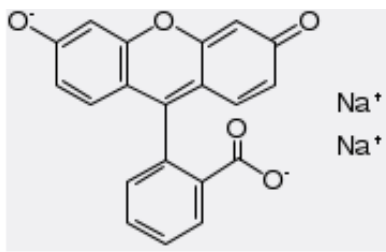


Figure 33: Molecular formula of Classical fluorescein

This tracer is widely used in LIF experiments due to its water solubility which facilitates the preparation of the solution. Classical fluorescein exhibits low toxicity as shown in the study done by Gombert et al. in 2017 [122]. They tested it at high concentrations in excess of the maximum used usually in the experiments and it appears to have no significant toxicological and ecotoxicological effects. Usually a concentration ranging from 10^{-8} M (mol/L) to 10^{-5} M is used in the LIF experiments. The solution of fluorescein is prepared by dissolving a small quantity in a volume of distilled water then passing by dilution to obtain the required concentration. By this method, we assure the diffusion of dye particles in the solution. It is important to state that when once fluorescein is dissolved into water, it decomposes into several forms through a complex set classified into four categories: cations FL^+ , neutral forms FL^0 , anions FL^- , and dianions FL^{2-} . Experiments done by Guilbault in 1990 [110] showed that each one of these species has its own quantum yield and that only anionic ones

have the ability to fluoresce. Classical fluorescein may undergo quenching during the experiments in which it loses its ability to fluoresce. This can be controlled by stirring the solution which allows fast dye renewal. In addition to this, in our experiments, the laser is switched on only during camera acquisition.

This insures the stability of the dye during the experiments and avoids the phenomenon of photo-bleaching. This phenomenon refers to the decay of the emission of the dye over a period of time. In general, these approaches are taken into consideration with all the other dyes. In the context of LIF, it is known that classical FL has a temperature-dependent emission. For instance, Chaze et al. in 2017 [113] reported a temperature sensitivity value of +3.22 % per °C at an excitation wavelength of 532 nm. This value changes to -0.16 % per °C at a laser excitation (continuous) wavelength of 488 nm as was shown by Coppeta and Rogers in 1998 [18]. Figure 34 shows the absorption and emission spectra of classical fluorescein (Uranine). The peak of absorption is at 490 nm whereas that of emission is at 515 nm.

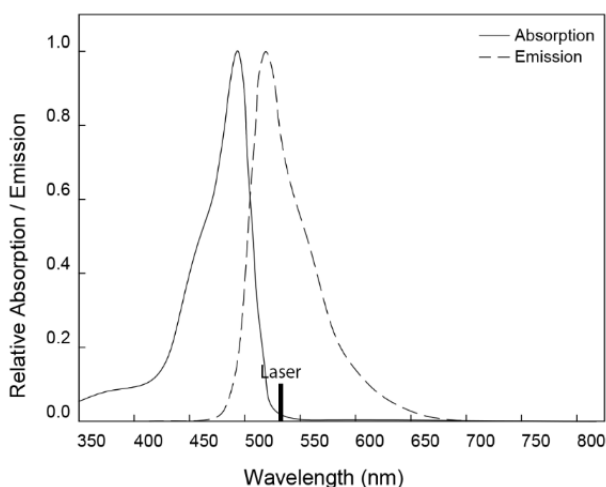


Figure 34: Absorption and emission spectra of classical fluorescein, based on [114]

Fluorescein 27

Fluorescein 27, known as 2',7'-Dichlorofluorescein has a molecular formula of $C_{20}H_{10}Cl_2O_5$ and a molecular weight of 401.2 g/mol (figure 35).

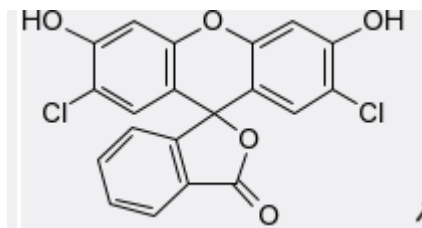


Figure 35: Molecular formula of FL27

Fluorescein 27 exhibits good solubility in water, low cost, and high quantum yield. This dye has also a positive temperature dependent emission of about +3.5% per °C as reported by Sutton et al in 2008 [32] when excited at 532 nm. The concentration range of FL 27 is between 10^{-8} M to 10^{-5} M. Figure 36 shows the absorption and emission spectra of FL 27. The peak of absorption is at 495 nm whereas that of emission is at 525 nm.

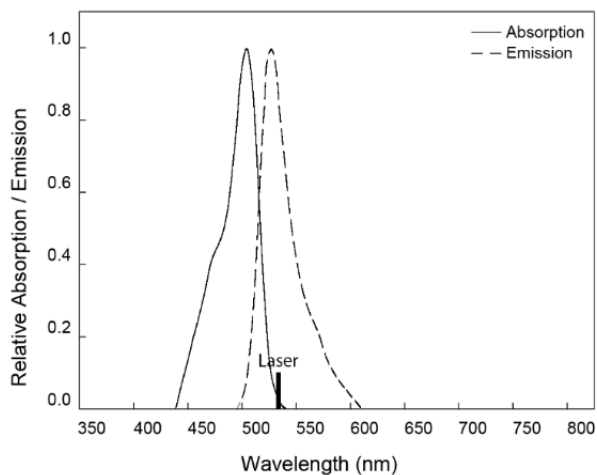


Figure 36: Absorption and emission spectra of FL27, based on [114]

To sum up, fluoresceins are good dyes to use in the LIF experiments because they are temperature dependent, soluble and have high quantum yield. Although these dyes have a low absorption at 532 nm, however this is compensated with the high pulse energies that are associated with Nd:YAG lasers.

However, the problem with using fluoresceins resides in the re-absorption of the dye which affects the measurements, but this is compensated by using a low concentration of these dyes. This solution keeps the medium optically thin as reported by Crimaldi et al. [38]. Such advantages of fluoresceins make them a better choice when compared to rhodamine B. RhB was used by many researchers as temperature dependent dye in small scale experiments but its use in large-scale water facilities causes environmental issues. The next section is dedicated to the characteristics of dyes which are temperature insensitive.

Rhodamine 6G

Rh6G is a basic red fluorescent dye of molecular formula $C_{28}H_{31}ClN_2O_3$ and molecular weight of 479.02 g/mol (figure 37).

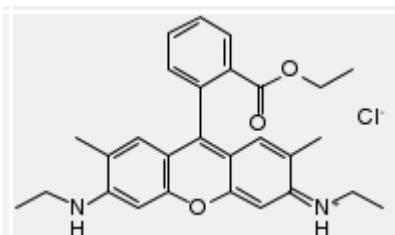


Figure 37: Molecular formula of Rh6G

Rhodamine 6G is also known as rhodamine 590. It is soluble in water and not toxic. This dye is highly resistant to photo-bleaching [38]. As shown in figure 38, it has peak absorption near 525 nm and peak emission near 560 nm. Thus, it can be excited by the 532 nm line from a Nd:YAG laser. Also, this dye is known to be temperature independent. All these characteristics make it a good choice as a reference dye when applying 2c/2d LIF.

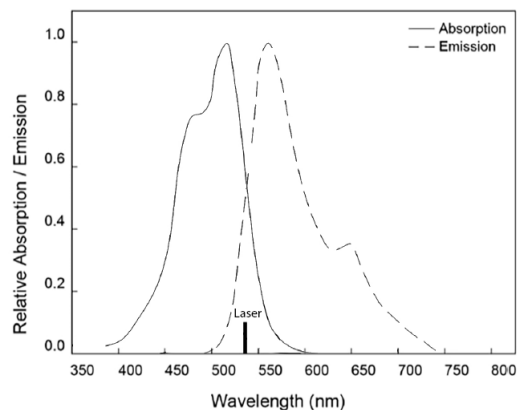


Figure 38: Absorption and emission spectra of Rh6G, based on [114]

Rh WT

RhWT is also called Xanthylum. It has a molecular formula of $C_{29}H_{29}ClN_2Na_2O_5$ and molecular weight of 566.99 g/mol (figure 39).

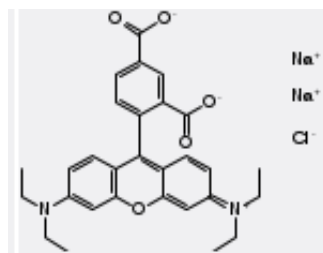


Figure 39: Molecular formula of RhWT

Rh-WT is closely related to rhodamine B. It has approximately same spectral properties as those of rhodamine B. It is soluble in water and very stable during LIF experiments. Thus, it does not undergo photo-bleaching such as the case of fluoresceins. However, there are two main differences between Rh-WT and RhB. Rh-WT is temperature independent whereas RhB has a negative temperature sensitivity when using Nd:YAG lasers. Also, since our experiments are applied

on large volume geometries, RhB exhibits a high toxicity to the environment whereas Rh-WT is much less toxic than other rhodamines. Figure 40 shows its absorption and fluorescence spectra. It absorbs strongly at 532 nm and fluoresces strongly at wavelength of 587 nm .

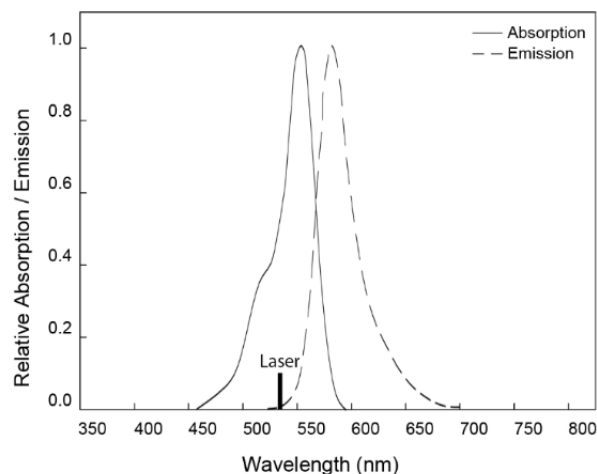


Figure 40: Absorption and emission spectra of RhWT, based on [117]

De-copperized Chlorophyll Sodium Salt

De-copperized Chlorophyll Sodium Salt (Ch-Na) is a gray green powder. It is a saponification derivative, that's why it does not have a chemical formula. This dye exhibits an interest in our experiments because of its absorption and emission spectra. It has an absorption peak at 400 nm whereas an emission peak at 660 nm as shown in figure 41. First, its Stokes shift which is the difference between its emission and absorption peaks is very large compared to the other dyes. Thus, the combination of such a dye with temperature dependent fluoresceins avoids spectral conflicts. The absorption of one dye does not overlap with the emission of the other and same thing regarding emission overlap. Also, upon analyzing Figure 41, the absorption curve of Ch-Na is very stable starting from a wavelength of 450 nm . Thus, it can be excited with different types of lasers.

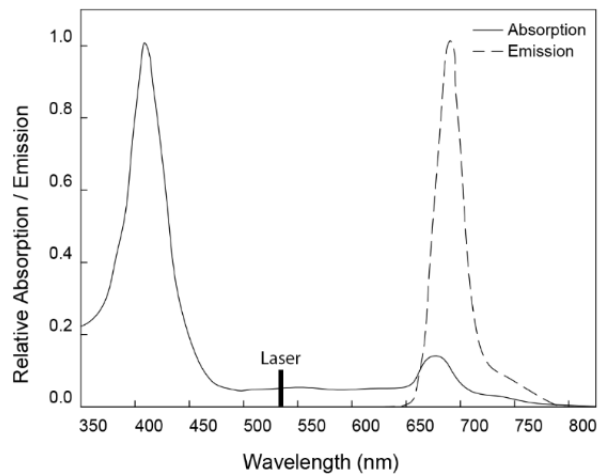


Figure 41: Absorption and emission spectra of Ch-Na, based on [116]

The rhodamines 6G & WT and de-copperized chlorophyll are temperature independent and importantly non-toxic, or at least not as other rhodamines. These make them good choice as second dyes in our experiments of two color LIF.

For best accuracy in our experiments, all the solutions are prepared in the same manner, using the same reagents and the same preparation techniques in the laboratory. Figure 42 shows the solutions of the dyes prepared.



Figure 42: Fluorescent dyes

Conclusion on the choice of dyes

The dyes chosen can be all excited with the pulsed 532 nm Nd:YAG laser we have. This leads to the simultaneous application of LIF and PIV with the same laser source. Moreover, some dyes are temperature (classical fluorescein, FL27) dependent and others are temperature independent (RhWT, Rh6G and Ch-Na). Thus, we can choose several pairs of dyes that serve for the application of two-color LIF such as classical fluorescein; Ch-Na or FL27; RhWT or FL27; Rh6G. That's why before choosing the dyes used in experiments, a certain study must be made to achieve compatibility between the different materials used and the goal of the measurements.

3.3.3 Optical Filters

Filters are typically placed in front of the camera lens and only allow the fluorescence wavelengths to be imaged in the case of LIF technique whereas they isolate the 532 nm harmonics in the case of PIV. In the case of LIF, the choice of filters depends on the fluorescent dye since each absorbs and emits photons at certain wavelengths when excited by laser as shown previously. Figure 43 shows the role of filters in general.

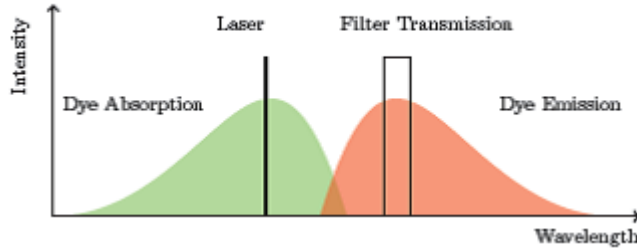


Figure 43: The role of the filter

Due to the usage of several dyes in which each has its different emission band, several filters are needed. To better understand the choice of filters, table 8 summarizes the emission spectra wavelength bands cutoff at 10 % of relative emission. It also shows the emission spectra peaks of the dyes used in our experiments.

Fluorescent dye	Emission spectra band at 10 % (<i>nm</i>)	Emission spectra peak
Classical fluorescein	480-610	515
FL 27	500-590	525
Rh6G	530-650	560
RhWT	560-650	587
Ch-Na	630-720	660

Table 8: Emission spectra of dyes

Ideally we should use filters with transmission spectra corresponding to the overall fluorescence spectral band. However, the choice of the filters has to consider the overlapping of the emission spectra of the different dyes. For instance, a notch filter is used in our experiments when dealing with fluoresceins. This filter works in a manner opposite to that of a band pass filter. It rejects a transmission band centered at 533 nm with a full width of 17 nm . Thus, it cuts off the wavelength of the laser used as well as the particles or bubbles present in the sample which lead to fluctuating readings. Such a filter collects a wide fluorescence bandwidth in the case of fluoresceins.

In this chapter, the components and materials used for the setup of measurements of velocity and temperature by PIV and LIF respectively were presented. The following chapters are dedicated to the two experimental facilities in which

the optical methods are applied on. The first facility is a simple volume geometry (Chapter 4) whereas the second is a complex geometry (Chapter 5) . The simple geometry is a small scale volume when compared to the complex geometry. Starting the experiments on simple geometry aims to identify the most convenient approach for the optical methods later on the complex one. For instance in the case of LIF, many fluorescent dyes are suggested. It is more practical to change the concentration of each dye and even to change the dye in a small volume to study its characteristics as function of different parameters. Later on the complex geometry, the choice of dyes is limited to the most convenient dyes. This gives more accurate results for the measurements of optical techniques.

Chapter 4

Experiments of LIF calibration on a simple geometry

4 Experiments of LIF calibration on a simple geometry

This chapter is dedicated to the experiments of calibration tests done on the small aquarium using the LIF method. First, a technical description of the geometry is presented. Then, this chapter shows the calibration facility used, the planning of the work, the graphs of the response of each fluorescent dye as function of temperature variation and ends up with analysis and conclusion regarding the dyes chosen for the application on the complex geometry.

4.1 Technical description of the simple geometry

The first approach of the experiments is an application of LIF on a simple geometry. The geometry chosen is a glass aquarium of volume 30 liters. The reason is to practically control the parameters that influence the measurements and be able to establish a calibration facility for the measurements. The calibration aims to study the response of the fluorescent dyes used as function of several parameters such as the dye concentration, the laser power and the temperature variation. Figure 44 shows the simple geometry used and the calibration results are presented in the following sections.

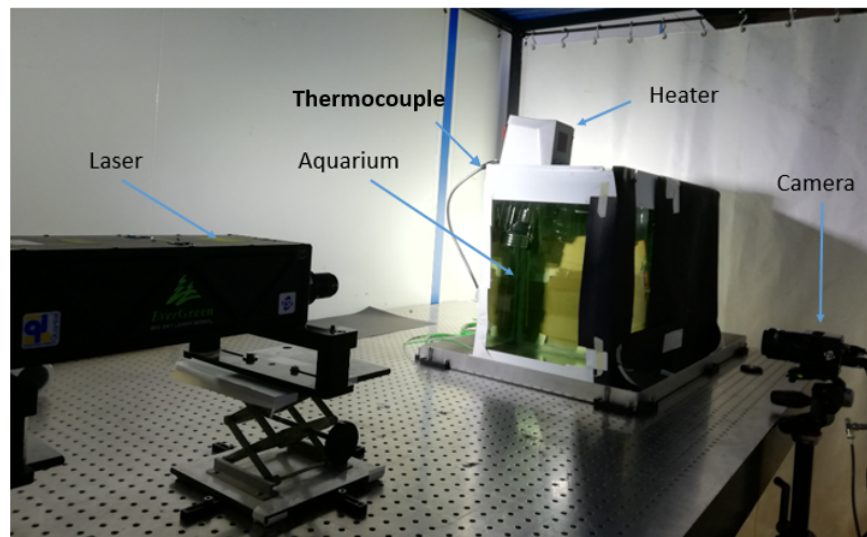


Figure 44: The LIF measurement facility on the simple geometry

The types of laser and cameras used in this facility are explained in chapter 3. The heating thermostat (JULABO GmbH) has a capacity to heat a volume of 50 L to the temperature required in our experiments (60°C). It is also equipped with a small pump that allows the circulation of the solution during heating. Also, two thermocouples type K are inserted in the aquarium to get accurate temperature measurements.

4.2 The approach to measurements

The first step in LIF measurements is a calibration study. It is done using a reference point at known temperature. This allows to convert the fluorescence intensity into a temperature value. It should be carried out when all the parameters that influence the procedure itself are kept constant. The parameters are usually the concentration of the dye, the laser power and the surrounding conditions of the experiments. This gives for each dye a temperature sensitivity coefficient which is necessary to convert fluorescence data and to obtain the values of temperatures in the later experiments.

The sensitivity coefficient is a parameter that corresponds to the relative variation of fluorescence signal I as a function of temperature T .

The coefficient s can be defined as:

$$s = \frac{1}{I} \frac{dI}{dT} \quad (30)$$

If we assume that s does not vary with temperature, then the fluorescence signal can be expressed as follows:

$$I(T) = I(T_0)e^{s(T-T_0)} \quad (31)$$

where T_0 is a reference temperature.

We are interested in the average sensitivity on a temperature range from T_0 to T_1 , so it is possible to estimate it as:

$$s = \frac{\ln\left(\frac{I(T_1)}{I(T_0)}\right)}{T_1 - T_0} \quad (32)$$

This is in general the equation used to calculate the sensitivity of each dye.

Each dye is studied separately. The dyes are in powder form so in order to prepare a homogeneous solution with water, a concentrated one is prepared at first for each dye, then it is diluted several times to get the required range of the concentration to be analyzed. The protocol for the measurements is almost

the same in each case. The solution is immersed in the test section, de-ionized water is added and the solution is mixed well and allowed to settle down.

First, the lens cap of the camera is covered and 100 images are captured. These images are defined as the dark response of the camera which serves later in the image processing step.

Then, a calibration grid is immerseimaged in the solution to convert the pixel of the camera into a metric value.

After this, another series of background images are captured in which the concentration is constant in the aquarium. The calibration facility used is shown in figure 45.



Figure 45: Calibration facility

To study the response of fluorescence of each dye as function of temperature, the heater is turned on and the temperature is increased from ambient until 65°C. At each value, 100 images are captured with the 4MP-HS camera (12 bit of resolution 2048 by 2048 pixels) and saved using the TSI Insight software. Two thermocouples type K are also immersed in the aquarium during all the experiments for accurate measurements of temperature.

The next section will be divided into several parts each showing and analyzing the response of the fluorescent dyes: Classical Fluorescein, FL 27, Rh6G, RhWT and Ch-Na.

4.3 Temperature dependent fluorescent dyes: Classical fluorescein and FL27

A notch filter is used for these fluorescent dyes. It allows a transmission band pass from 400 to 517 nm and from 548 to 710 nm as shown in figure 46.

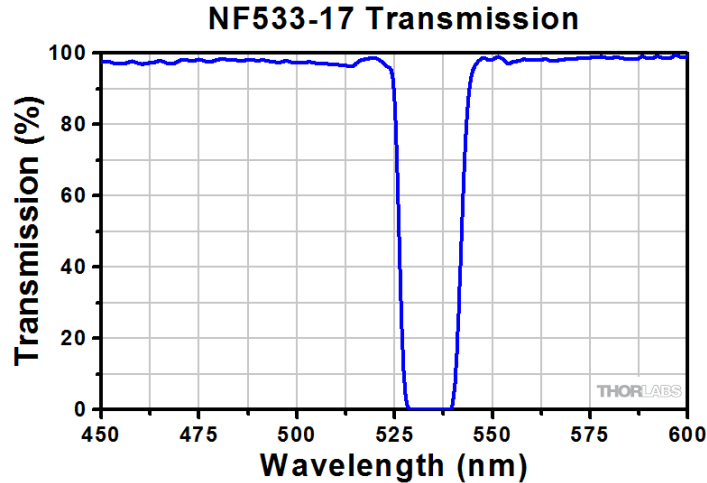


Figure 46: Transmission pass bands of the notch filter

The concentration of these dyes ranged from $10^{-8}mol/L$ to $10^{-5}mol/L$. The position of the camera was approached as close as possible towards the aquarium. The average of the monitored temperatures of the two thermocouples was recorded at each measurement.

The solution of FL27 was prepared with a concentration of $10^{-7}mol/L$. Figure 47 shows the time average response of FL27 and figure 49 shows the time average over 100 raw images at temperature $59.2^{\circ}C$. The red line in figure 47 is uniform so if we suppose that the concentration is homogenized (because it is well stirred), then the temperature is homogeneous. Thus, the spatial average can be applied in our calibration.

According to this and from figure 48, we got a sensitivity coefficient for FL27 of $3.02\%/^{\circ}C$, a value approximately similar to that found by Sutton et al. which is $3.5\%/^{\circ}C$.

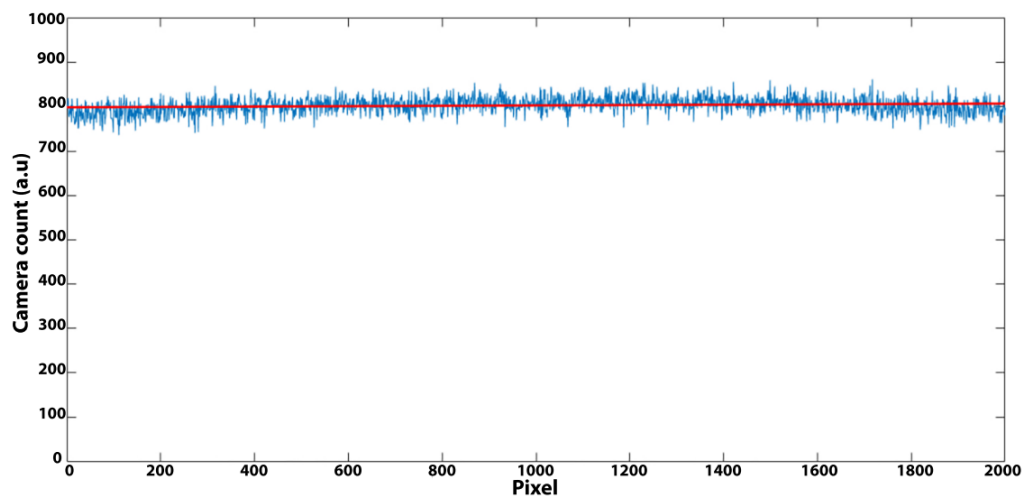


Figure 47: Response of FL27 at temperature 59.2°C

We also re-applied the calibration test of the same solution of FL27 but after two days to study its influence of aging. We realized that both show a very good response as function of temperature variation as shown in figure 49, however that of the first experiment is much more stable than that of the second because of the linearity in its response. The reason behind this is the photodegradation of FL27 with time; that is why the experiments should be done directly and the solution of fluorescein should be stirred frequently.

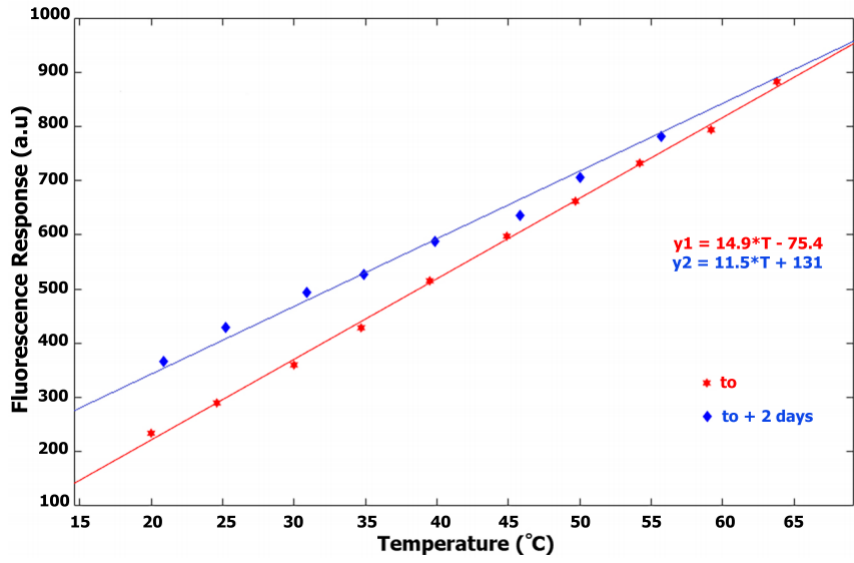


Figure 48: Response of FL27, influence of aging

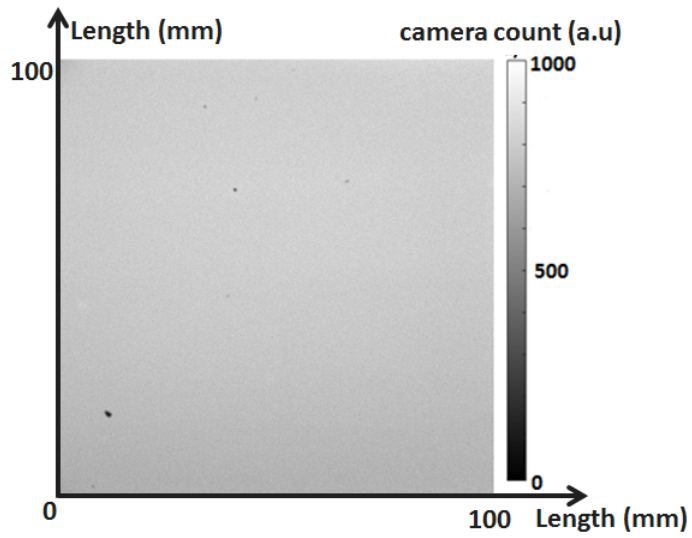


Figure 49: Response of FL27 at temperature 59.2°C

Regarding classical fluorescein, we found approximately no increasing response at 10^{-8} mol/L until 10^{-6} mol/L . Then the response was studied at concentration 10^{-5} mol/L at two periods just like the case of FL27. The response we got was low and was not really varying with temperature (figure 50). However, at a high concentration of 10^{-4} mol/L , the response was positive having a sensitivity of $3.38\% / ^\circ\text{C}$. So, the response of classical fluorescein is null unless using a high concentration under controlled conditions. This response is due to the composition of classical fluorescein which is pH dependent (section 3.1.2). In our experiments we cannot add chemical solutions that can stabilize the pH since later our experiments are applied on a complex geometry.

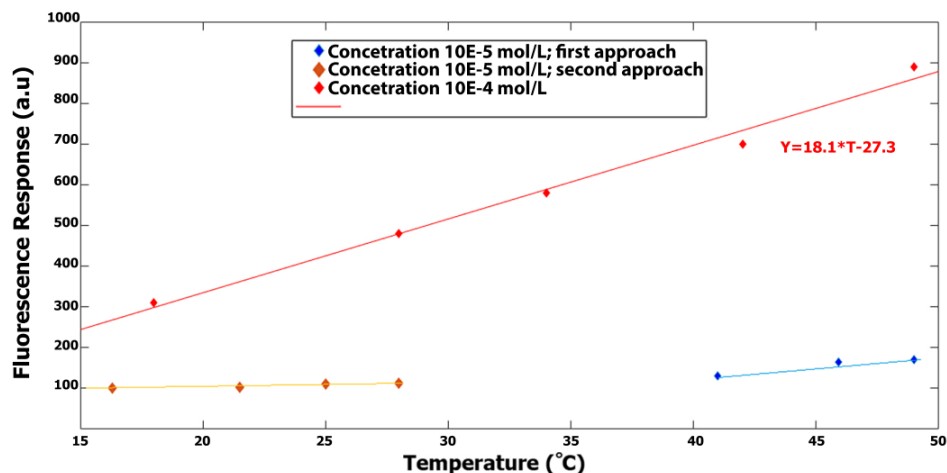


Figure 50: Response of classical fluorescein in three experiments

To end up this section, figures 51 and 52 show the normalized response of FL27 and classical fluorescein respectively done during their first experiments. The normalized values are calculated by dividing the fluorescein response by the maximum value obtained (at the highest temperature) for each value of temperature. From the graph shown, we got interesting results regarding the response of FL27 as it shows more stability and consistency in the values compared to classical fluorescein, that is why it was chosen as a temperature dependent dye for the next experimental approach.

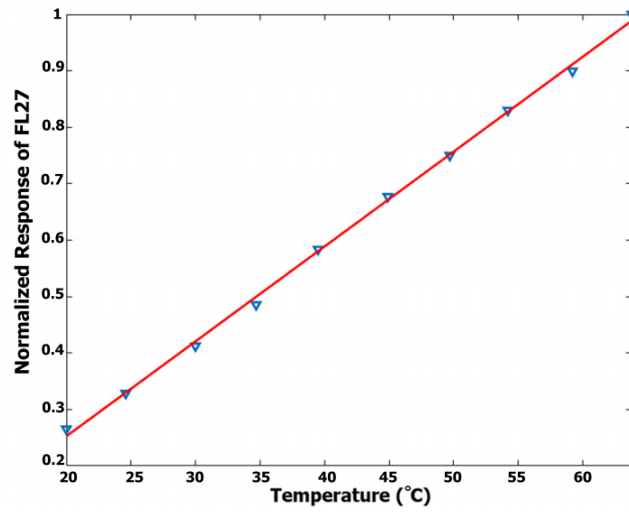


Figure 51: Normalized response of FL27

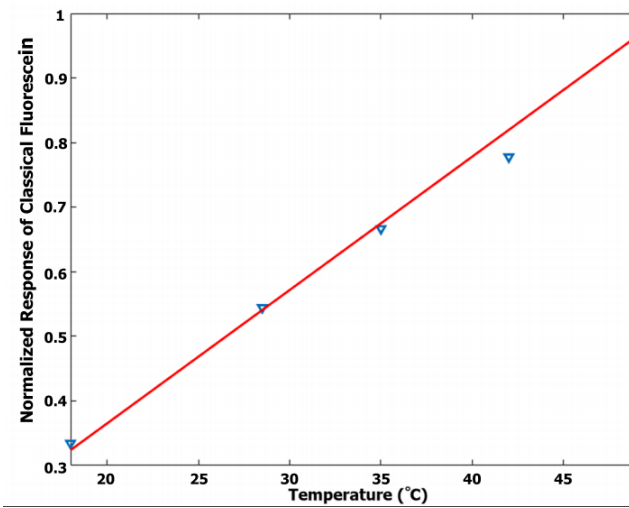


Figure 52: Normalized response of Classical fluorescein

4.4 Temperature independent fluorescent dyes: Rh6G, RhWT and Ch-Na

These dyes are known to be temperature independent. In our approach, we tested their response to choose the most stable one. A temperature independent dye serves as a reference dye in the two color two dye LIF method. It corrects for laser power fluctuations and dye absorption. Figures 53 and 54 show the response of these fluorescent dyes as function of temperature variation. The concentration used for Rh6G is 10^{-5} mol/L , the level of fluorescence was high which is normal since the concentration used is high too. The coefficient sensitivity is $-0.56\%/^{\circ}\text{C}$. Rh6G is a temperature independent dye but the response is not stable during the variation of temperature. We notice a decrease in this response after 40°C .

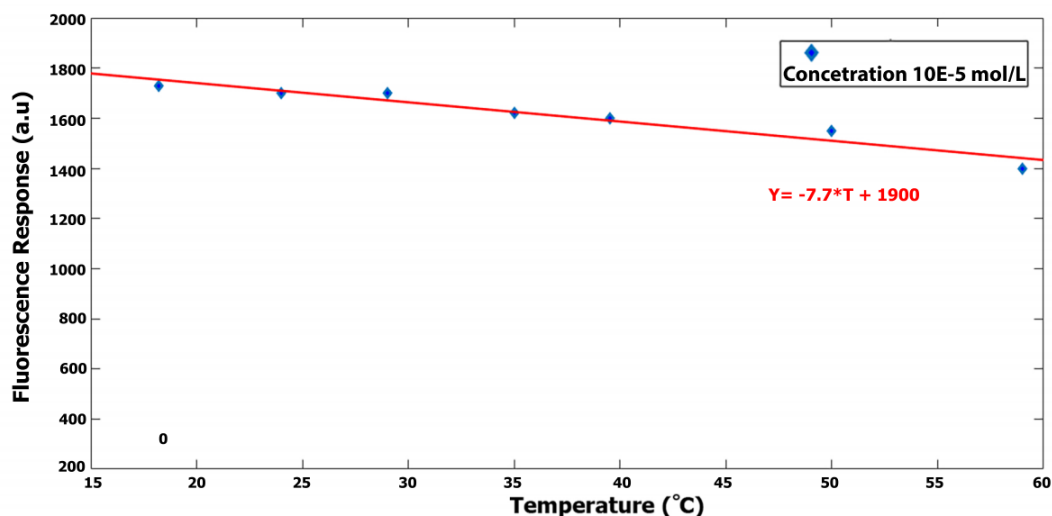


Figure 53: Response of Rh6G as function of temperature

Regarding RhWT, the coefficient sensitivity is $-0.50\%/^{\circ}\text{C}$ at a concentration of 10^{-6} mol/L . The response is approximately stable during the variation of temperature even at high values.

Regarding Ch-Na, it shows no variation in fluorescence response as a function of temperature. However the value of response is very low even at high concentration. We increased the concentration to 10^{-5} mol/L until the color of the solution was dark green. The coefficient sensitivity then was $-0.36\%/^{\circ}\text{C}$.

In conclusion, RhWT seems to be the best candidate among the others due to many reasons. Its fluorescence stability over temperature is better than that

of others, its sensitivity coefficient is lower than that of Rh6G. Although its sensitivity coefficient is higher than that of Ch-Na but from another aspect, a small concentration is needed for RhWT when compared to Ch-Na.

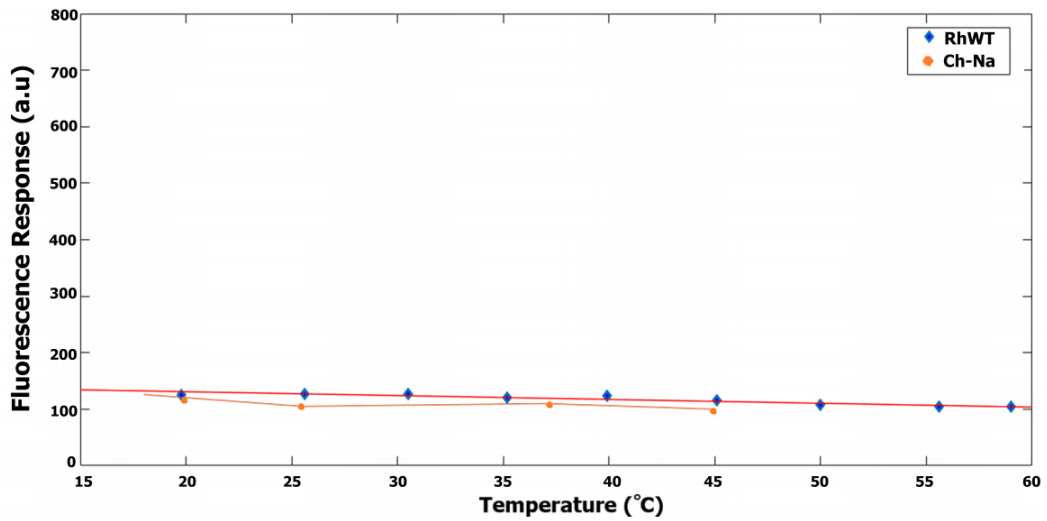


Figure 54: Response of RhWT and Ch-Na as function of temperature

4.5 Conclusion

The objective of this study is to find the adequate couple of dyes that will serve later for the 2c/2d LIF technique on the complex geometry. This was achieved by studying separately the response of each fluorescent dye as function of temperature. FL27 showed a more stable and consistent dependency on temperature when compared to classical fluorescein.

RhWT showed a fluorescence stability over temperature when compared to the other dyes in terms of sensitivity coefficient and its concentration.

In conclusion, FL27 will serve as a temperature dependent fluorescent dye and RhWT as temperature independent dye for the 2c/2d LIF technique.

Chapter 5

TABOULE & OLYMPE Facility

5 TABOULE & OLYMPE Facility

This chapter shows the design of the experimental facility on which the simultaneous measurements of temperature and velocity by LIF and PIV respectively were applied. The concept of this facility was created during the first year of this PhD work. It then took another year to implement and set it up completely to be ready for experimentation. This project is funded by CEA Cadarache (France). Chapter 5 is divided into several sections starting by the purpose of this facility and then explaining the geometry and the materials used in details

5.1 Purpose of the facility

The facility was constructed for the purpose of applying simultaneous measurements of velocity and temperature using PIV and LIF techniques on different fluid flows. Such measurements aim to study the complex mixing flows present in the MICAS mock-up (explained in chapter 2) since this geometry is made up of many cold and hot nozzles. A hydrodynamic study helps to identify models in large scale simulations in which the application of advanced models is limited by available computation resources. The mixing fluid flows are controlled by many parameters that affect the hydrodynamics of the fluid flow such as the flow rate, the temperature in the test section, the injection temperature and the distance separating them. These parameters control the dimensionless numbers such as Reynolds, Richardson and Froude number which allows us to study different fluid flows such as the negative, neutral and positive buoyant jets.

Table 9 shows a comparison between the different facilities ASTRID, MICAS mock-up and TABOULE in terms of geometry, some physical parameters and the measurement techniques applied on them.

Facility		ASTRID	MICAS	TABOULE
Length (m)	geometry	15 (diameter)	2.5 (diameter)	1 (length and width)
	Diameter nozzle	0.15	0.025(outer) 0.02 (inner)	0.025(outer) 0.02 (inner)
Flow rate		7900 kg/s	212 - 380 m ³ /hr	0.15 - 0.8 m ³ /hr
Dimensionless numbers	Re	1100000	46000	2000 - 40000
	Ri	0.028	0.028	0.0005 - 0.15
	Fr	0.18	0.18	0.04 – 0.22
Velocity measurements		Similitude with the MICAS	Intrusive: Propeller probes Non intrusive: PIV; LDV	Non intrusive: PIV
Temperature measurements		Similitude with the MICAS	Intrusive: Thermocouples	Non intrusive: LIF

Table 9: The different facilities ASTRID, MICAS mock-up and TABOULE

5.2 Construction of the facility

The facility consists of two loops shown in figure 55; a hydraulic loop called OLYMPE and a test section called TABOULE which stands for "Two-jet flow Analysis By Optical methods Using LasEr"

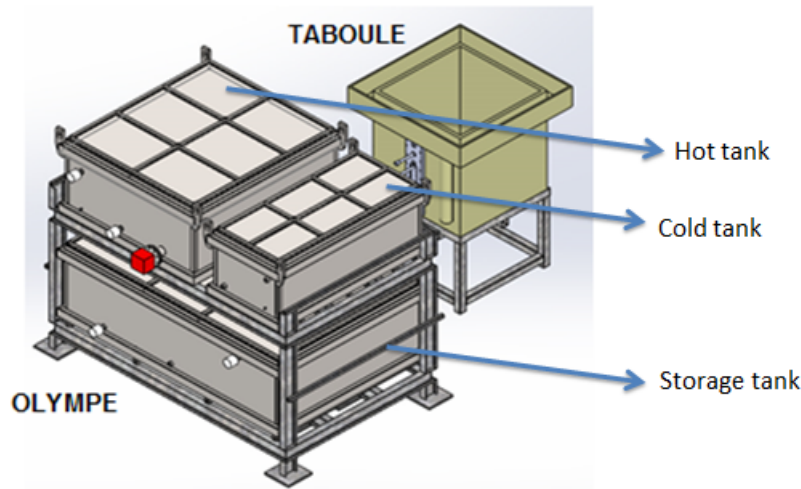


Figure 55: The experimental facilities TABOULE & OLYMPE

5.2.1 Geometry and specifications

TABOULE is a test section of volume $1m^3$ made up of three PMMA transparent faces for optical access. It consists of two transparent parallel nozzles of outer diameter 25 mm and inner diameter 20 mm . These diameters are identical to those of the nozzles found in the MICAS mock-up. Such an approach allows us to understand the hydrodynamics of the fluid flows in the mock-up. The two nozzles are constructed on a plate that allows us to vary the distance between them from 5 to 20 cm and to vary it horizontally and vertically to study different hydrodynamic cases. Also, similar spare plates were manufactured at the same time. For instance, the nozzles are fragile, so if one is damaged during an experiment, the plate can be changed and placed directly. As shown in figure 56, the top of the test section is equipped with an overflow tray. This serves to get identical exit conditions to achieve an unbounded medium in the experiments. The back flow of the fluid from the tray to the storage tank is connected opposite

to the non-transparent faces so as not to distort the optical access. Also, the bottom of the test section is equipped with a drain valve to empty it when needed.

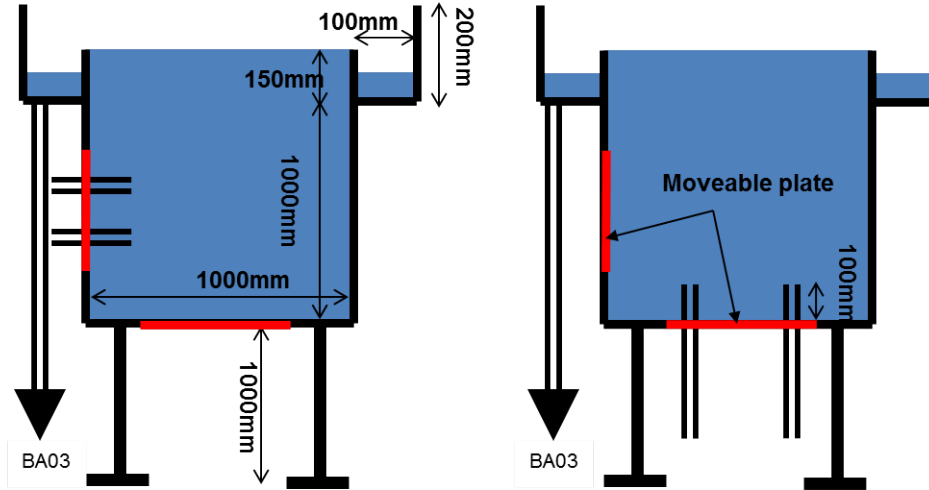


Figure 56: Geometry of the test section

Concerning the volume of the other tanks, the cold tank shown in figure 55 has a volume of 1 m^3 . It serves as a source of water at ambient temperature for the first nozzle in the test section TABOULE. The hot tank has a volume of 2 m^3 and the reservoir tank however is of volume 3 m^3 . The dimensions of the tanks are summarized in the table 10. De-ionized water is used in our experiments, then there is a risk of corrosion in the tanks. That is why the hydraulic loop is made up of stainless steel to prevent such a process.

Tank	Volume (m^3)	Length (mm)	Width (mm)	Height (mm)
Cold	1	1800	800	700
Hot	2	1800	1600	800
Storage	3	1800	2700	800

Table 10: Dimensions of the tanks

5.2.2 Immersion heater and sensors

An immersion heater (VULCANIC type 2400) of power 35 kW power is mounted on a flange in the hot tank as shown in figure 57. It allows heating the solution in the tank to cover up a maximum temperature of 60°C. It is regulated by a thermocouple immersed also in the tank. The hot and cold tanks are equipped with temperature sensors that allow us to know when to inject the solution in the test section. This assures uniform conditions in the test section. The reservoir tank however is of volume 3 m³ and is used either to fill up the other tanks or to empty them. All the tanks are equipped with drain plugs and with low and high level sensors. Two thermocouples are located on the cold and hot circuits very near to the parallel nozzle outlets.

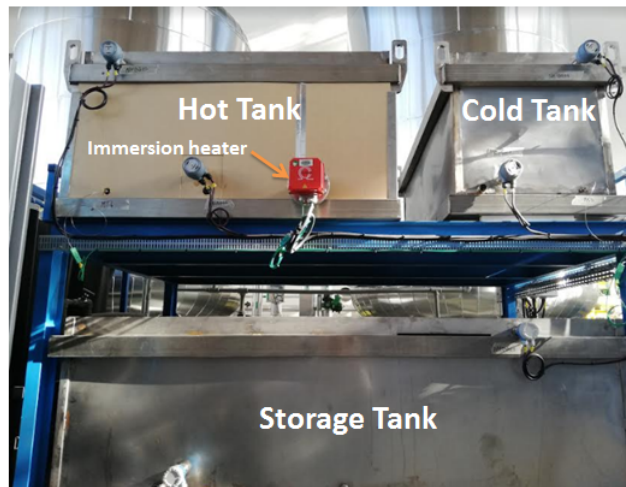


Figure 57: Specifications of the test section

5.2.3 Pumps used in the facility

Two volumetric pumps (Figure 58) with flexible impeller are used for the fluid flow from and into the hot and cold tanks. The maximum flow rate of 3 m³/h is varied from the speed of rotation of the pump. Such pumps serve to vary the flow rate in the range that gives different values for Reynolds number and thus different regimes from laminar to turbulent flow. A set of point valves are added too to this circuit of pumps to finely control the flow. The pump used for the storage tank is a centrifugal technology with a fixed flow rate of 15 m³/h. This pump with high flow rate was chosen so that to fill and empty the storage tank of volume 3 m³ quickly.

5.2.4 PID and notations

This section presents the piping and instrumentation diagram (PID) of TABOULE & OLYMPE used to control the process of experimentation. It is presented in figure 58. The notations and symbols of the equipment used in this diagram are summarized in table 11.

Symbol	Notation	Apparatus / Equipment
	PO#	Pump
	MQ#	Flow rate sensor
	MT#	Temperature sensor
	MDPO#	Pressure difference measurement
	MNBA03	Level measurement
	NHBA0#	High level sensor
	NBBA0#	Low level sensor
	VR#	Control valve
	VM#	Manual valve

Table 11: Symbols of the equipment used in this diagram

Notations

BA01 Cold tank

BA02 Hot tank

BA03 Reservoir tank

RECH Immersion heater used in the hot tank

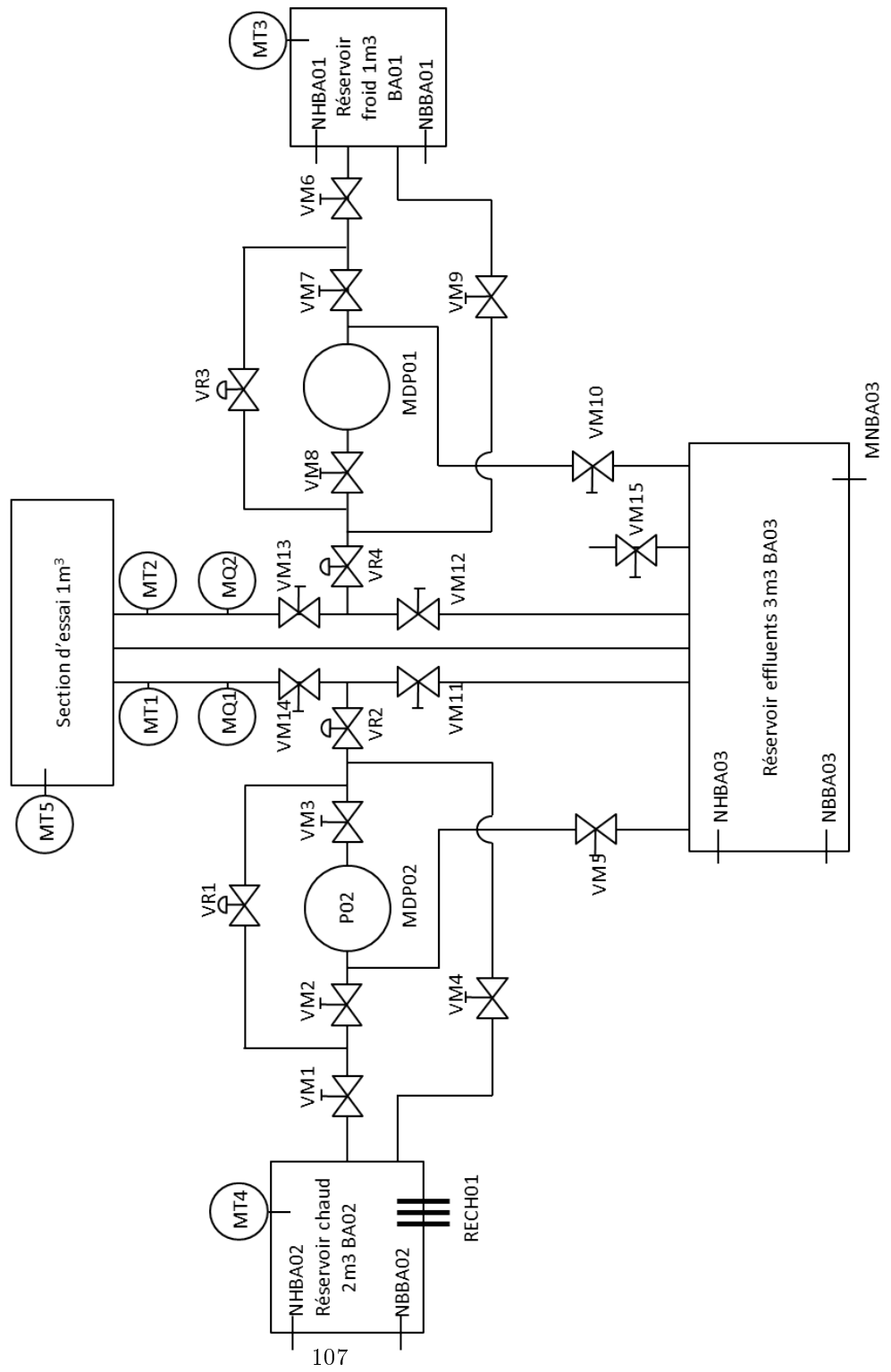


Figure 58: PID of the test section

5.3 Functioning of the loop

In a first step, the solution of fluorescent dyes or PIV particles is prepared. It is then injected in the reservoir tank to be properly mixed with de-ionized water. Then, using pump, a certain volume is sent from the reservoir tank to both the hot and cold tanks. By this way, the hot and cold tanks are of the same dye concentration. The solution in the hot tank is heated until 50°C using the immersion heater and is circulated in a closed loop using pump P02 to avoid overheating during the process of heating. At this point the loop is ready to perform the tests. The flow rate of the pumps are regulated at a rate depending on the objective of the experiments. Water in the test section returns to BA03 by gravity. The loop however is controlled by an electrical bay located near the tanks. All security is managed by this bay. An emergency stop button is located on the front near the control buttons. Figure 59 shows the test section TABOULE during preliminary preparations. Figure 60 shows the electrical bay where the values of the sensors are monitored and the temperature of the immersion heater is controlled.



Figure 59: Test section TABOULE



Figure 60: Electrical Bay

Chapter 6

Hydrodynamics and phenomenology of different fluid flows

6 Hydrodynamics and phenomenology of different fluid flows

6.1 Introduction and objectives

This chapter is dedicated to study the hydrodynamics of different fluid flows on the experimental facility TABOULE. The geometry of the two jets exhibits interesting features. That is why before starting the temperature and velocity measurements, simple experiments were done to analyze the flow dynamics of a single jet and the interaction between two jets. The experiments are done using a non reactive fluorescent dye RhWT at a very low concentration so that the flow dynamics are not affected due to the presence of the dye. The concept is to add uniquely solutions of RhWT in the cold and hot tanks and fill the test section just with de-ionized water. By this, the fluid flowing from the jets and containing a fluorescent dye penetrates the test section filled just with water. The camera used is a 12 bit camera of resolution 2048 by 2048 pixels and frequency 15 Hz. The spatial calibration measured indicated 445 pixels for 10 cm horizontally and vertically.

Figure 61 shows the geometry of the test section. The nozzles have a height of 100 mm, an outer diameter of 25 mm, an inner diameter of 20 mm, and are separated by a distance of 50 mm.

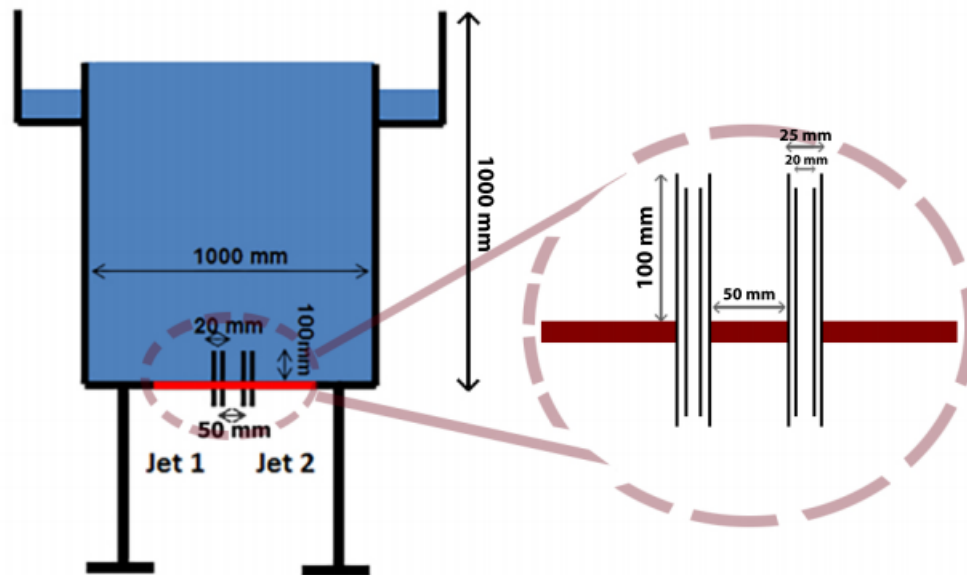


Figure 61: The test section zoomed at the two nozzles

In Figure 61, we consider that the jets are far away from the wall of the test section as the ratio of the jet diameter to its distance to the wall is 0.04. We can assume that the medium of experimentation is unbounded in all the tested configurations. In most of the cases, the height of the jet penetration was measured as function of time using the video recorder of the flow visualization as seen in the following sections.

Such experiments allow to visualize the characteristics of different input fluid flows such as positive and negative buoyant jets. A positive buoyant jet occurs when the fluid is injected upward into a higher density fluid or downward into a lower density fluid. A negative buoyant jet occurs when the fluid is injected upward into a lower density fluid or downward into a higher density fluid.

The dimensionless numbers used for these calculations are Reynolds, Richardson and the discharge Froude numbers. A positive discharge Froude number represents a positive buoyant jet whereas a negative discharge Froude number represents a negative buoyant jet. This definition of the discharge Froude number is used in our experiments.

Figure 62 shows a summarized graph for different fluid flows: jet (neutral or positive buoyant jet), plume (positive buoyant jet) and fountain (negative buoyant jet) using the values of Richardson numbers for the first fluid flow (Ri_1) and for the second one (Ri_2).

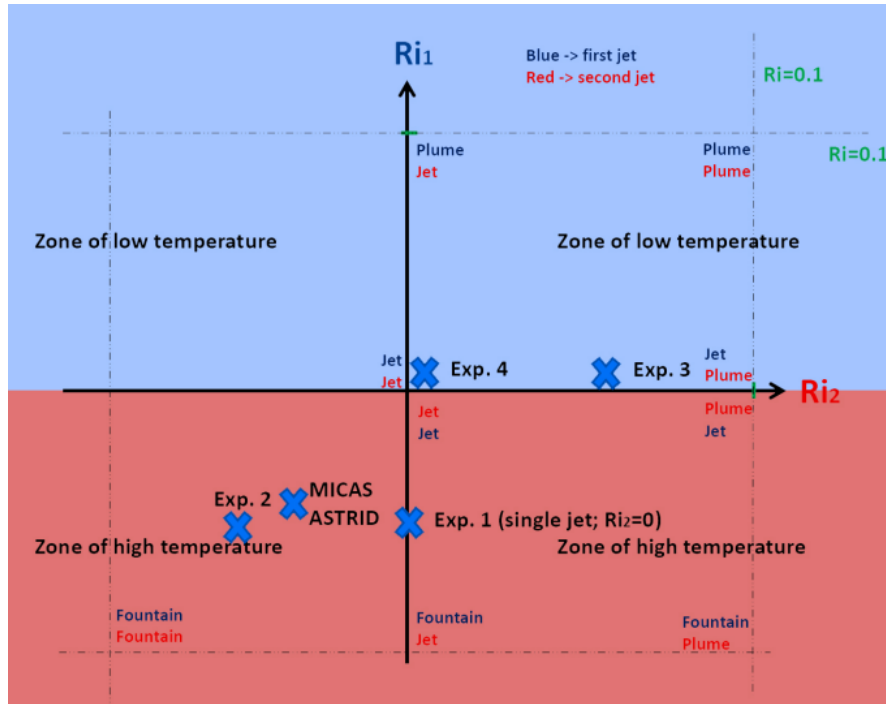


Figure 62: An experimental graph for different fluid flows

The behavior of the fluid flow will depend on the temperature of the surrounding fluid. So, we differentiate two zones related to the surrounding fluid; the first one is at low temperature (about 20°C ; zone above the Ri_2) and the second one is at a high temperature (zone below the Ri_2). In the zone of low temperature, it is usually the case of either positive or neutral buoyant jets. The range of Richardson number is between 0 and 1 according to Carazzo et al. [108, 120]. If the injection temperature is ambient (similar to the surrounding), then the fluid flow is a neutral buoyant jet and Richardson number is null. However, if the injection temperature is higher than the surrounding, then the fluid flow is a positive buoyant jet. In this situation if the flow rate is low, the fluid flow ends by a plume whereas it maintains the upward flow if the flow rate is high. In the high temperature zone, the fluid flow is a negative buoyant jet instead of being positive as shown in the figure 62. The different behavior flows were just indicated on the right part of the y-axis because the other ones are symmetrical. For instance, if we start by the case of Jet (blue) / Jet (red) situation, along the x-axis and with the increase of Ri_2 to its critical value (0.1), this neutral or positive buoyant jet (Red) will end up by a plume since its flow rate is low. However, the fluid flow of the Jet (blue) will maintain its form because Ri_1 remains constant.

The objectives of this chapter is to study the physics of the buoyant jets, the different phases of their penetration into the unbounded medium, the maximum height reached, the width of the jet and the interaction between two jets. This chapter is divided into three main sections; the first is dedicated to show the initial conditions and some calculations, the second for results and the last section is dedicated to state the analysis and comments regarding the results with comparison to literature review.

6.2 Initial conditions and calculations

In the experiments, temperature is the main variable. Figures 63 and 64 show the variation of density and viscosity respectively as function of increase in temperature. These values will be used later during the calculations.

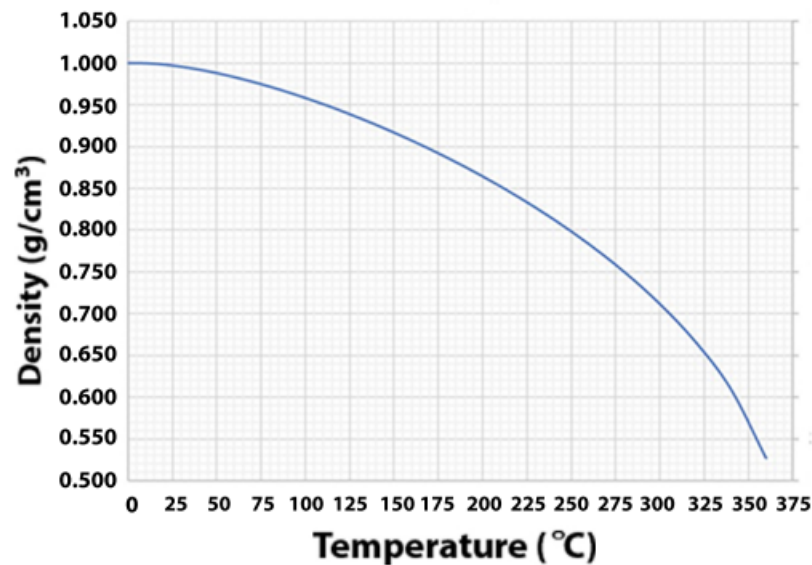


Figure 63: Variation of density of water as function of temperature (Engineering toolbox)

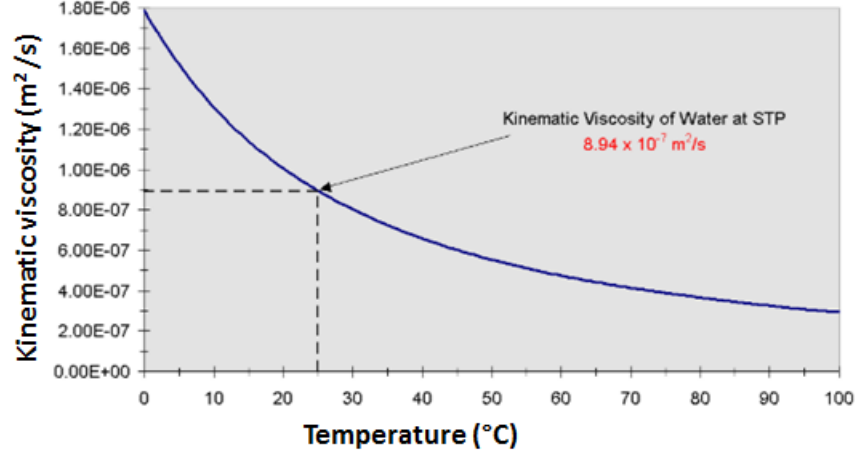


Figure 64: Variation of viscosity of water as function of temperature (Engineering toolbox)

Re , Ri and Fr_d are calculated in each case; we also introduce in this study the momentum and buoyancy flux which are used to find the penetration height scale and the time scale through which different fluid flows can be compared and studied. First, Turner [77] and Baines et al. [118] showed that the flow depends only on the momentum and buoyancy at the source when the radius of the outlet jet is small compared to the penetration of the jet which the case here. In addition to this, during the spread of a negative buoyant jet, buoyancy force and momentum compete. Thus, these variables shape the spread of the fluid flow in the unbounded surrounding.

The equations for the momentum and buoyancy flux are presented below. The height and time scales were derived from equations (33) and (34) using dimensionless analysis. These scales are valid for over a wide range of discharge Froude numbers for either positive or negative buoyant jets (Pantzlaff et al. [109]).

Momentum Flux

$$M = \pi r^2 U^2 \quad (33)$$

Buoyancy Flux

$$B = \pi \left[g \left(\frac{\rho_e - \rho_0}{\rho_0} \right) \right] r^2 U \quad (34)$$

Penetration height scale

$$H = hM^{-3/4}B^{1/2} \quad (35)$$

Time scale

$$T' = tM^{-1}B \quad (36)$$

where r is the radius of the nozzle, h is the penetration height and t is the time of fluid flow penetration.

Table 12 shows the experimental matrix including the calculations for different flow rates 0.15 and 0.8 m^3/hr . These values were chosen to cover a range of Reynolds number that varies from laminar to turbulent flow.

Experiment	Temperature in test section (°C)	Temperature Jet 1 (°C)	Temperature Jet 2 (°C)	Flow rate (m ³ /s)	Reynolds		Discharge Froude		Richardson	
					Re1	Re2	Fr1	Fr2	Ri1	Ri2
1	45	17	X	0.15	2640	No injection	-21.2	No injection	-0.047	No injection
2	45	17	25	0.15	2640	3000	-21.2	-17.47	-0.047	-0.057
3	20	17	43	0.15	2640	4773	undefined	21.2	null	0.047
4	20	17	43	0.8	14000	25400	undefined	289	null	0.0035

Table 12: Experimental matrix with some parameters

Those different configurations are reported on the the graph of figure 62.

6.3 Results

This section presents the raw results. The analysis is shown in the next section.

6.3.1 Experiment 1: Single negative buoyant jet at $Re=2640$ and $Fr_d=-21.2$

The fluid at ambient temperature 17°C is injected into a surrounding at high temperature (45°C) at a flow rate of $0.15\text{ m}^3/\text{hr}$. This gives a Reynolds of 2640 and discharge Froude number of negative 21.2. The fluid flow was recorded and the figures 65 and 66 show the spread of the flow at different instants. The area under the jet outlet is not considered for the analysis because the shape of the tube changes the the light path. The results in this location are not relevant.

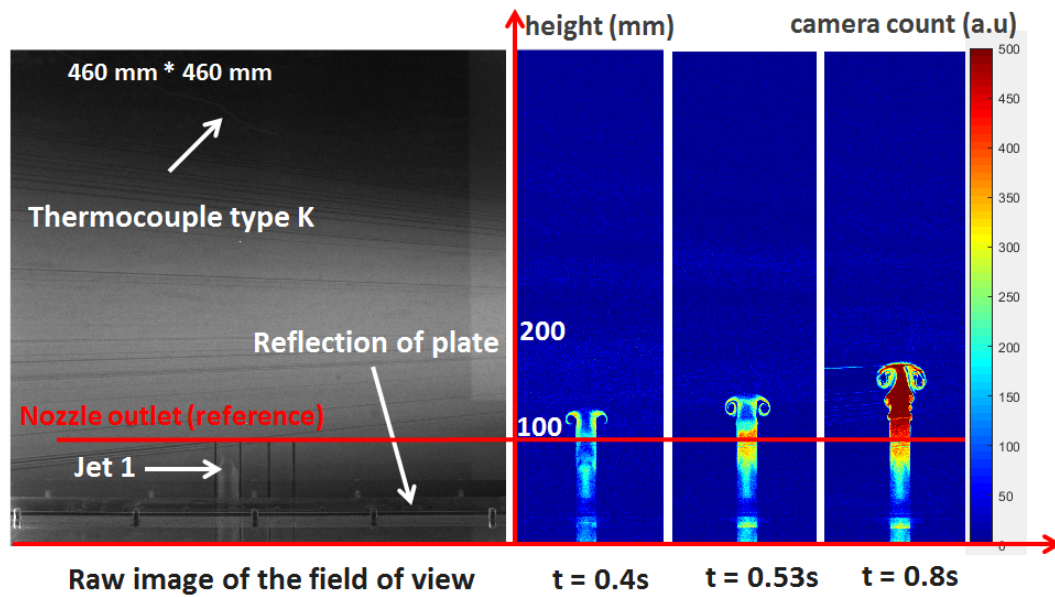


Figure 65: Evolution of the negative buoyant jet

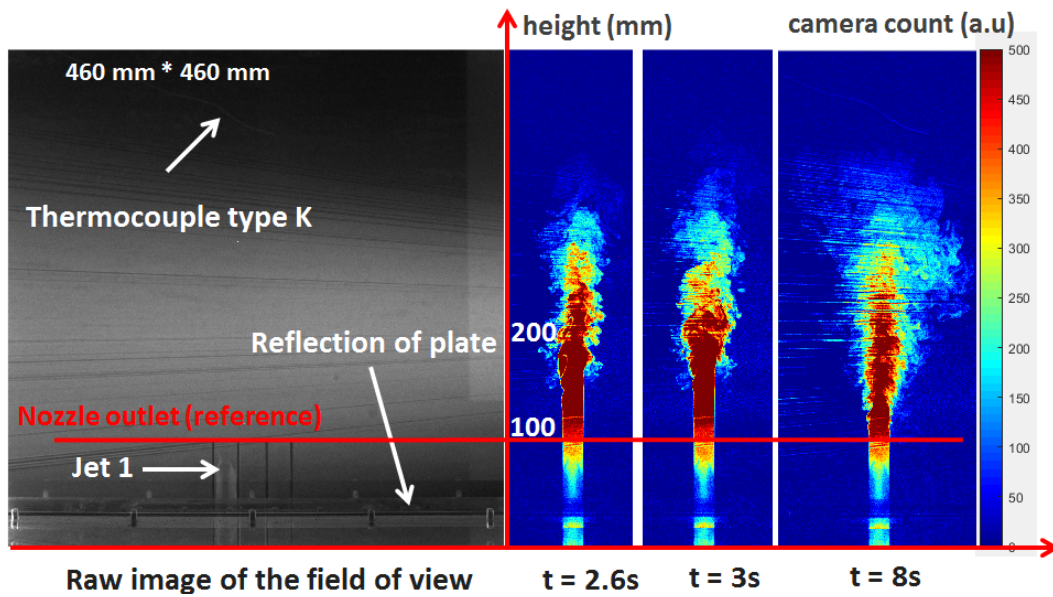


Figure 66: Evolution of the negative buoyant jet

**6.3.2 Experiment 2: Two negative buoyant jets both at $Re_1 = 2640$,
 $Fr_{d1} = -21.2$ and $Re_2 = 3000$, $Fr_{d2} = -17.47$**

The temperature in the test section is $45\text{ }^\circ\text{C}$ in this situation. The first injection was done at temperature $17\text{ }^\circ\text{C}$ and flow rate of $0.15\text{ m}^3/\text{hr}$. The second injection was at temperature $25\text{ }^\circ\text{C}$ and a flow rate of $0.15\text{ m}^3/\text{hr}$. The fluid flow was recorded and figures 67 and 68 show the spread of the flow at different instants.

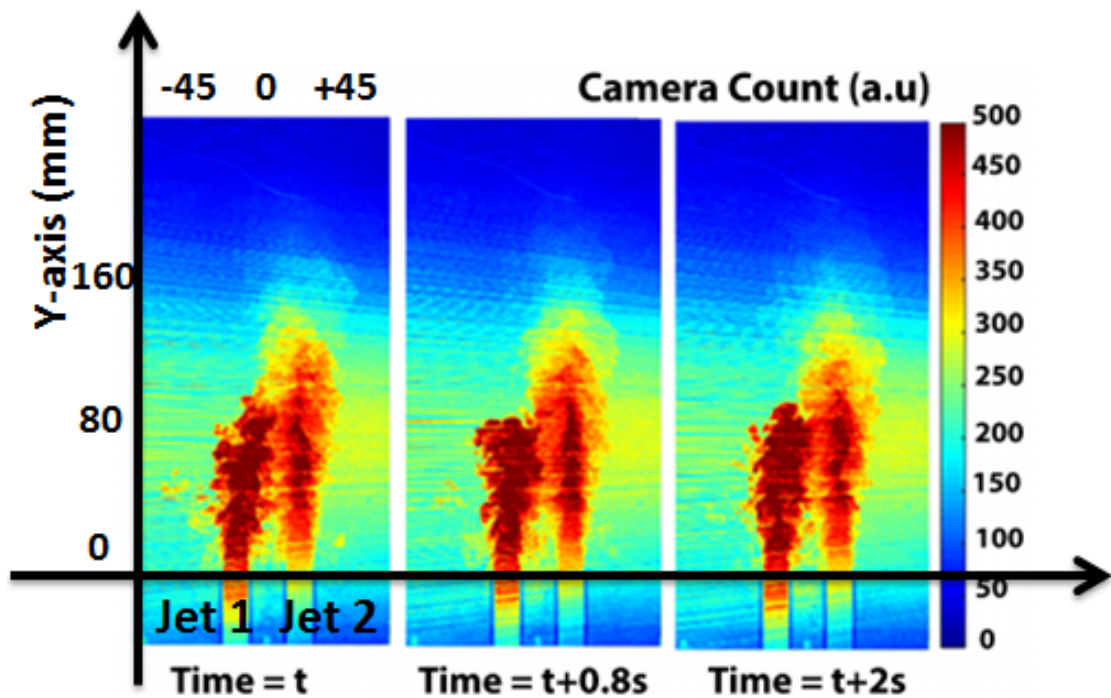


Figure 67: Evolution of the two negative buoyant jets, part 1

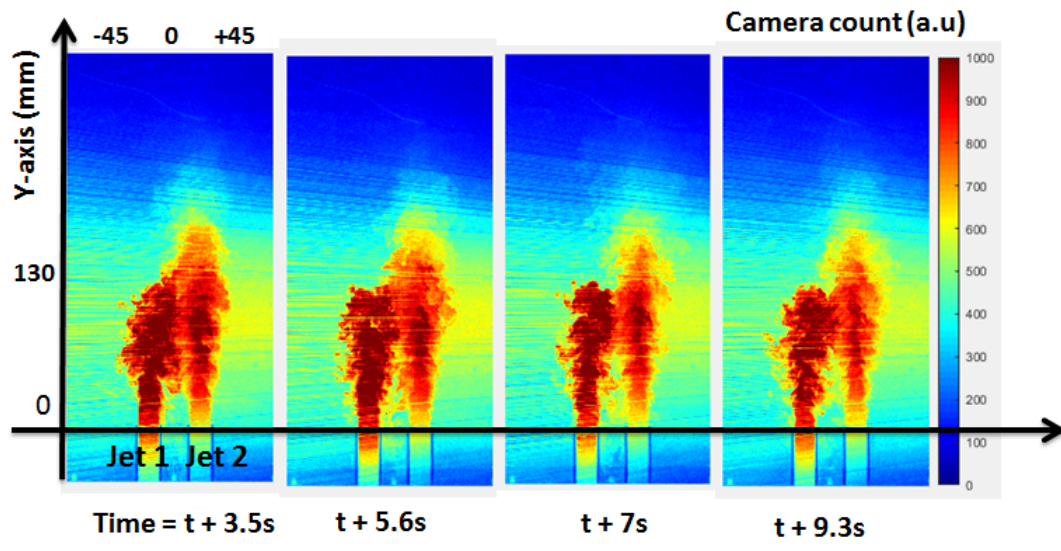


Figure 68: Evolution of the two negative buoyant jets, part 2

6.3.3 Experiment 3: Positive and neutral buoyant jets at $Re_1 = 2640$ and $Re_2 = 4773$, $Fr_{d2} = 21.2$

Experiment 3 was done after experiments 1 and 2 without emptying the test section. Since we are applying such experiments on a large volume, it is not practical to empty the test section at each time and clean it well. The test section is already filled with de-ionized water and RhWT at unknown concentration. In order to visualize the flow, we added again concentrated solution of RhWT to the hot and cold tanks. The drawback in such a case is not getting clear images as the previous cases after image treatment because the difference in concentration between the jet and the surrounding fluid is lower than that of the previous cases. The test section was at ambient temperature (20 °C). The first injection was at temperature 17 °C and flow rate of $0.15 \text{ m}^3/\text{hr}$. The second injection was at temperature 43 °C and flow rate of $0.15 \text{ m}^3/\text{hr}$. The spread of the flow at different instants is shown in figure 69. However, we were not able to record exactly the starting point of the injection of the two jets. Thus, we suppose t as a reference time instant in this situation.

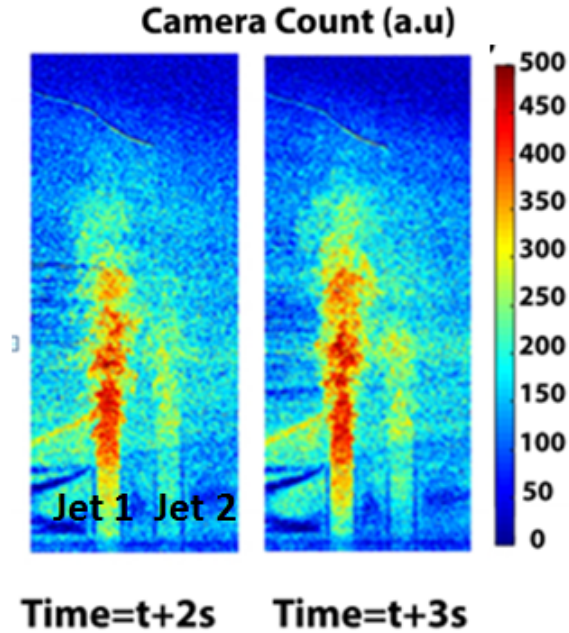


Figure 69: Evolution of the two fluid flows

6.3.4 Experiment 4: Positive and neutral buoyant jets at $Re_1 = 14000$ and $Re_2 = 25400$, $Fr_{d2} = 289$

The test section was at ambient temperature (20 °C). The first injection was at temperature 17 °C and flow rate of $0.8m^3/hr$. The second injection was at temperature 43 °C and flow rate of $0.8m^3/hr$. The spread of the flow at different instants is shown in figures 70 and 71. However, we were not able to record exactly the starting point of the injection of the two jets. Thus, we suppose t is a reference time instant in this situation just like that in experiment 3.

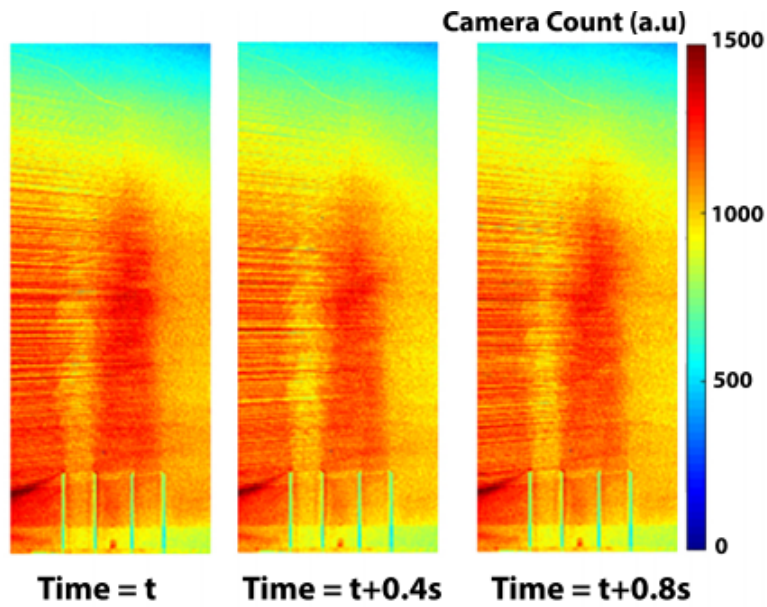


Figure 70: Evolution of the two fluid flows

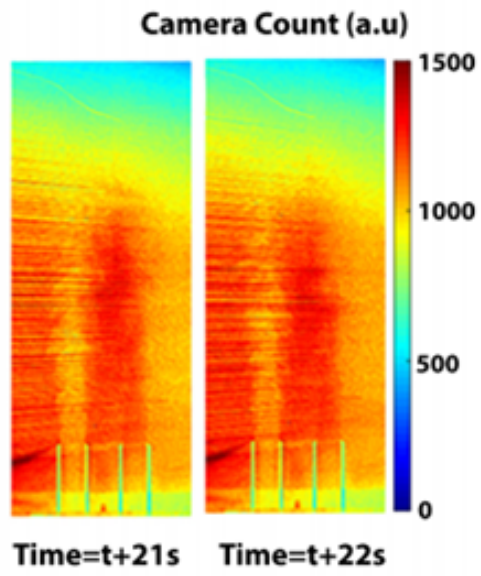
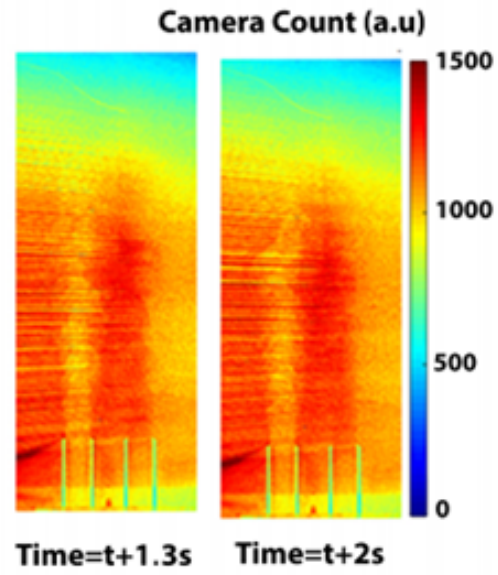


Figure 71: Evolution of the two fluid flows

6.4 Analysis and comparison with literature

6.4.1 Experiment 1: Single negative buoyant jet at $Re = 2640$ and $Fr_d = -21.2$

The Reynolds number in this case is 2640 and the discharge Froude number is negative of value 21.2. The fluid flow is a turbulent fountain since a dense fluid is ejected into a lower density environment. This fountain starts as two symmetrical vortex rings and then continues to flow into the fluid of the test section. The starting jet decelerates due both to the entrainment of surrounding fluid and to the negative buoyancy force. So it passes by three main stages. It penetrates to its maximum height in the surrounding medium, then decreases and finally fluctuates around a mean value of the maximum height of penetration. There is an interaction between the second and the third phase because of the upward and downward flows which restrict the rise of the jet again. This reduces immediately the initial penetration height to a smaller steady value (established flow). The different phases are shown in section 6.3.1. Since the Reynolds number is low, the flow is expected to be laminar to transitional. Concerning the comparison with experiments found in literature, the maximum height reached by a round fountain at low Reynolds follows the scaling shown in equation (37) and that at high Reynolds is given by equation (38). However, the range of Reynolds number was not well precised and the values of n and p varied from one study to another. Table 13 summarizes the literature review and the values of n and p found in each to compare it with the value we calculate later.

$$\frac{h_m}{r} \sim Fr_{d0} Re_0^n \quad (37)$$

$$\frac{h_m}{r} \sim Fr_{d0}^p \quad (38)$$

where h_m is the maximum penetration height, Fr_{d0} and Re_0 are calculated at the injection velocity U_0 .

Reference	Fr_{d0}	n	Reference	Fr_{d0}	p
Lin & Armfield (2000b)	< 1	$-2/3$	Hunt (2006)	< 1	$2/3$
Lin & Armfield (2000a)	< 1	0	Hunt (2006)	$1 < Fr_{d0} < 10$	2
Lin & Armfield (2003)	< 1	$-1/2$	Zhang et al (1998)	general	1.3
Philippe et al. (2005)	> 1	$1/2$	Lin & Armfield (2004)	general	1
Williamson et al. (2008)	> 1	$1/2$	Lin & Armfield (2008)	general	1.5

Table 13: Literature review

In this case, to calculate the value of n , h_m should be known. Figure 72 shows the variation of the jet penetration height as function of time. The 'diamond' variables are the real values of the penetration height and the red curve is a fit regression of the values obtained. This curve however validates the fact that the jet penetrates to its maximum height and then decreases due to the downward back flow of denser solution surrounding the jet which reduces its upward momentum. The maximum penetration height (h_m) reached by the jet in this case is about 265 mm and the height of the established flow (h_s) is about 187 mm. This value of fluctuation is 70.5% of the maximum height of injection, a value similar to that found by Pantzlauff et al. [109] (71%). Going back to the equations, we get a value of 0.028 for n from equation (37) whereas a value of 1.07 from equation (38) for p . We got a value of p similar to that found by Lin & Armfield (2004) [121] which was 1. Their study in 2004 was done for fountains with intermediate Froude and Reynolds numbers ($1 \leq Fr_d \leq 20$ and $1000 \leq Re \leq 3000$). These conditions are similar to ours in this experiment. That is why equation (38) seems to be best fitting in this situation. This analysis was done on one experiment. Other experiments can be carried out at different discharge Froude number to validate the results of the studies listed previously.

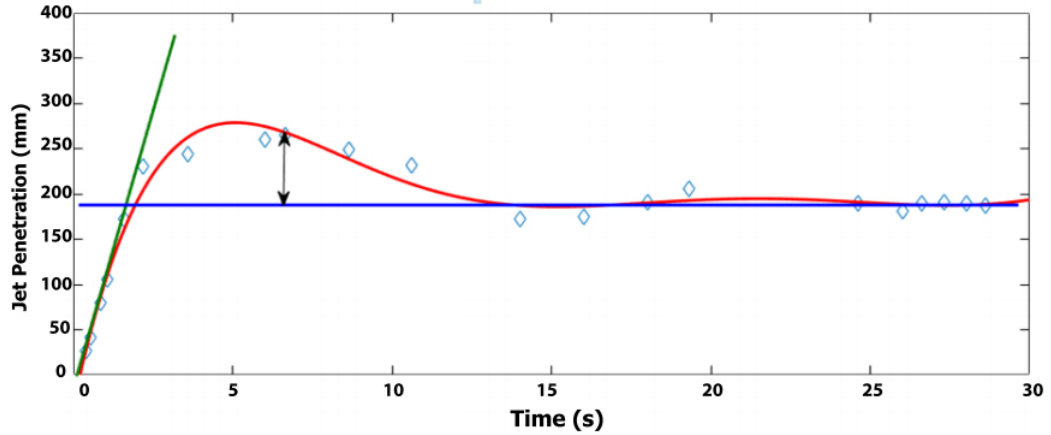


Figure 72: The jet penetration curve as function of time

The first points on the curve of figure 72 show a linear behavior. That is why we plot the green line in this figure. It is used to calculate the penetration velocity during phase one (U_1) so that we compare it with the upward injection velocity (U_0). From figure 73, U_1 has a value of 0.1 m/s which is approximately

similar to U_0 , 0.132 m/s (calculated from the flow rate and the diameter of the nozzle).

The blue line shows the established height of penetration of the jet which is around 187 mm and is reached after time 14 s . Turner [77] showed that the established height reached by the negative buoyant jet is handled using the predictions of the initial maximum height as shown in equation (39).

$$\frac{h_m}{h_s} \sim 1.43 \quad (39)$$

In our case, the ratio of $\frac{h_m}{h_s}$ is 1.42 , a value consistent with that found by Turner [77] and Pantzlaff et al. [109]. h_m can also be expressed using the discharge Froude number and the nozzle diameter D according to equation (24) related to figure 24. From our experiment, $\sqrt{-Fr_d}$ has a value of 4.6 which gives a value of about 10 for $\frac{h_m}{D}$ from figure 25 related to the study done by Mizushina et al. [76]. This value however is a little lower than that found in our experiment which is 13.25 .

The following paragraph deals with the variation of the penetration width at the different phases of the spread. Figures 73 and 74 show the different graphs plotted along the x-axis to compute the width of the fluid flow.

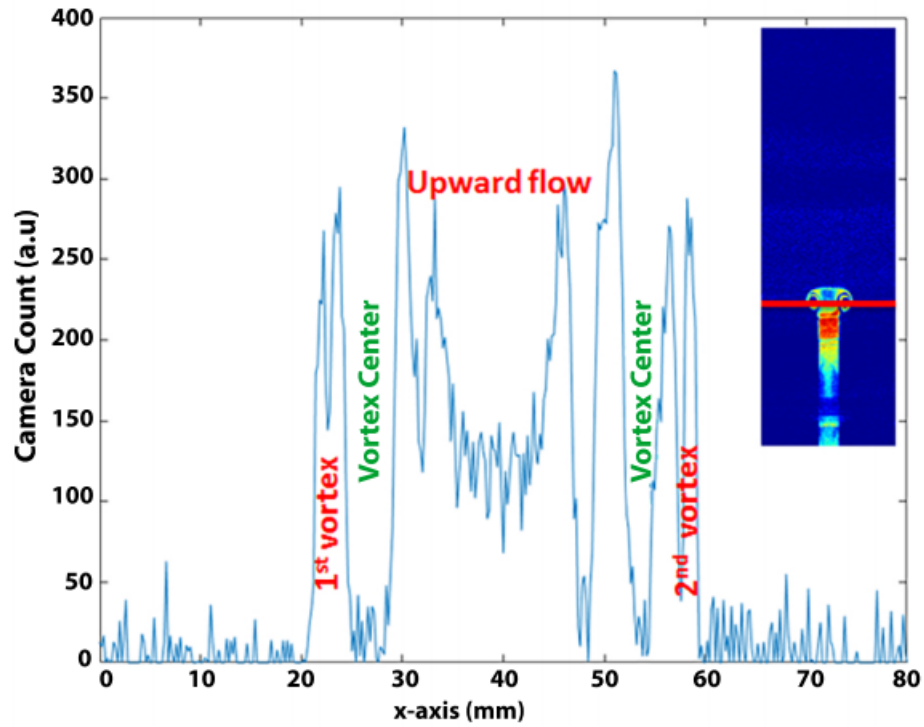


Figure 73: Graph plotted along the x-axis at time 0.6 s, position red line

The fluid flow starts spreading as two symmetrical vortex rings of a diameter about 40 mm. After this, it spreads maintaining the same width which is equal to the nozzle diameter (red curve) along a height equal to that of the nozzle, and then it reaches its maximum height of penetration.

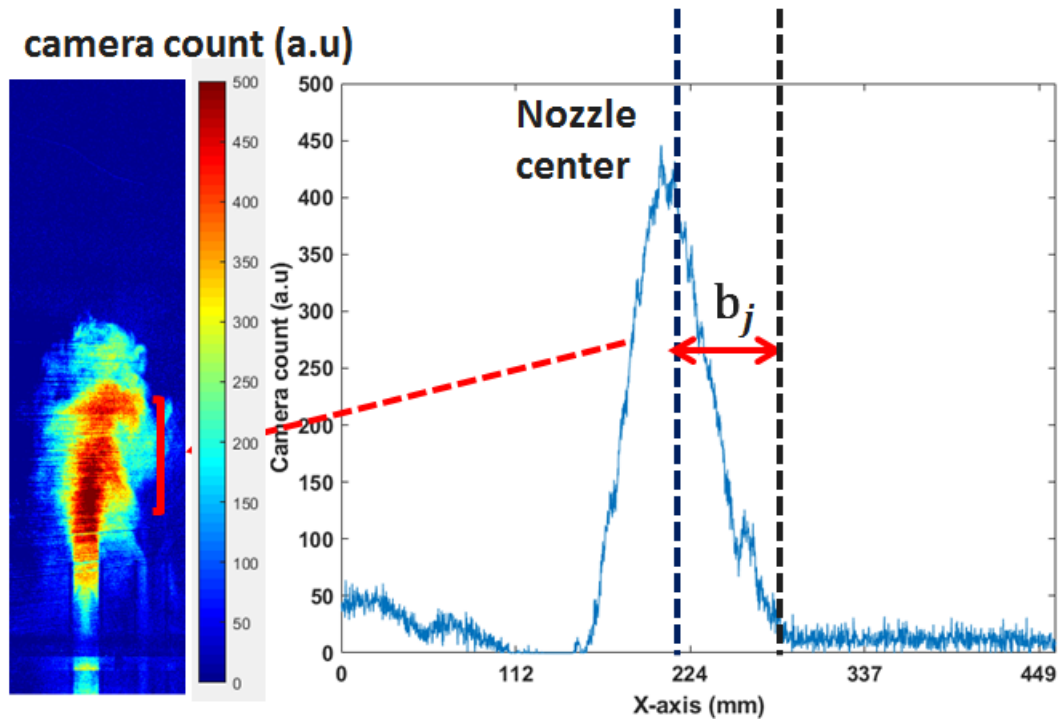


Figure 74: The time average over 75 images during the established phase

Figure 74 shows the time average over 75 images during the established phase from 25 to 30 s. The width b_j of the fluid flow reaches a value about 56 mm. However, equation (23) gives a value of 34 mm for b_j , a value larger than that found in our experiments. So, the study done by Mizushima et al. [76] does not fit the values we got regarding h_m and b_j . This can be due to the conditions of the experiments done in what concerns the diameter of the nozzle, the solution used (brine solution or water) or the geometry of the test section.

**6.4.2 Experiment 2: Two negative buoyant jets both at $Re_1 = 2640$,
 $Fr_{d1} = -21.2$ and $Re_2 = 3000$, $Fr_{d2} = -17.47$**

The temperature in the test section is 45°C. The first injection was at temperature 17 °C and flow rate of 0.15 m³/hr. This gives a Reynolds value of 2640 and a negative discharge Froude number of 21.2. The second injection was done at temperature 25 °C and flow rate of 0.15 m³/hr. The Reynolds number for this fluid flow is 3000 and the discharge Froude number is a negative 17.47.

Both fluid flows are negative buoyant jets, but each at a different discharge Froude numbers. In this situation, graphs are plotted to get the maximum height of penetration of each jet, the interaction between the two and finally to compare the case with the single negative buoyant jet. Figure 75 shows the jets at time $t + 3.3s$, the lines indicate different positions above the nozzle injection in which graphs (figures 76 and 77) were plotted at each of these indicated positions. Jet 1 is noted as the negative buoyant jet of Froude number of -21.2 and jet 2 that of Froude number of -17.47.

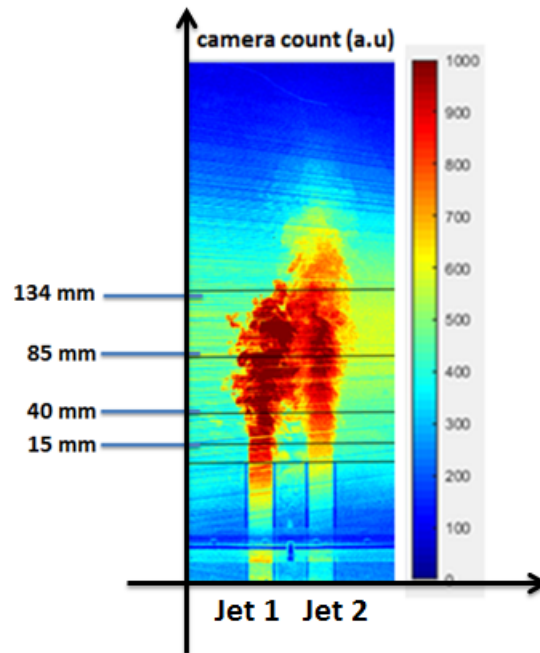


Figure 75: The lines indicate the position of graphs along the y-axis

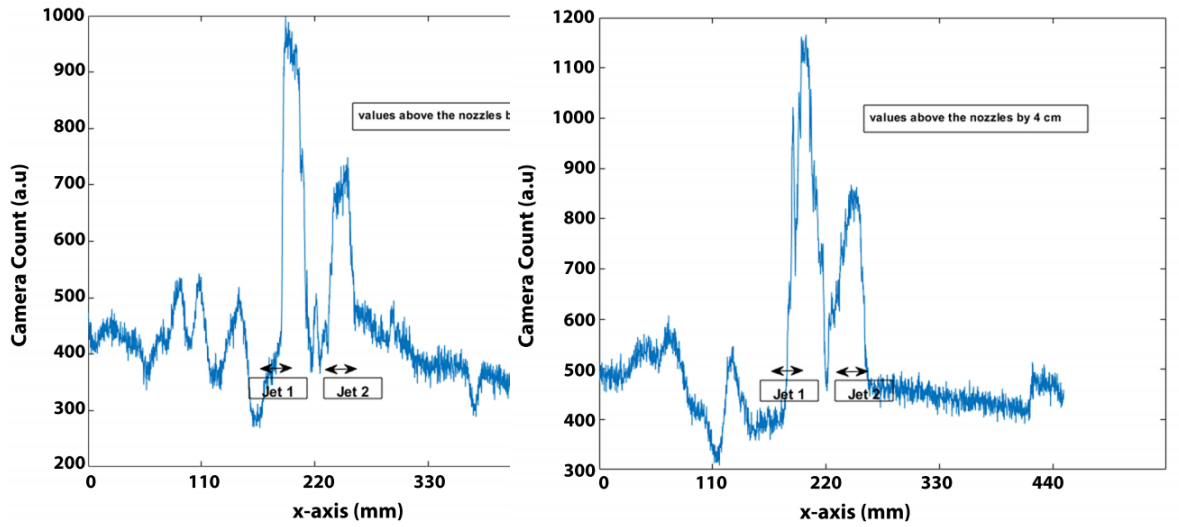


Figure 76: Plot of values along the x-axis at positions 15 and 40 *mm*

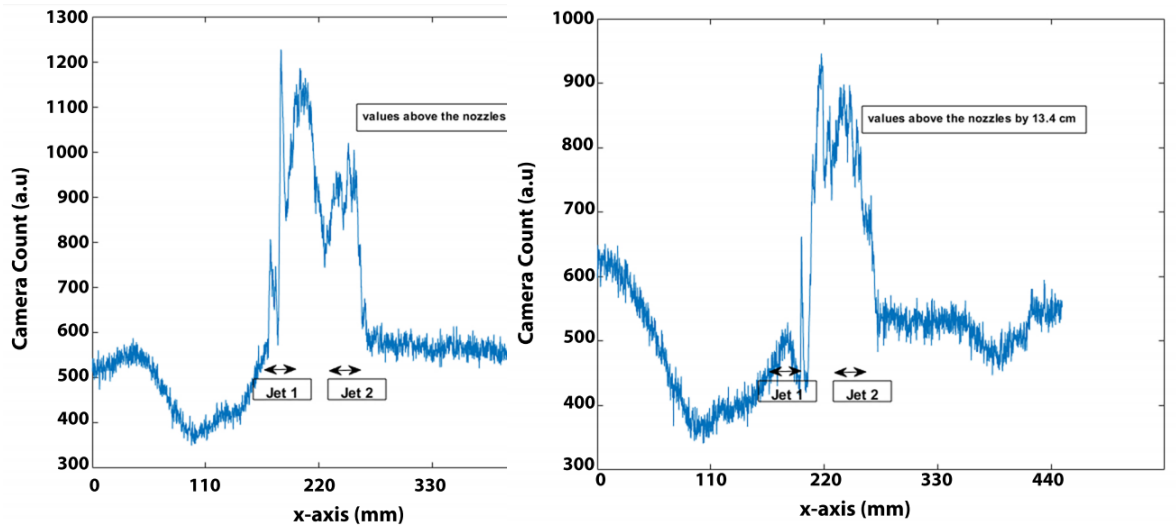


Figure 77: Plot of values along the x-axis at positions 85 and 135 *mm*

From the graphs, jet 2 spreads higher in the medium than that of jet 1. This is because the competition between the buoyancy and momentum flux in jet 2

is lower than that in jet 1. This is shown by the peaks in figures 76 and 77 in which the peak reached by jet 1 is higher than that of jet 2. Then, both jets interact drawing the flow downwards in a clockwise direction along jet 1 and anticlockwise along jet 2. This interaction is approximately along all the height of penetration of jet 1.

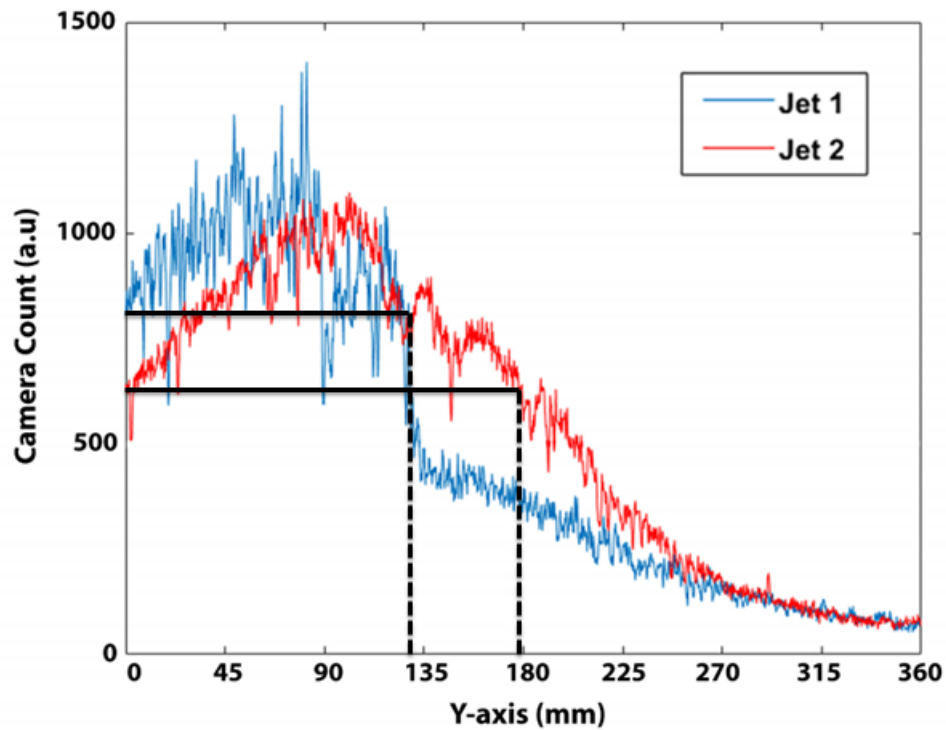


Figure 78: Evolution of the two fluid flows at the centerline of each nozzle

The maximum height of penetration of jet 1 is about 130 *mm* and that of jet 2 is about 180 *mm* as obtained from figure 78. It is interesting to compare this case with that of single negative buoyant jet (experiment 1). Both jets 1 have the same conditions of injection, but the value of h_m in this case (130 *mm*) decreased by approximately the half when compared to that of experiment 1 (265 *mm*). This is due to the interaction with jet 2 which decreases its height of penetration.

6.4.3 Experiment 3: Positive and neutral buoyant jets at $Re_1 = 2640$ and $Re_2 = 4773$, $Fr_{d2} = 21.2$

The temperature in the test section is 20°C in this experiment. The first injection was done at a temperature of 17 °C and flow rate of 0.15 m^3/hr which gives a Reynolds value of 2640. However, the second injection was done at a temperature of 43°C and flow rate of 0.15 m^3/hr which gives a Reynolds value of 4773 and a positive discharge Froude number of 21.2. In this experiment, the first fluid flow acts as a neutral buoyant jet because of the very low temperature difference between the fluid flow and the surrounding water. The second fluid flow acts as a positive buoyant jet because the fluid is injected upward into higher density fluid (colder surrounding). So the buoyancy force and jet momentum have the same sense.

Just like the case of a negative buoyant jet, three phases of the spread can be identified in the case of a positive buoyant jet. In the region near the nozzle exit, the jet momentum dominates and the flow is similar to a neutral buoyant jet. Far from the jet exit, the buoyancy dominates, and the flow acts like a plume. The intermediate region however is a transition between jet flow and plume flow. However, the second and the third phase of spread depend on the flow rate of injection which directly affects the momentum force of the spread. For instance, if the flow rate is high, then the momentum is significant so the flow is a certain positive buoyant jet. Inversely, if the flow rate is low, then buoyancy force is dominant so the flow acts as a plume. In this situation, the flow rate is 0.15 m^3/hr which is assumed low, so apparently the positive buoyant jet will end up by forming a plume. Analyzing figure 79, the neutral buoyant jet which has a Reynolds of 2640 spreads linearly with the jet centerline which is the upstream distance from the point source. The positive buoyant jet spreads linearly then during the transition phase, buoyancy becomes significant so it then spreads like a plume. We were not able to explicit these results into graphs because the values were biased. This is because the test section had already a mixture of water and RhWT before injection. So unlike the previous cases, this will not give a fine analysis for this experiment.

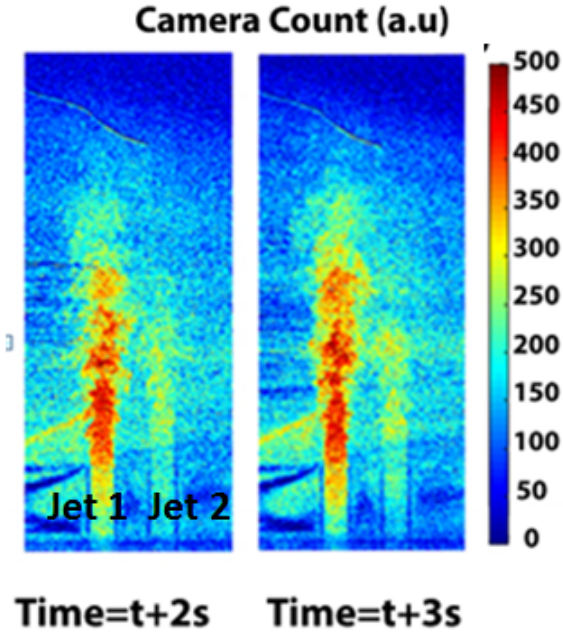


Figure 79: Evolution of the two fluid flows

6.4.4 Experiment 4: Positive and neutral buoyant jets at $Re_1 = 14000$ and $Re_2 = 25400$, $Fr_{d2} = 289$

The temperature in the test section is ambient in this experiment just as that before. The first injection was done at a temperature of $17\text{ }^\circ\text{C}$ and flow rate of $0.8\text{ m}^3/\text{hr}$ which gives a Reynolds value of 14000. This fluid flow acts as a neutral buoyant jet since there is no significant temperature difference between the injection and the surrounding. However, the second injection was done at a temperature of $43\text{ }^\circ\text{C}$ and flow rate of $0.8\text{ m}^3/\text{hr}$ which gives a Reynolds value of 25400 and a positive discharge Froude number of 289. This jet is a positive buoyant jet since the fluid is injected upward into a colder surrounding as shown in figure 80. When comparing the results in this situation to those obtained in the previous section, we can see that positive buoyant jet spreads linearly and higher than before. It does not end as a plume, however it maintains the shape of the jet. This is due to the high flow rate which allows the momentum force to dominate that of buoyancy. There seems to be no interaction between the two fluid flows. The first fluid flow spreads with a width ranging between D and $2D$ however that of the second maintains the diameter of the jet D . Also in this experiment, we were not able to explicit the results into graphs because

the values we got were biased.

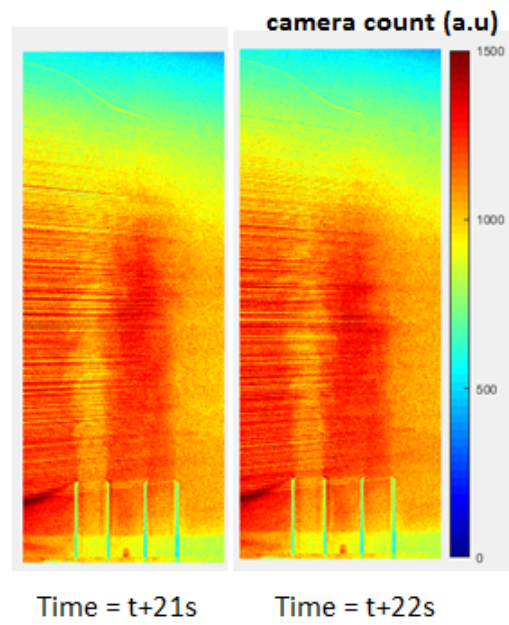


Figure 80: Evolution of the two fluid flows

Chapter 7

LIF & PIV on the complex geometry (TABOULE)

7 LIF and PIV on the complex geometry (TABOULE)

From the previous studies on the simple geometry facility presented in chapter 4, we get enough data to carry on experiments on the complex geometry.

This chapter is divided into two main sections. In the first, we present the installation of the optical measurement techniques and the complexities faced during this process.

In the second part, we present the experiments of PIV and LIF done along with the results.

7.1 Installation of LIF & PIV and the complexities faced:

Passing from a volume of 30 L into a larger volume of 1000 L (TABOULE test section), the application of optical measurements gets more complex. First, the solution of fluorescent dyes and PIV particles was prepared for a volume of 3.5 m^3 which is the total volume of the test section and the other tanks (the OLYMPE loop). By this, the solution is homogeneous and the concentration of the dyes is constant so that to measure uniquely temperature (not concentration) using the LIF technique.

When working with a large geometry, some parameters cannot be controlled easily.

The position of the jets is at the center of the test section. So, we fixed the cameras at the nearest point near the wall of the test section to capture as possible the intensity of fluorescence and view the two jets at the same time. This does not allow us to have a perfect full and net optical access because a compromise is done between the aperture and the focusing of the camera. However, calculations should be done to know in which characteristic regime the experiments are done (as stated in section 2.2.1). The illuminated surface can be estimated starting from the laser thickness (1 mm) and the height perpendicular to the illumination (50 mm) at the level of the test section. The laser power is about 20 MW . This gives a power density of about 4 $\frac{MW}{cm^2}$. From this calculation, the work is estimated to be between the partially saturated regime and the saturated laser regime.

The arrangement of all the materials required for the optical measurements on our facility was done with a lot of attention concerning safety and protection part. So the test section along with the optical materials were covered with safety curtains. By this protection against laser light and also that against sunlight during mornings is consistent.

Another complexities are those regarding the practical part of the experiments. For instance, the solution takes long time to be heated because of its huge volume and then we are obliged to make experiments as fast as possible to maintain the same conditions. In many times, we had to reheat the solution again to get back to the initial conditions.

Other problems were related to the mechanical and electrical part of the set up. For example, we had to design a stand for the calibration facility to fit in the test section. Sometimes, the software bugged and a camera needed repair.

Another difficulty encountered during the experiments is the presence of bubbles upon injection as shown in figure 81. These bubbles were created inside the pumps owing to the pumping technology (impeller pump). The bubbles reflect the laser light and induce too much noise on the recorded images. This problem was solved by using an adequate filter and injecting by gravity force.

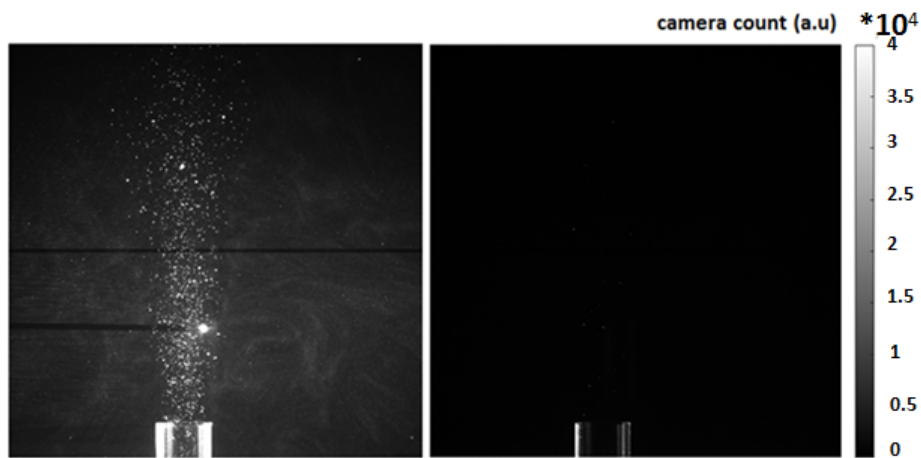


Figure 81: Image on the left without a filter, image on the right with a filter

The setup of the cameras is presented in figure 82. In our measurements, the two 12 bit cameras of resolution 2048*2048 are used for the two color LIF technique. For the first camera, a high pass band filter is used at 550 *nm* to capture the fluorescence response of RhWT. Concerning the second camera, a notch filter (transmission band pass between 400 to 517 *nm* and 548 to 710 *nm*) is used to capture a sufficient fluorescence response of FL27 and avoid collecting laser light.

For the PIV measurements, the 12 bit camera of resolution 3320*2496 is installed and a 532 *nm* filter is used to only get the particles. The frequency was set to 1 Hz so that we can adapt the cameras with the synchronizer and the software. Regarding the mirrors placed, first a dichroic mirror (DM) at 550 *nm* was placed in a rectangular cage in front of the two LIF cameras and another 50% semi-reflective mirror was placed in another rectangular cage in front of the second LIF and PIV cameras as shown in figure 82. Each camera was geared with a 50 *mm* lens.

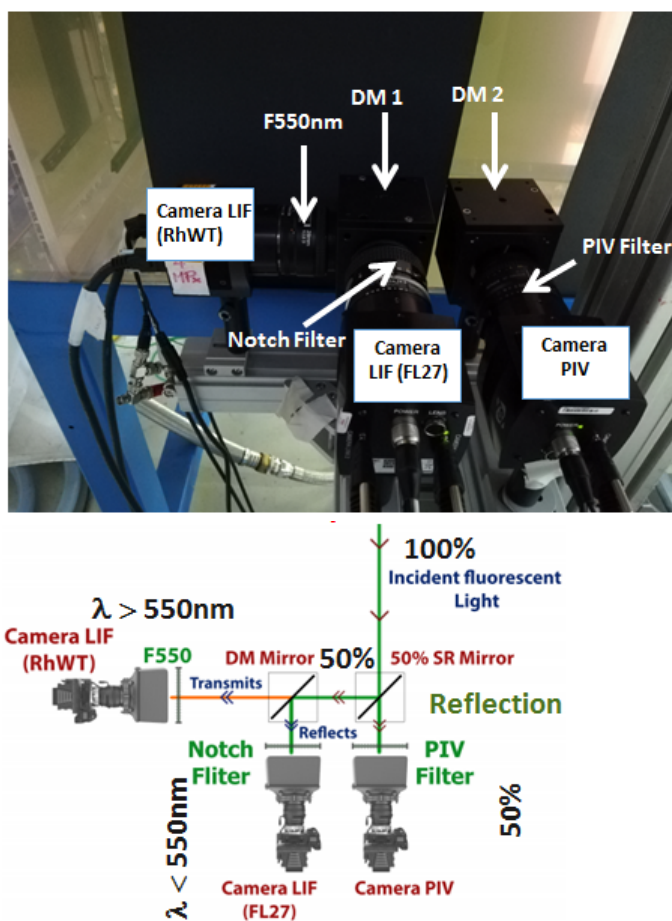


Figure 82: The setup of cameras and optics

Thus, first 50 % of the light is reflected to the PIV camera and the other 50 % to the LIF cameras. This reflected beam is forwarded towards the dichroic mirror. It reflects the wavelength lower than 550 nm into the second LIF camera to collect the response of FL27. Then, it transmits fluorescence which has a longer wavelength than 550 nm into the first LIF camera to collect the response of RhWT. It is important to state that the diameter of the notch filter is 25 mm which does not match that of the camera's objective (50 mm). Thus, a lens hood mounting mark was used to fit the notch filter on the camera. So this procedure along with the mirrors configuration has its drawback in obtaining a reduced optical view field as shown in figure 83 and also obtaining an inverse image for the first camera.

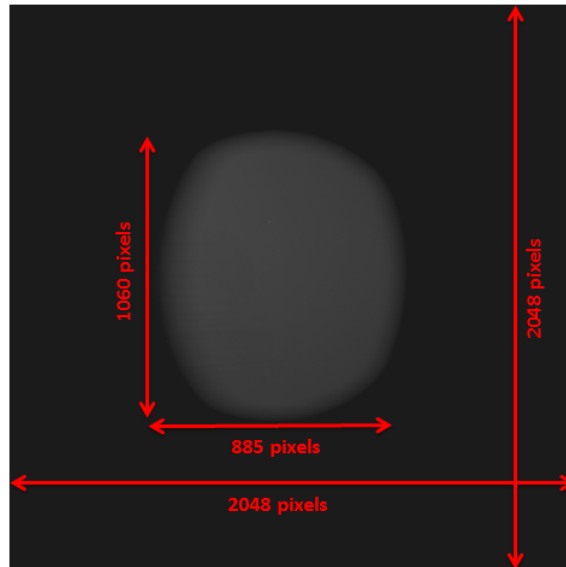


Figure 83: Example of the reduced optical field of view for the second LIF camera

From the setup of figure 82, figure 84 shows the emission and absorption spectra of dyes (FL27 and RhWT) chosen for the measurements with an illustration of the spectral bands selected for the application of the 2c/2d LIF method.

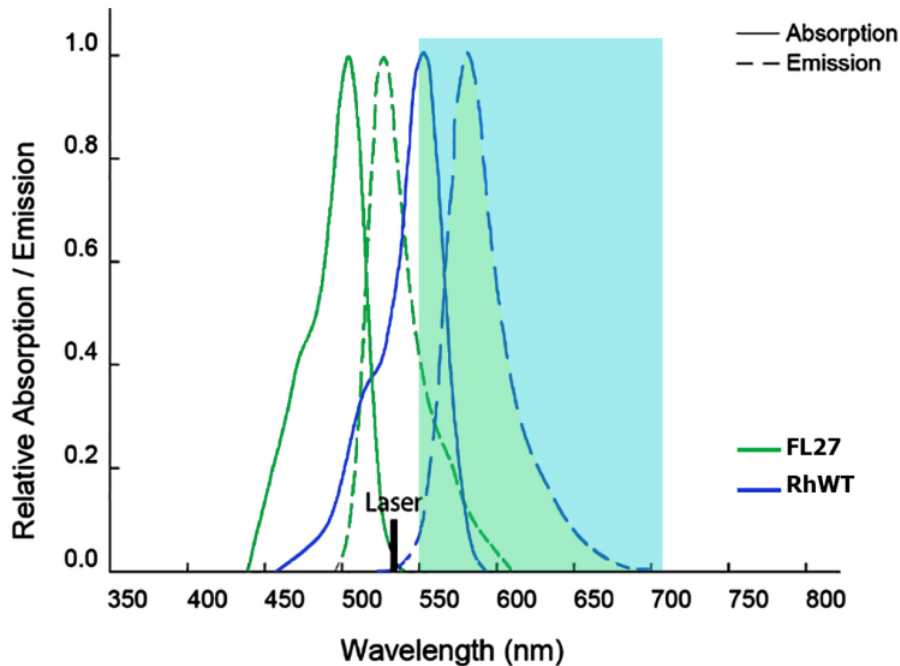


Figure 84: Emission and absorption spectra of dyes (FL27 and RhWT)

7.2 Experiments and processing of the results

7.2.1 The experimental protocol

The experimental protocol considered for all the experiments is explained in this section. First, the storage tank is filled with de-ionized water. A concentrated solution of the fluorescent dyes in addition to the particles are added in the storage tank. The pump in this tank is turned on until the solution is well mixed. During this time, the measurement setup (cameras, laser, synchronizer and software) are turned on. The mixed solution is then sent to the cold and hot tanks. The first step in measurement is capturing the dark images for each camera. The dark response of the camera is quantified when the lens cap is covered. Several images are captured, then the average of intensity is calculated for each camera. This average is the dark response. Then, reference images are captured. They are taken before starting the variation of the parameters. The conditions are stable at uniform temperature and without any injection. Several images are captured and their average is calculated. The next step is the spatial calibration for the images of the three cameras since they do not show the same visual field. This step is explained in details in section 7.2.3.

Then, the parameters are varied and measurements are done.

7.2.2 The experimental matrix

Table 14 lists the performed tests according to the planned experimental matrix. The water is seeded with the PIV particles and the two fluorescent dyes FL27 and RhWT. The parameters of the matrix are the injection flow rate and the injection temperature of each jet realized in a medium in which the temperature was varied too. So three parameters were controlled during these measurements. Experiments 1, 3 and 6 are carried out with a single jet. Only in experiments 1 and 2, LIF and PIV were simultaneously applied.

Exp.	Temperature in test section (°C)	Temperature in jets(°C)		Flow rate (m ³ /s)		Reynolds		Discharge Froude		Richardson		LIF	LIF and PIV
		T1	T2	Q1	Q2	Re1	Re2	Fr1	Fr2	Ri1	Ri2		
1	52	27	No injection	0.2	No injection	3930	No injection	-24.5	No injection	-0.04	No injection		
2	45	27	27	0.27	0.27	5400	5400	-62.2	-62.2	-0.016	-0.016		
3	50	28	No injection	0.1	No injection	2000	No injection	-6.72	No injection	-0.15	No injection		
4	50	28	56	0.1	1.23	2000	40000	-6.72	2071	-0.15	0.0005		
5	47	28	28	0.11	0.11	2222	2222	-9.41	-9.41	-0.1	-0.1		
6	42	28	No injection	1.3	No injection	25555	No injection	-1785	No injection	-0.0006	No injection		

Table 14: The experimental matrix of velocity and temperature measurements

7.2.3 Treatment of the LIF and PIV results

The LIF and PIV images are treated separately in these experiments. Starting with the LIF technique, the treatment consists of three processes: pre-processing, processing and post processing. This corrects errors such as camera dark response, spatial calibration between the two cameras, deblurring and temperature calibration. The processing procedure is shown in figure 85 and its steps are explained later.

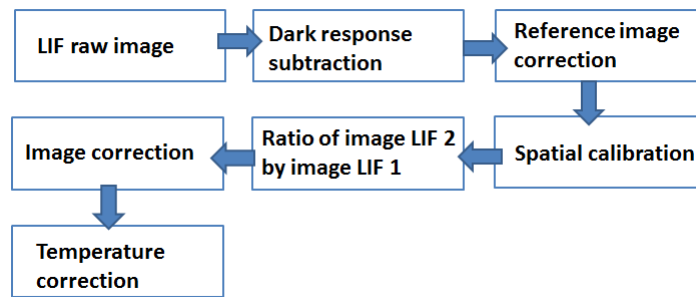


Figure 85: The processing procedure

In a first step, the average of the dark response of each camera is subtracted from the raw images. Then, the average of the reference image is subtracted from the previous images. This step eliminates background effect and smooths the intensity distribution. Figure 86 shows the average reference image of each fluorescent dye captured by the LIF cameras.

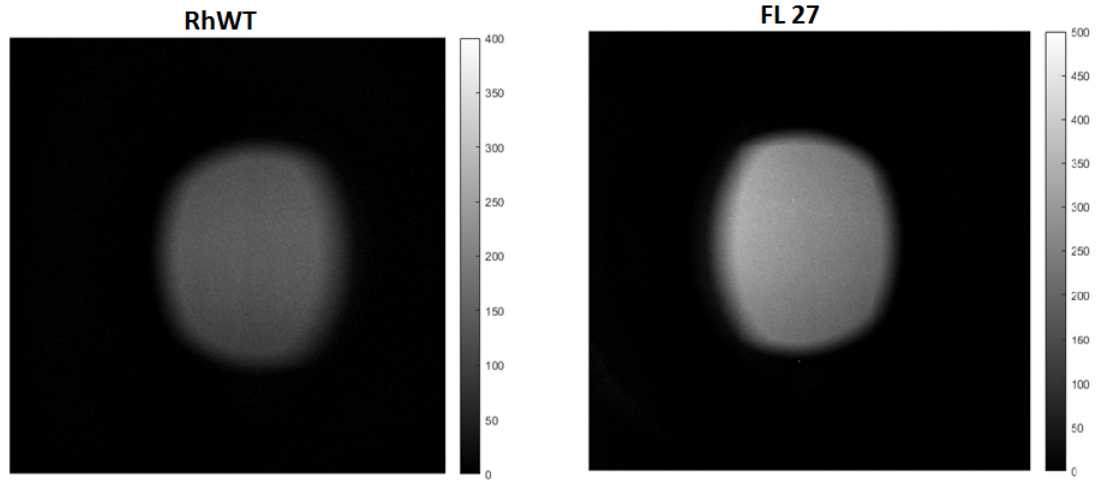


Figure 86: Average reference images captured at 50°C

The next step is the application of a spatial calibration for the images of the three cameras. Generally, the calibration consists in placing a target with highly contrasted markers (for example white dots on a dark background as shown in the figure 87) with a known physical position as the cross shown or even by identifying several points.



Figure 87: The calibration facility

The target is placed possibly in the same location of the laser sheet, and translated to sweep a volume in which the illuminated region is enclosed. One of the markers is identified as the origin of the physical reference system, while the other points coordinates are determined by setting the orientation of the axes. The final result is a discrete correspondence between spatial coordinate and image coordinates. Concerning the LIF images obtained by the two cameras, many points that match in the two images are chosen. The polyfit function

using Matlab creates the correspondence (translation and rotation) of the first camera to the second as shown in figures 88.

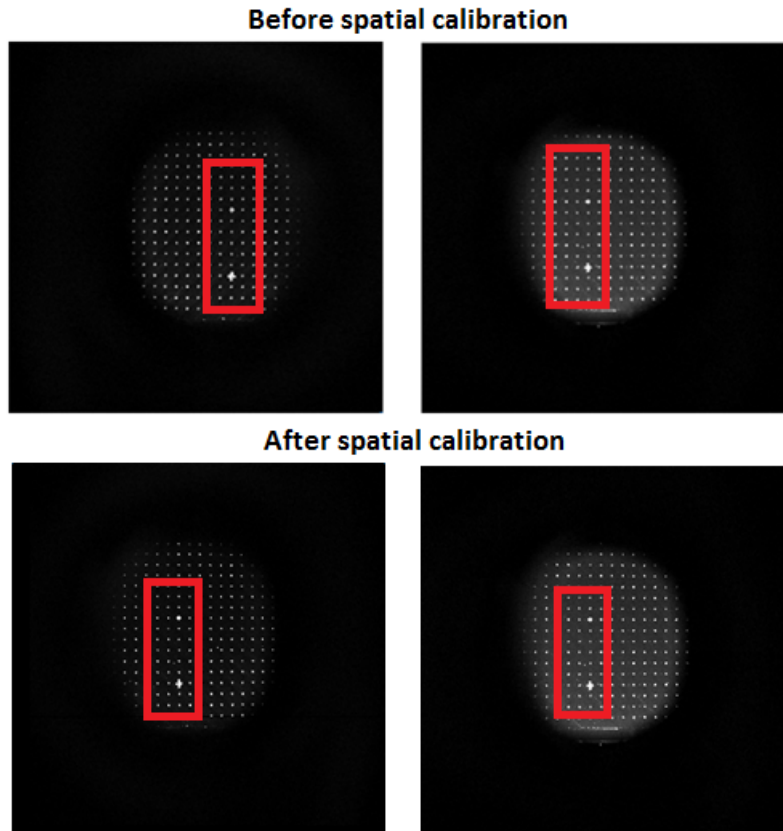


Figure 88: Before and after calibration (to the left: first camera; to the right: second camera)

On the other hand, the blurring of an image can be caused by many factors such as the movement of the cameras during the experiments, index of refraction,... In our experiments, all the cameras were well fixed as possible so there was no movement during the image capture process. However, the variation in temperature changes the index of refraction which then creates blurred images. For instance, the density of a liquid usually decreases with temperature, then the speed of light in a liquid will normally increase as the temperature increases. Thus, the index of refraction decreases as the temperature increases for a liquid.

The fundamental task of deblurring is to deconvolve the blurred image that exactly describes the distortion. In our case, we used functions in Matlab such as “imadjust” and “medfilt” to sharpen the images after increasing the contrast in them. The first function adjusts the image intensity values to increase the contrast of the output image. The second one is a 2-D median filtering function where it is performed in two dimensions. Each output pixel contains the median value in a 3-by-3 neighborhood around the corresponding pixel in the input image. Some use a convolution function, but the goal was to reduce the noise effect of the blurring. In such a case, a median filter is more effective. In the last step of processing, we need to convert the values of intensity into temperature values. Although we did the calibration testings on a small volume (30 L), we repeated these tests on the large volume of TABOULE (1000 L).

So for these experiments, we studied the response of the solutions at different temperatures. This step is very time consuming because we needed to heat the solution at a first step to 30°C, capture images, then send the solution to the hot tank to reheat again until 35°C, send it back to the test section to capture the images and repeat the operation. Figure 89 shows the results of calibration for each dye: FL27 and RhWT. We notice that the slope of the response of FL27 in this case (6.8) is lower than that obtained in chapter 4 (14.9 at t_0 and 11.5 at t_0+2 days). This can be due to a scale effect related to the volume of the test section. Another reason might be the presence of the other dye RhWT which can decrease the response of FL27. For the calibration calculations, the same protocol of chapter 4 is applied. 100 images are captured and the average image is calculated.

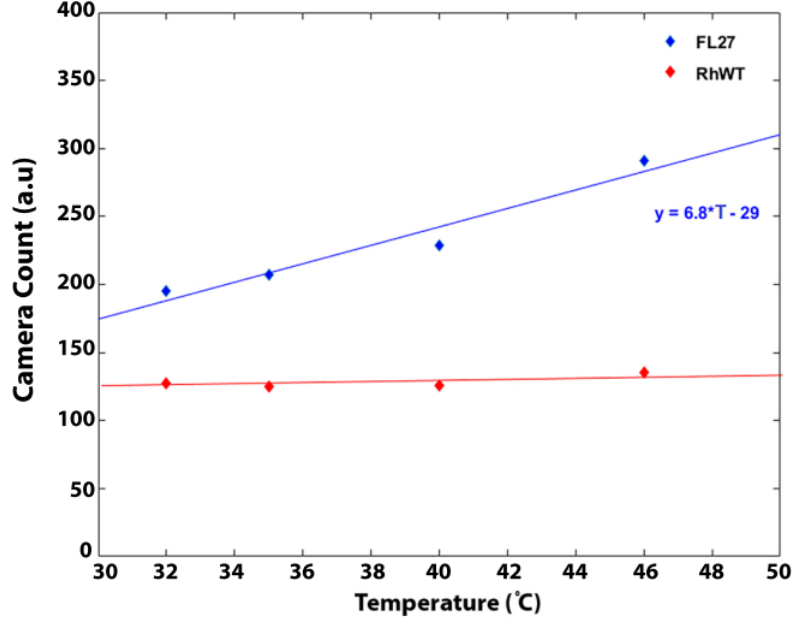


Figure 89: The results of calibration for each dye

Since we are implementing the ratiometric technique between FL27 and RhWT, the equation below presents the processing done to

$$Ratio = \frac{Exp_{FL27} - Ref_{FL27}}{Exp_{RhWT}^* - Ref_{RhWT}^*} \quad (40)$$

where:

Exp_{FL27} is the image obtained during the experiment using the second camera

Exp_{RhWT} is the image obtained during the experiment using the first camera

Ref_{FL27} is the reference image obtained using the second camera (no injection)

Ref_{RhWT} is the reference image obtained using the first camera (no injection)

The * refers to the calibration matching of camera 1 to camera 2.

The equation $T = 53.9 - 77I$ presents the relation between temperature T and the camera count I we got after applying equation (39) on the values of calibration of each dye.

For the images obtained by PIV, the processing is done using the PIV analysis software (TSI Insight 4G) and the velocity vectors are retrieved using Scilab. In the processing step, the grid engine chosen is rectangular, it breaks the input images up into smaller spots and copies the pixels from the input images into the spots and passes the spots to the Gaussian mask. With this mask, each pixel in the spot is multiplied by a Gaussian weighing function so that the spot is bright in the center and dark around the edges. This weighting gives more value to the center pixels and less to the edge pixels. Then, using the fast Fourier transform, the correlation function is computed and returned as a correlation map. A two-step processing is applied; 128*128 pixels interrogation window and 50 % overlap for the first step, and then 64 by 64 pixels interrogation window and 50 % overlap for the second step. The sample area of PIV measurement in these experiments is of 182*135 mm^2 . In the next section, we present the experiments done along with the results and their analysis.

7.3 Experimental Results and analysis

During the process, 100 images were captured by the three cameras simultaneously at a frequency of 1 Hz. Generally, the analysis are lead using the average (over time and space) for the temperature and the velocity. This smooths the results and gives a physical interpretation of the change in temperature and velocity. The quality of the LIF image is not high and this is due to a major problem faced with this technique in most of the thermal studies of jets. The problem is the appearance of striations due to the change in the refractive index resulting from the temperature variation of the jet in the surrounding. These striations are random, either of enhanced or decreased intensity and they mainly lead to non physical temperature values. In order to know in which characteristic regime the experiments are done, the laser excitation intensity I_0 is about $(\frac{W}{m^2})$ and the saturation intensity of the fluorescent dye I_{sat} $(\frac{W}{m^2})$

7.3.1 PIV and LIF on a negative buoyant jet at $Re= 3930$ and $Fr_d=-24.5$

A single fluid flow is injected from the nozzle at temperature 27°C into the test section having a temperature 52°C at a flow rate of $0.2\text{ m}^3/hr$. This gives a Reynolds value of 3930 and a negative discharge Froude number of 24.5. The average velocity and temperature fields over time obtained by LIF and PIV are shown in the figure 90.

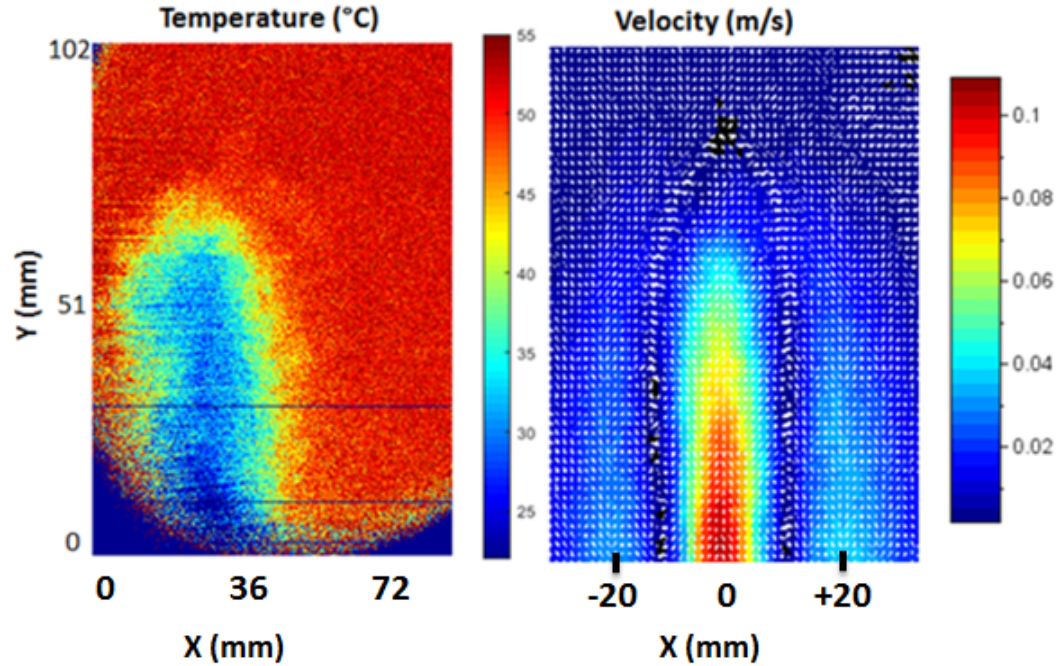


Figure 90: The LIF and PIV time average field profiles

Several figures are presented in the following to analyze the variation of velocity and temperature during the spread of the jet. For the analysis of the velocity field, the time average velocities along the centerline and the axial direction are plotted. For the analysis of the temperature field, the space moving average over 5 points of the temperature along the centerline of the nozzle is plotted. The operating conditions in this experiment are approximately identical to those of 6.4.1. From figure 72, the established flow is after 20 s. That is why we proceed our analysis after this time to compute the time average field profiles.

Figure 91 shows the plot of the time average velocity at different positions indicated by the red lines. The positions were chosen to cover the outlet of the nozzle (position Y_A), the maximum height of jet penetration (position Y_D) and two positions in between them (position Y_B and Y_C) because we see a change in the color map. We notice that the time average velocity of the fountain had a symmetric Gaussian profile with three peaks. The highest value for the peak at the center is upon injection (position Y_A). As the jet spreads in the upward direction, the peak at the center decreases since the velocity is decreasing. The maximum velocity reached during the spread is about 0.11 m/s which is less than the value of the injection velocity calculated which is 0.176 m/s . This is

because we are not capturing exactly the flow at the outlet of the nozzle because of the reduction of the optical view due to the difference of resolution of the three cameras.

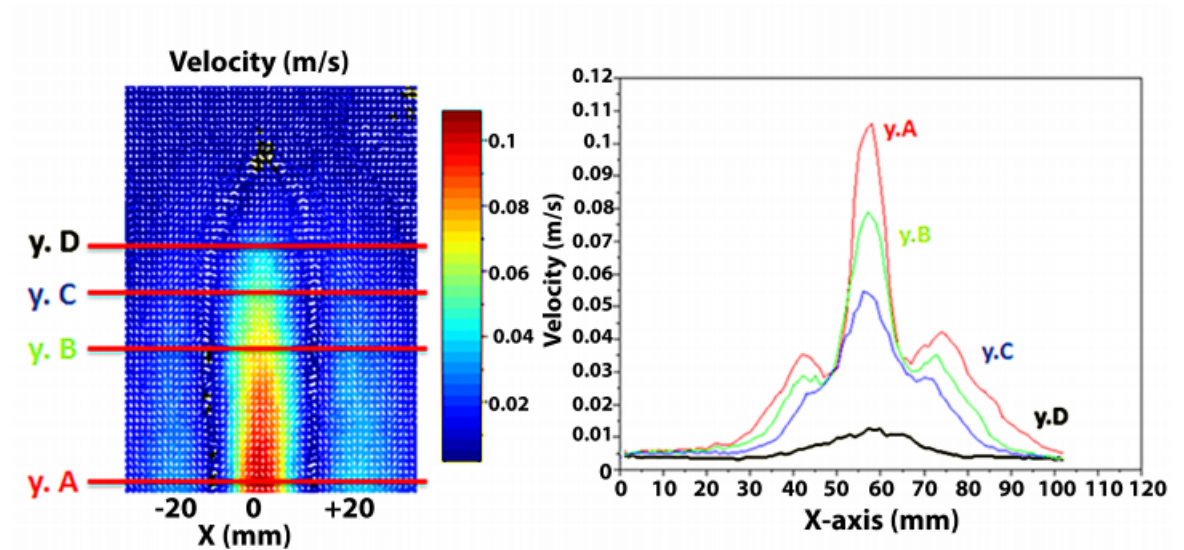


Figure 91: The plot of the time average velocity along different positions

Figure 92 shows the plots of the axial velocity and its vertical component along the position Y_B . We see that the fountain spreads upward at the center of the nozzle since the velocity is positive until it reaches its maximum height. Then, it spreads downward in the two adjacent peaks where the velocity becomes negative (red curve).

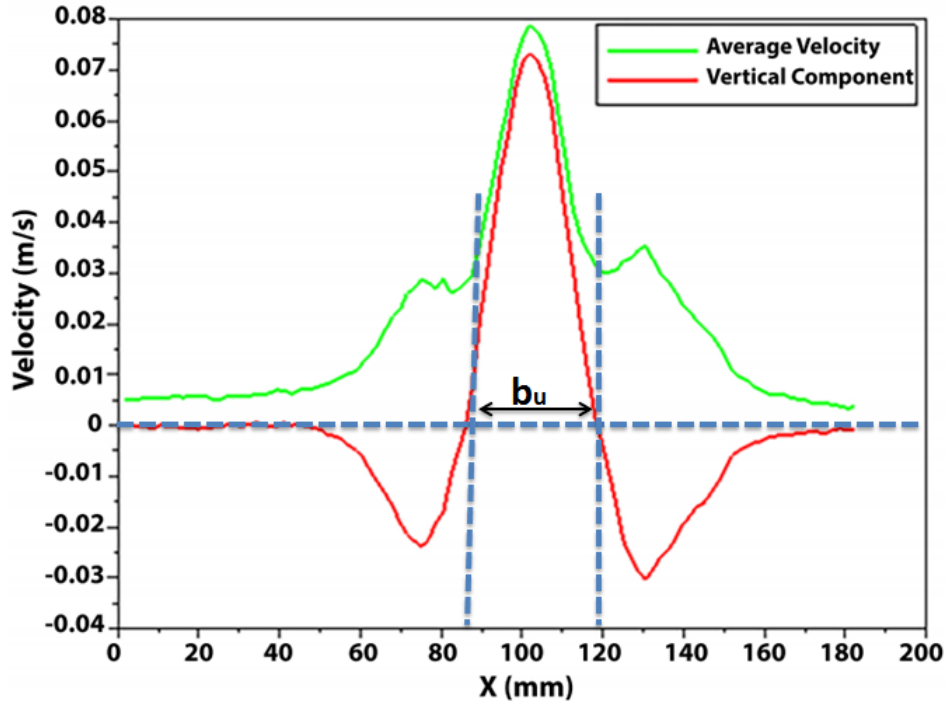


Figure 92: The plot of the average velocity and its vertical component at position Y_B

From the different positions present in figure 92, we exploited the values of the jet width as shown by the dashed lines in figure 93. The goal was to plot the variation of the jet width (b_u) as function of the height of penetration (h) similarly to the study done by Mizushima et al. [76]. They showed that the jet width is linear dependent with the elevation. They found a constant of 0.17 for this linearity from equation (22). In our experiment, we had a constant of 0.38.

h (mm)	b_u (mm)
5	50
45	30
56	25
65	20

Table 15: Experimental values of jet width with height of penetration

The plot of the space moving average of temperature and the centerline velocity are shown in figure 93. The flow which is injected at temperature 27°C into the test section maintains approximately a range of temperature between 27°C and 32°C along the y-axis from 0 and 51 mm ; then the temperature starts to increase gradually until it reaches a value about 50 to 51°C at its highest level of penetration (around 80 mm). This value of temperature is approximately near to that found by the thermocouple in the test section which is 52°C . The centerline velocity decays uniformly as the negative buoyant jet evolves in the upward direction. We notice that between 0 and 51 mm , the temperature variation is steady when compared to that of velocity which decreases rapidly due to the competition between momentum and buoyancy flux. This is also shown by the rapid color change in the time average velocity field profile presented in figure 90.

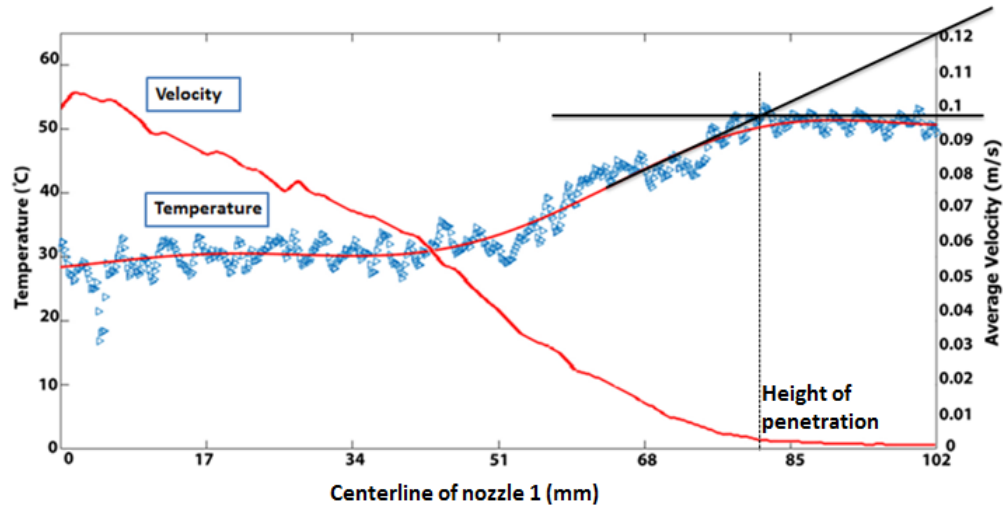


Figure 93: The space moving average of temperature and the centerline velocity

To end up this section, figure 94 shows an instantaneous image obtained at $\text{time} = 30\text{ s}$ from the start of experiment. This result highlights high noise which induces a limited accuracy in measurements. However, we can recognize some swirls resulting from the mixing between the high and low temperature fluid.

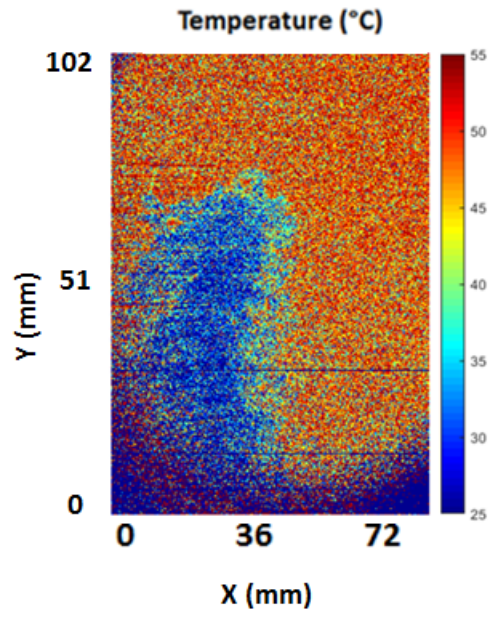


Figure 94: The space moving average of temperature and the centerline velocity

7.3.2 PIV and LIF on two negative buoyant jets at $Re= 5400$ and $Fr_d= -62.2$

Two fluid flows are injected at temperature 27°C into the test section having a temperature 45°C at a flow rate of $0.27\text{m}^3/\text{hr}$. This gives a Reynolds value of 5400 and a negative discharge Froude number of 62.2. The time average velocity and temperature field profiles obtained by LIF and PIV are shown in the figure 95.

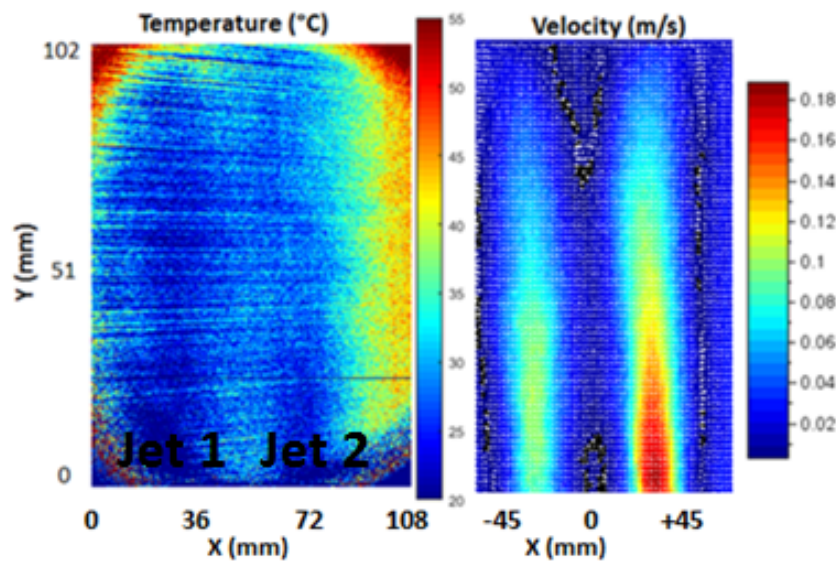


Figure 95: LIF and PIV time average field profiles

Figure 96 shows the plot of the time average velocity at different positions as indicated. We notice two Gaussian profiles referring to the spread of the two negative buoyant jets. However we notice that the two peaks are not at the same level although these two jets have the same conditions at departure. Many factors can lead to this result; maybe more PIV particles were present in the tank providing water to jet 2. The solution of water and particles was prepared for each tank so a difference in concentration of particles may occur. The laser path is from right to left. The temperature difference between the fluid flow and its surrounding induces a change in the index of refraction which then modifies the laser sheet. That is why we see this difference in the measurements between the two fluid flows.

The injection flow rate is $0.27 \text{ m}^3/\text{hr}$ which gives a velocity of 0.24 m/s ; a value higher than the maximum velocity found (0.19 m/s) and this is because of the capturing position as discussed previously.

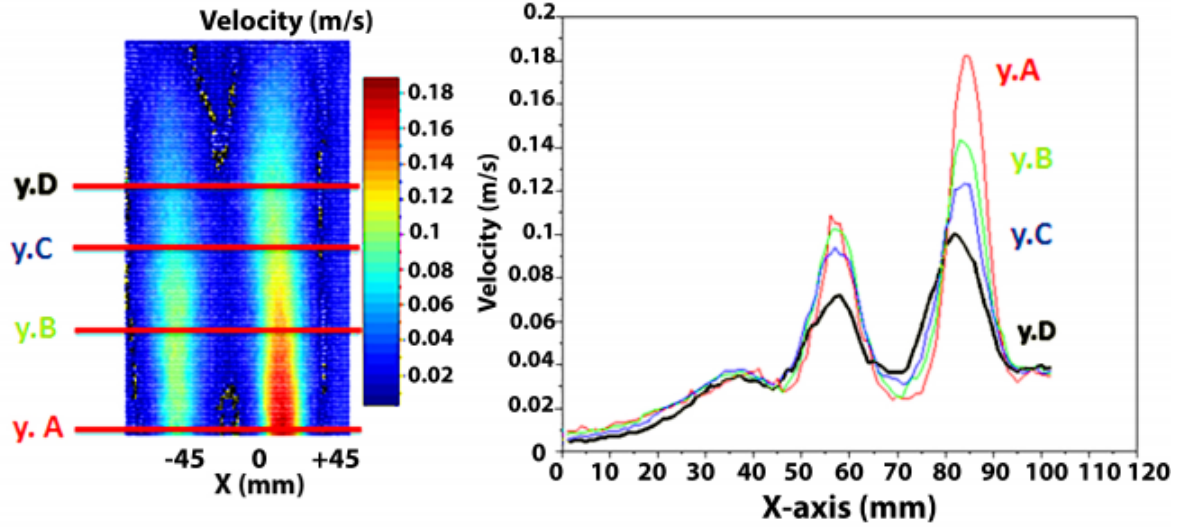


Figure 96: The plot of the average velocity along different positions

Figure 97 shows the plots of the average time temperature profile along the centerline of the nozzle 1 and 2. Although the injection of the two jets was done at the same temperature (27°C), the values of the temperature variation are not the same. We notice the response of jet 2 is higher than that of 1 by 10°C . This resembles the results we got by PIV regarding the difference in the peaks. So, the fluorescence response at the right is higher than the left part due to the modification of the laser sheet. In conclusion, it is difficult to measure temperature and velocity in the presence of many jets where the temperature is different from that of the surrounding.

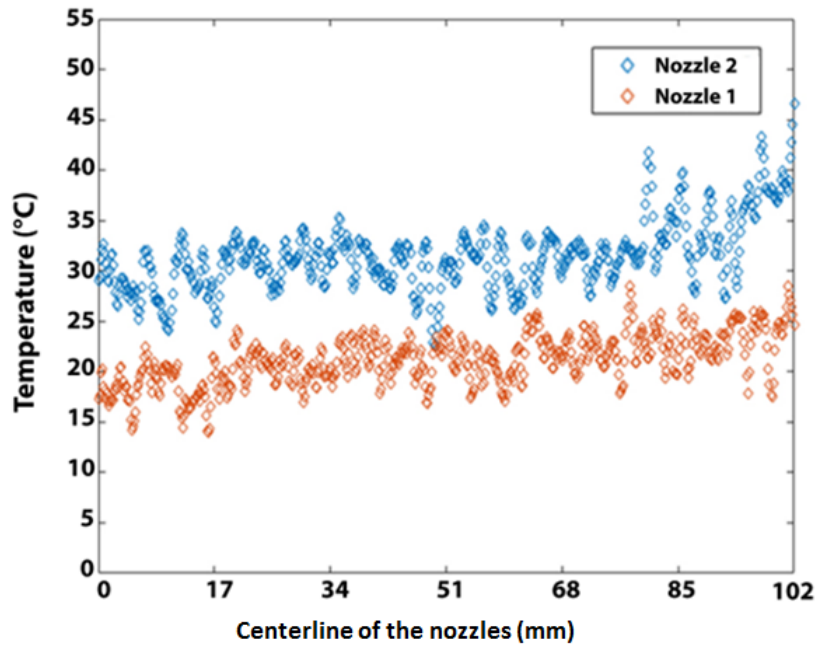


Figure 97: The average time temperature profile along the centerline of the nozzle 1 and 2

7.3.3 LIF on a negative buoyant jet at $Re= 2000$ and $Fr_d= -6.72$

A single fluid flow is injected from the nozzle at temperature 28°C into the test section having a temperature 50°C at a flow rate of $0.1\text{ m}^3/\text{hr}$. This gives a Reynolds value of 2000 and a negative discharge Froude number of 6.72. In this experiment, we present only the time average temperature profile obtained by the LIF technique (figure 98). PIV technique was applied but the results were not relevant because of some complexities faced during this experiment.

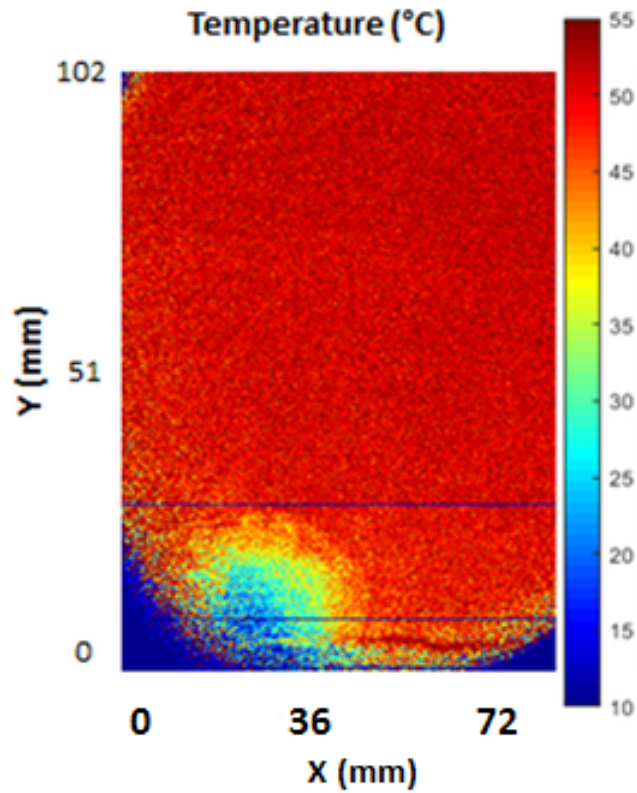


Figure 98: The average time LIF image on a negative buoyant jet at $Re= 2000$ and $Fr_d= -6.72$

The plot of the space moving average of temperature in this experiment is shown in figure 99. The temperature increases directly until it reaches a value ranging between 48 to 52°C at its highest level of penetration (around 20 mm).

The variation of temperature is always along the height of penetration. It is interesting to compare this experiment with that of 7.3.1 since both study the spread of a single negative buoyant jet but at different flow rates. We notice that the spread of the fountain in this case is lower than that of experiment 7.3.1 due to the lower flow rate. The low value of flow rate attributes to a lower momentum flux, thus a less spreading in the medium.

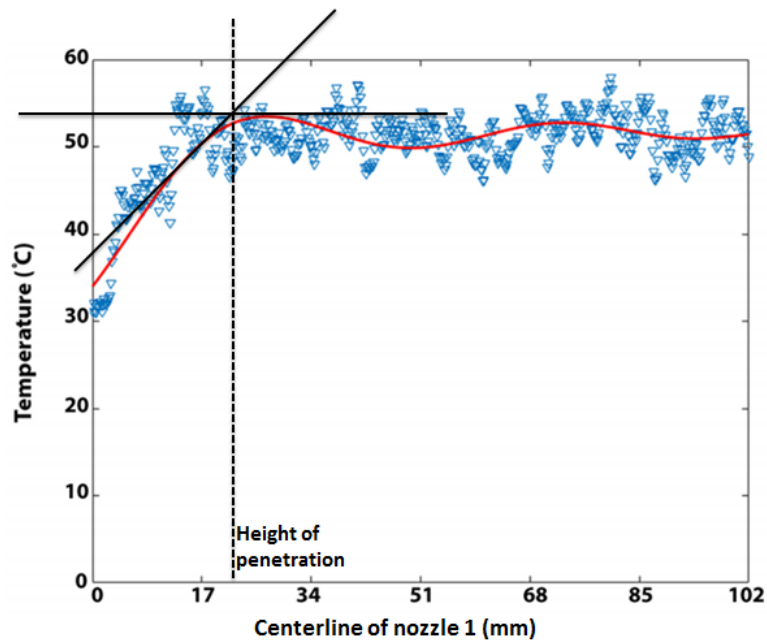


Figure 99: The space moving average of temperature along the centerline of the nozzle 1

**7.3.4 LIF on a negative and a neutral buoyant jets at $Re_1 = 2000$,
 $Fr_{d1} = -6.72$ and $Re_2 = 40000$, $Fr_{d2} = 2071$**

In this experiment, two fluid flows are injected into the test section having a temperature 50°C . The first injection is done at a temperature of 28°C with a flow rate $0.1\text{ m}^3/\text{hr}$ which gives values of 2000 for Reynolds and negative -6.72 for Froude number. The second injection is done at a temperature of 56°C with a flow rate $1.23\text{ m}^3/\text{hr}$ which gives values of 40000 for Reynolds and a positive 2071 for discharge Froude number. The average temperature profile obtained by LIF is shown in figure 100.

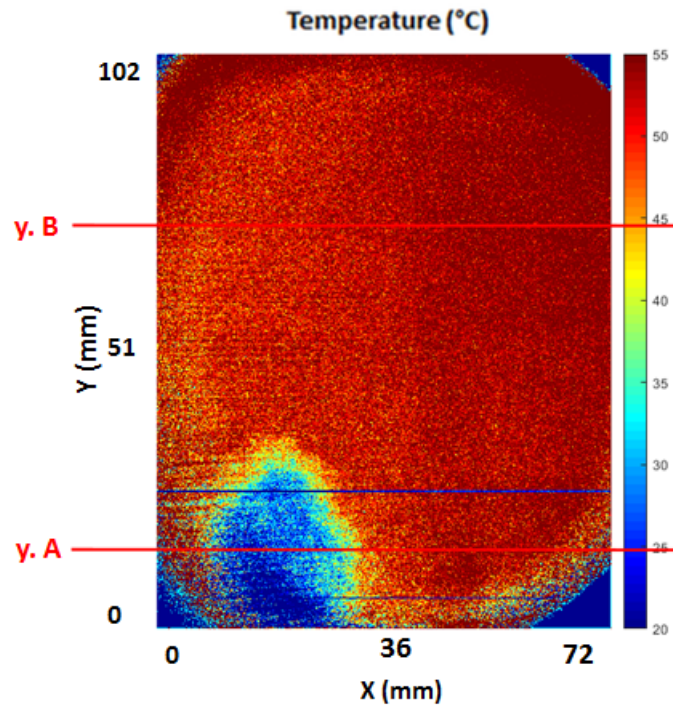


Figure 100: The time average LIF image on a negative and a neutral buoyant jets at $Re_1 = 2000$, $Fr_{d1} = -6.72$ and $Re_2 = 40000$, $Fr_{d2} = 2071$

The space moving average of temperature profile along the centerline of the nozzle 1 and nozzle 2 are plotted in figures 101 and 102 respectively.

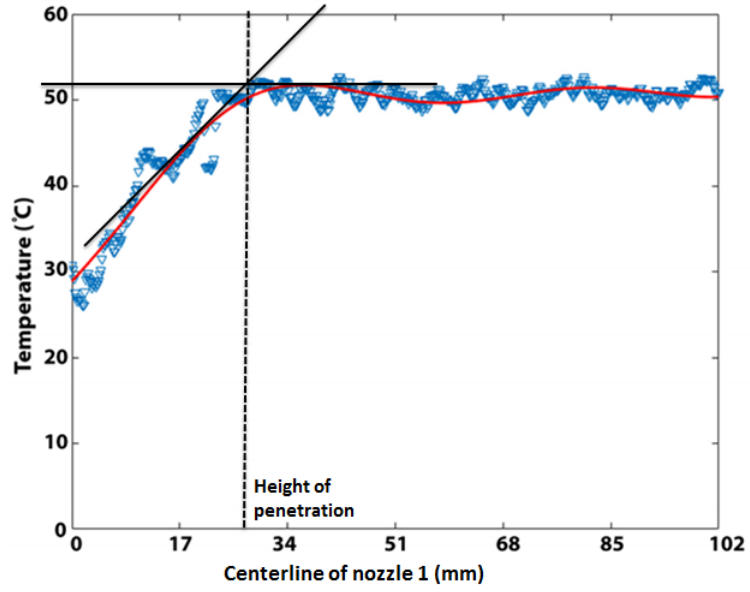


Figure 101: The space moving average of temperature along the centerline of nozzle 1

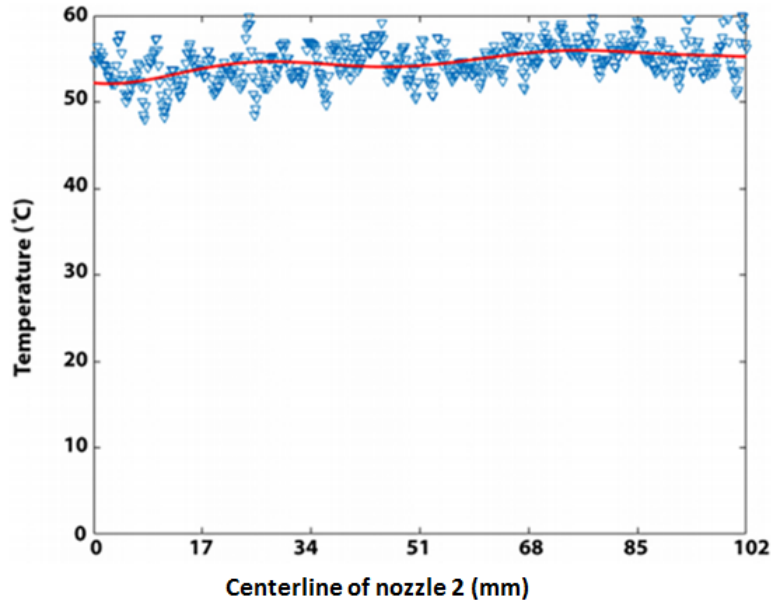


Figure 102: The space moving average of temperature along the centerline of nozzle 2

We notice the profile of the negative buoyant jet (figure 102) is similar to that of experiment 7.3.3 (figure 99) since both cases have approximately the same conditions of injection. However, the highest level of penetration in this case is around 27 mm , a little higher than that of experiment 7.3.3. This can be due to the effect of the second hot jet which can increase its spread along the upward direction. Regarding the profile of the neutral buoyant jet, it maintains a temperature range between 50 and 55°C . The Reynolds and discharge Froude number for this jet are high, so this flow is dominated by inertial forces. This explains why the neutral buoyant jet does not end up as a plume as shown in figures 101 and 102. Figures 103 and 104 show the plots of temperature profiles along the different positions Y_A and Y_B as indicated in figure 101.

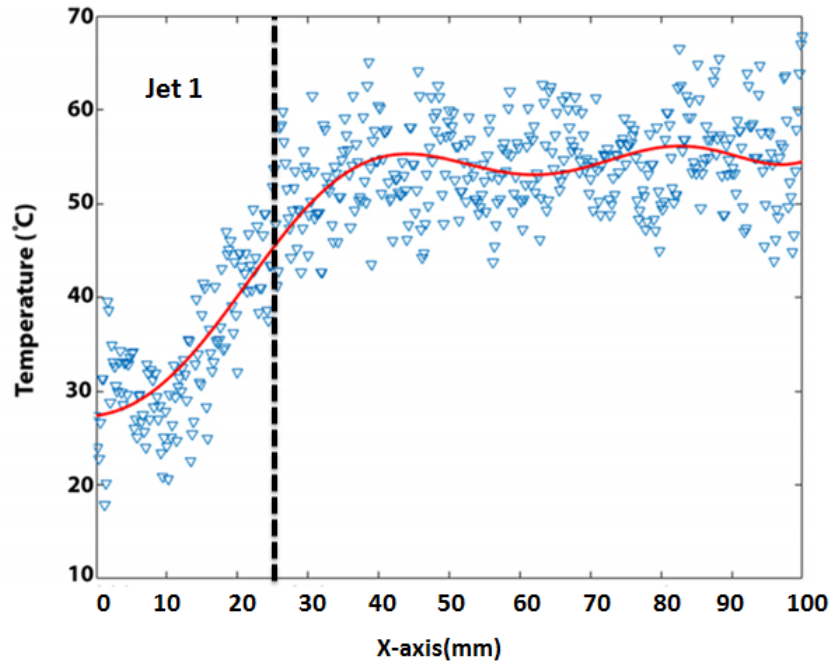


Figure 103: Plot of temperature profiles along the different positions Y_A

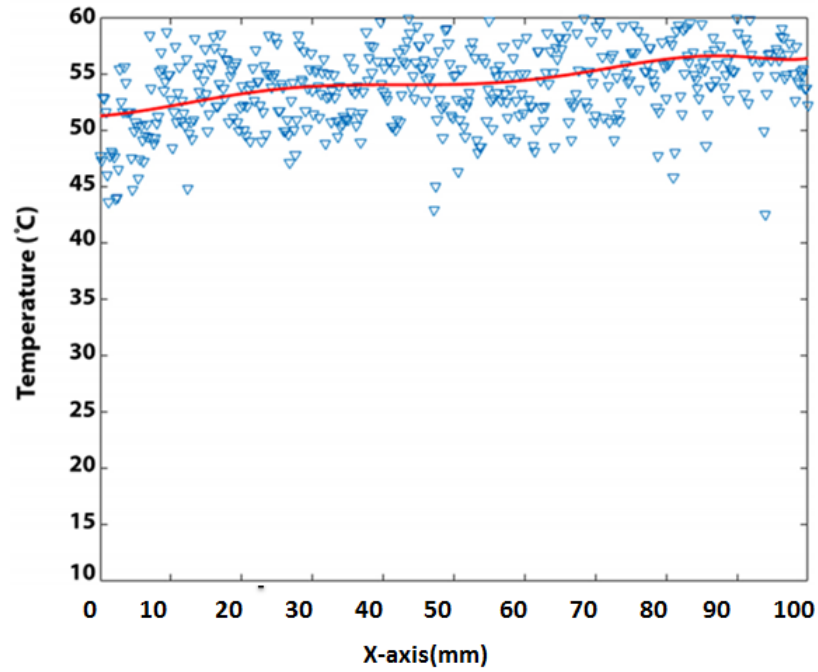


Figure 104: Plot of temperature profiles along the different positions Y_B

From the plot along Y_A shown in figure 104, we can see the flow of the two jets. However along Y_B , the jets are mixed. As seen, the values are biased so we cannot define exactly the width of each jet from the temperature plot.

7.3.5 LIF on two negative buoyant jets at $Re= 2222$ and $Fr_d= -9.41$

Two fluid flows are injected into the test section having a temperature 47°C . Both injections are done at a temperature of 28°C with a flow rate $0.11\text{ m}^3/\text{hr}$ which gives values of 2222 for Reynolds and negative 9.41 for discharge Froude number. The average temperature profile obtained by LIF is shown in figure 105.

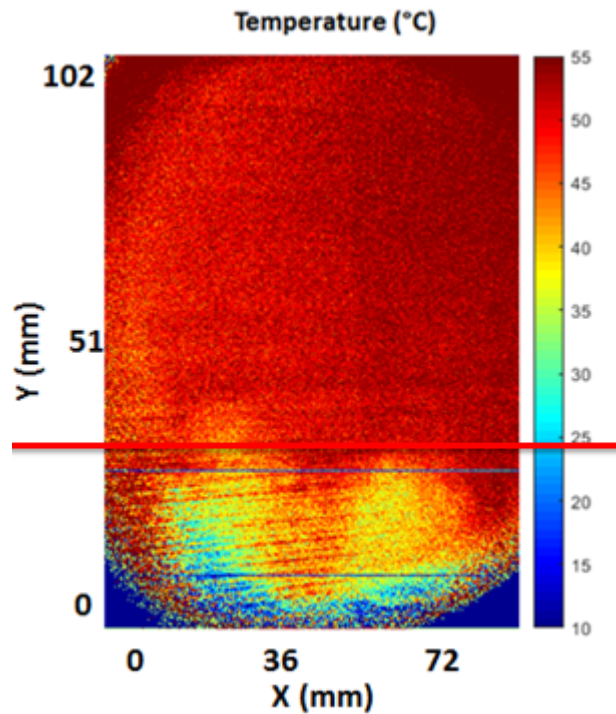


Figure 105: The time average LIF image on two negative buoyant jets at $Re= 2222$ and $Fr_d= -9.41$

The temperature profiles along the centerline of the nozzle 1 and nozzle 2 are plotted in figures 106 and 107.

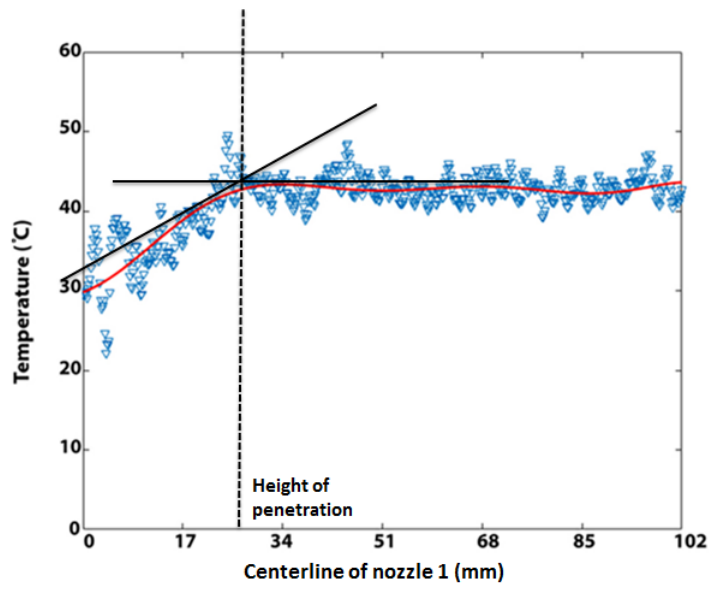


Figure 106: The space moving temperature profile along the centerline nozzle 1

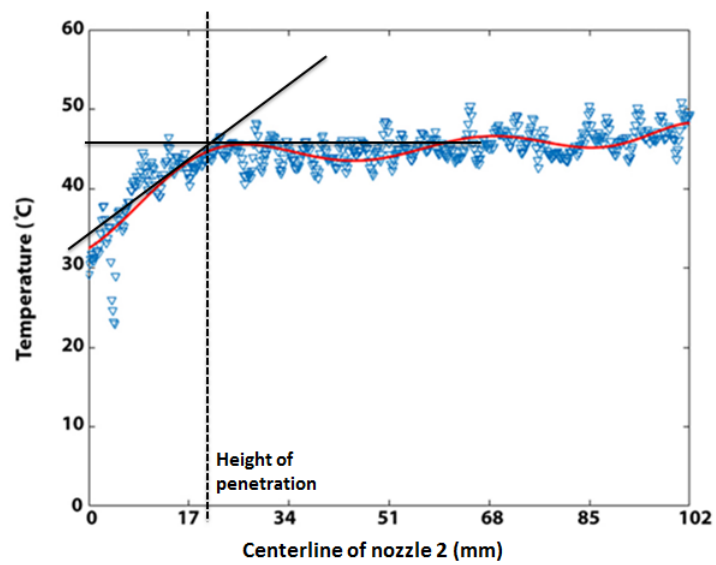


Figure 107: The space moving temperature profile along the centerline nozzle 2

From figures 106 and 107, we notice that the two jets act the same. The temperature increases directly until it reaches a value ranging between 42 to 45°C at the highest level of penetration. The maximum height of penetration of jet 1 is about 25 *mm* and that of jet 2 is about 19 *mm*. In experiment 7.3.3, we had approximately the same parameters as in this case regarding the flow rate and temperatures; however it was the case of a single jet. In comparison, the height of penetration of jet 2 (19 *mm*) is approximately equal to that of 7.3.3 (20 *mm*). It is better to do the comparison of jet 1 in experiment 7.3.3 with jet 2 in this case due to the direction of the laser light that traverses jet 2 before jet 1.

7.3.6 LIF on a buoyant jet at $Re = 25555$ and $Fr_d = -1785$

A single fluid flow is injected from the nozzle at temperature 28°C into the test section having a temperature 42°C at a flow rate of $1.3\text{ m}^3/\text{hr}$. This gives a Reynolds value of 25555 and a negative discharge Froude number of 1785 . The average temperature profile obtained by LIF is shown in figure 108.

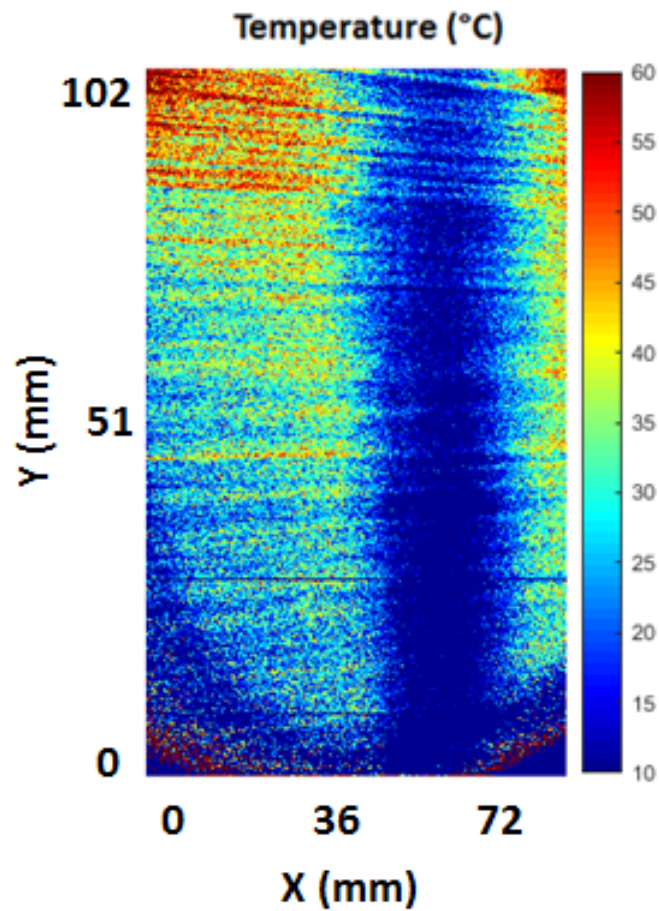


Figure 108: The time average LIF profile on a buoyant jet at $Re = 25555$ and $Fr_d = -1785$

Figure 109 shows the temperature profile along the centerline of the nozzle. We notice that the values vary between 25 to 35°C in a non coherent way

with. The height of penetration in this case is larger than the field of view of the camera. This experiment can be compared with 7.3.1 and 7.3.3.

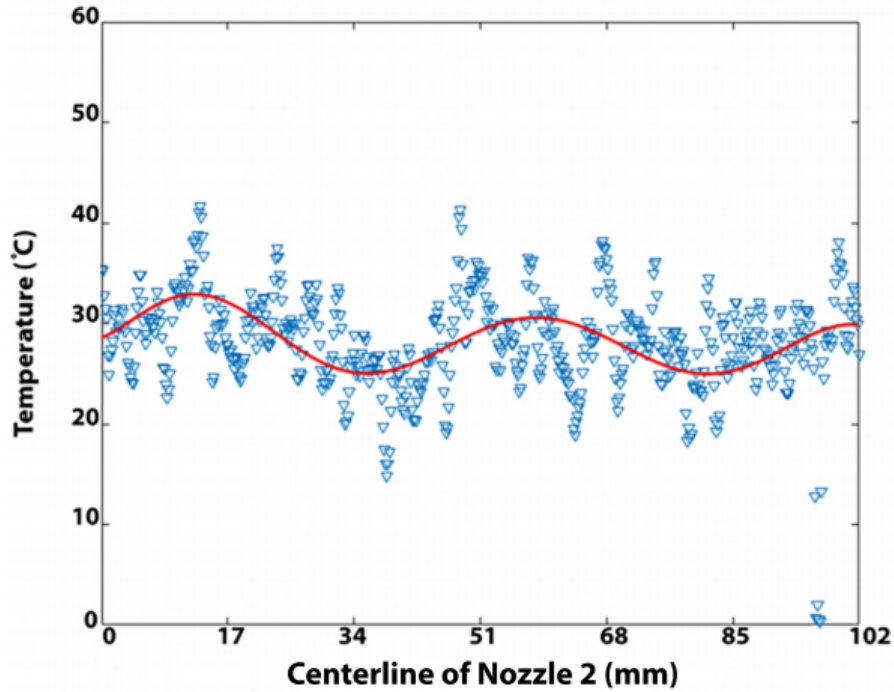


Figure 109: The temperature profile along the centerline of the nozzle 2

This experiment can be compared with experiments 7.3.1 and 7.3.3 since they all study the injection of a single jet. Thus, we compared the results of the height of penetration in these experiments in terms of Reynolds and discharge Froude numbers. These results are presented in table 16 and they are organized in increasing order of the dimensionless numbers Re and $-Fr_d$. These values can be exploited to a graph in similarly to the approach of Mizushima et al. [76]. They plotted their results by presenting the variation of $\frac{h_m}{D}$ as function of $\sqrt{-Fr_d}$ (figure 25) in which they got a constant of 1.66 as was shown in equation (24). Using the values of table 16, we get a constant of 1.25 which is a little lower than the constant of their experiments.

Experiment	Reynolds	Discharge Froude	$h_m(mm)$
3	2000	-6.72	20
1	3930	-24.5	80
6	25555	-1785	very large

Table 16: Summary of the results of experiments 7.3.1, 7.3.3 and 7.3.6

7.4 Conclusion

For the first time, we managed for to simultaneously apply the measurement techniques PIV and LIF on the complex test section TABOULE having a volume 1000 L . We were also able to perform several experiments to study different cases by varying several parameters. However, we faced many complexities that do not allow us to compute the accuracy of our measurements. The degradation over time of fluorescent dyes does not allow to get a stable response over time as function of temperature variation. Thus, the solution should be prepared again for each experiment which gets difficult when working with large facilities. The setup of the cameras and its optics also contribute to the decrease in accuracy because of the reduced field of view. Thus, there is a need for improvements in this approach to increase the accuracy of the results.

Chapter 8

Conclusions and Perspectives

8 Conclusions and Perspectives

This last section is a summary of the work presented in this thesis. It presents the main approaches, the results and ends up with the perspectives.

8.1 Summary and Conclusions

Through this thesis, we sought to put into practice the measurements of temperature fields by means of Laser Induced Fluorescence using two dyes (2c/2d LIF) and apply it simultaneously with PIV on a complex geometry.

The primary objective of the work was to accomplish a thermal hydraulic study of the different phenomenology present in the MICAS mock-up; more precisely the interaction between the hot and cold fluid flows present at its core. This objective was achieved by simultaneously measuring temperature and velocity fields using optical methods. 2c/2d LIF and PIV were chosen respectively for this purpose. However, through a survey in literature, the LIF technique is limited to simple volume geometries (less than 30 Liters). Thus, the experimental matrix was divided into several steps.

In a first step, the LIF technique was applied for the first time in our laboratory on a simple geometry of volume 30 L . We studied the response of five fluorescent dyes Classical fluorescein, FL27, RhWT, Rh6G and Ch-Na. The goal was to find two adequate dyes for the ratiometric technique of LIF (2c/2d). The main advantages of this technique are the correction for laser power fluctuations and dye absorption. Regarding temperature dependent dyes, FL27 and classical fluorescein showed an increase in their response as function of temperature variation. We got a sensitivity coefficient for FL27 of $3.02\%/^{\circ}C$ at a concentration of $10^{-7}mol/L$. We also re-applied the calibration test of the same solution of FL27 but after two days to study its influence of aging. We realized that both show a very good response as function of temperature variation however that of the first experiment is much more stable than the

second. The reason behind this is the photo-degradation of FL27 with time; that is why the experiments should be done directly and the solution of fluorescein should be stirred frequently. For classical fluorescein, the sensitivity coefficient was $3.38\%/^{\circ}C$ at a concentration of $10^{-4}mol/L$. The response of classical fluorescein was null at lower concentrations. This response is due to the composition of classical fluorescein which is pH dependent. However, in our experiments we cannot add chemical solutions that can stabilize the pH since later our experiments are applied on a complex geometry. The results were more interesting when using FL27 as it shows more stability in the values. FL27 was chosen as a temperature dependent dye for the 2c/2d LIF technique. Regarding temperature independent dyes, we studied the response of Ch-Na and two non-toxic rhodamines: RhWT and Rh6G. We got a sensitivity coefficient for Rh6G of $-0.56\%/^{\circ}C$ at a concentration of $10^{-5}mol/L$. However, the response was not stable during the variation of temperature. We notice a decrease in this response after $40^{\circ}C$. Regarding RhWT, the coefficient sensitivity is $-0.50\%/^{\circ}C$ at a concentration of $10^{-6}mol/L$. The response is approximately stable during the variation of temperature even at high values. For Ch-Na, it shows no variation in its fluorescence response as a function of temperature. However the response is very low even at high concentration. We increased the concentration to $10^{-5}mol/L$ until the color of the solution was dark green. The coefficient sensitivity then was $-0.36\%/^{\circ}C$. The most interesting results were those using RhWT. So, for the application of 2c/2d LIF technique in our experiments, the couple of dyes chosen was FL27 and RhWT.

To pass from a simple geometry ($V= 30 L$) to a complex one (MICAS mock-up), a representative intermediate scale mock-up was designed (TABOULE) during the first year of the PhD. It consists of two jets in which it is possible to vary several parameters to study the interaction between different fluid flows. Two experimental campaigns were performed on TABOULE; a hydrodynamic study for different fluid flows and the simultaneous application of

2c/2d LIF and PIV for temperature and velocity measurements.

In the first study, we used a non reactive fluorescent dye RhWT at a very low concentration so that the flow is not affected due to the presence of the dye. The medium of experimentation is unbounded to have the same exit conditions. Four different fluid flows representing those in MICAS were studied and compared with literature. We compared the spread of a single and two negative buoyant jets into a hot medium. The jet penetrates to its maximum height in the surrounding medium, then decreases and finally fluctuates around a mean value of the maximum height of penetration. The results we got were comparable to those found in literature regarding the values of the maximum height of penetration h_m and the width of the fluid flow b_j . In the case of two negative buoyant jets, the maximum height of penetration of the first jet decreased by half when compared to the first experiment due to its interaction with the second jet. Then, we compared two cases; positive and a neutral buoyant jet at low and high Reynolds numbers. Three phases of the spread were identified in the case of a positive buoyant jet. In the region near the nozzle exit, the jet momentum dominates and the flow is similar to a neutral buoyant jet. Far from the jet exit, the buoyancy dominates, and the flow acts like a plume. The intermediate region however is a transition between jet flow and plume flow. However, the second and the third phase of spread depend on the flow rate of injection which directly affects the momentum force of the spread. For instance, if the flow rate is low, then buoyancy force is dominant so the flow acts as a plume. This was the case in the third experiment at low Reynolds number (2640). However, if the flow rate is high, then the momentum is significant so the flow is a certain positive buoyant jet. This was the case in the fourth experiment at high Reynolds number (14000).

For temperature and velocity measurements on TABOULE; we were not able to apply 2c/2d LIF and PIV on all the cases as indicated in the experimental campaign. Their

application was possible in the case of single and two negative buoyant jets. For the analysis of the velocity field, the time average velocities along the centerline and the axial direction were plotted. For the analysis of the temperature field, the space moving average of the temperature along the centerline of the nozzle was plotted. In each case, the spread of the jets was studied. We notice that the temperature variation is steady along the height when compared to that of velocity which decreases rapidly due to the competition between momentum and buoyancy flux. Also, the LIF technique was applied on other four cases at different Reynolds and Froude numbers covering a range that allowed us to compare our results to those found in literature. However, the experiments were done between the partially saturated regime and the saturated regime. Also, the filters used did not avoid the spectral conflicts between FL27 and RhWT. That is why the results were biased. We also realized that the presence of striations is reduced when the temperature difference between the fluid and the surrounding is small. This can explain why the quality of the LIF image is better when this technique is used for a hydrodynamic study. In conclusion, the complexities in the experiments increase with the increase in the scale of the facility as we have to control and manage many parameters to get precised results. Although we managed to apply the simultaneous measurements of temperature and velocity by LIF and PIV on a complex geometry ($V= 1000 L$), the precision of the results was not high when compared to those performed on volumes less than $30 L$.

8.2 Perspectives

Many perspectives are opened as a result of the experimental approaches in this thesis and several elements could be studied to follow up this work. This will serve to improve the measurement accuracy and the appeal of 2c/2d LIF and PIV techniques in thermal studies in the laboratory. The elements are divided and explained according to the experimental campaigns realized.

The LIF technique was implemented for the first time. Some improvements could be carried out in order to take into account the accuracy of the measurements during the calibration step. This could be done by repeating the experimental tests several times.

For the study of hydrodynamics, several constraints are present. It is time consuming because of the large volume of the facility. The best approach would be to change the solution at each experiment. To be precised, the test section should be re-filled just with de-ionized water at the beginning of each experiment. Then, the same concentration of the dye should be added to the hot and cold tanks. This would definitely enhance the processing step of the images.

For the simultaneous application of 2c/2d LIF and PIV on TABOULE, several elements could be enhanced.

Regarding the LIF technique, the experiments need to be done in the saturated laser regime. This could be achieved either by increasing the laser energy or by decreasing the duration of the laser pulse in order to exceed the value of the of the saturation energy of the fluorescent dye. Another method is by decreasing the collection surface of measurements. Regarding the spectral conflicts between the two dyes chosen, an adequate filter should be chosen in a way to avoid the reabsorption of the FL27 and the overlap between the absorption of FL27 and emission of RhWT (using a high pass band filter at 650nm). There is also a need to find the adequate means to store the fluorescent dyes in a way the preserves their stability. Using three

identical cameras having the same resolution assures the matching (spatial calibration) between the field of views for each camera. This will also allow to increase the operating frequency during the experiments. For instance, we were obliged to perform these experiments at a frequency of 1 Hz. The field of view of the cameras can be enhanced by fabricating filters and mirrors that fit the objective of the cameras. However, this might be expensive. That is why technological developments are expected to be done in this domain, especially in what concerns the synchronization between the cameras and the laser. This will make the LIF technique a metrological tool as common and easy to use as the velocity measurement techniques PIV and LDV. In what concerns the treatment of images, it would be of fundamental interest to solve the problem of striations which will enhance the quality of the obtained LIF images. It is also of importance to state that the LIF technique is used to measure other scalars such as concentration or the density variation of fluid in its surrounding. In such measurements, the effect of striations due to the change in the refractive index is not present. This improves the quality of the images obtained by this method thus giving a high precision measurement. For future experimental campaigns on this facility, studies could be done to study the buoyancy effect of fluid flows since the plate of the nozzles can be moved and placed on the vertical wall of TABOULE.

References

- [1] Nuclear Reactors: Generation to Generation, American Academy written by SM Goldberg.
- [2] The nuclear fuel cycle, World Nuclear website updated in March 2017.
- [3] Nuclear reactors, Educational booklet by CEA, From fission to power generation.
- [4] Sodium cooled fast reactor (SFR) Technology and Safety Overview, Office of Nuclear Energy U.S. Department of Energy, February 18, 2015.
- [5] Fourth generation cooled fast reactors, the ASTRID technological demonstrator, Nuclear Energy Division (CEA), December 2012.
- [6] Plateau facility in support to ASTRID and the SFR program: an overview of the first mock-up of the astrid upper plenum, MICAS, D. Guénadou, I. Tkatchenko and P. Aubert, NURETH-16, 2015.
- [7] Review of temperature measurement P. R. N. Childs, J. R. Greenwood, and C. A. Long Thermo-Fluid Mechanics Research Centre, University of Sussex, Brighton, United Kingdom.
- [8] Mesure des températures - Questions à poser avant la mesure, article Mesures, Jacques ROGEZ, Jean LE COZE, March 2009.
- [9] Measurement of temperature field around a single steady vapor bubble using phase shift interferometry, Stoica, V. and P. Stephan, Archives of Thermodynamics,27:81–90, 2006.
- [10] Temperature Field Measurements with High Spatial and Temporal Resolution Using Liquid Crystal Thermography and Laser Induced Fluorescence, Thesis by Ralph Nasarek, 2010.
- [11] Molecular tagging velocimetry and thermometry and its application to the wake of a heated circular cylinder. Measurement Science Technology, Hui Hu and Manoochehr M Koochesfahani, Measurement Science and Technology, Volume 17, Number 6, 2006.
- [12] Numerical Simulation of Lasing Dynamics in Cholesteric Liquid Crystal Based on ADE-FDTD Method, Tatsunosuke Matsui, Numerical Simulations of Physical and Engineering Processes, 2011.
- [13] Simultaneous velocity and temperature measurements in turbulent Rayleigh-Bénard convection based on combined Tomo-PIV and PIT, Daniel Schiepel, Daniel Schmeling and Claus Wagner, The 18th International Symposium on Applications of Laser Techniques to Fluid Mechanics, 2016.

- [14] Laser-induced fluorescence as a method for measuring mass-transfer rates and for flow visualization, D. S. Nichols, C. H. Brown, Bulletin Of The American Physical Society, vol. 17, no. 11, p. 1091, 1972.
- [15] Laser velocimeter measurements of structure of turbulent spray flames, Owen, F. K., *Astronautics & Aeronautics*, vol. 15, no. 10, p. B19, 1977.
- [16] Laser-induced fluorescence measurements of mixed fluid concentration in a liquid plane shear layer, Koochesfahani, M. M. and Dimotakis, P. E, *AIAA Journal*, vol. 23, pp. 1700–1707, Nov. 1985.
- [17] A fluorescence technique for measurement of concentration in mixing liquids, Walker, D. A , *Journal of Physics E: Scientific Instruments*, vol. 20, pp. 217 - 224, 1987
- [18] Dual emission laser induced fluorescence for direct planar scalar behavior measurements, J. Coppeta, C. Rogers *Experiments in Fluids* 25, 1-15 1998.
- [19] Whole field measurements of temperature in water using two-color laser induced fluorescence, Sakakibara J, Adrian R, *Exp Fluids* 26:7–15, 1999.
- [20] Jablonski diagram, <https://www.med.unc.edu/microscopy/files/2018/06/jablonski-diagram.pdf>.
- [21] Combined PLIF and PIV technique for velocity and temperature field, K Hishida and J. Sakakibara *Experiments in Fluids* 29, 129-140 Springer-Verlag, 2000
- [22] Evaporating and combusting droplet temperature measurement using two colors laser induced fluorescence, Lavielle P, Lemoine F, Lebouche M, Lavergne G, *Exp Fluids* 31:45–55, 2001.
- [23] Instantaneous measurement of two-dimensional temperature distributions by means of two-color planar laser induced fluorescence (PLIF), Bruchhausen M, Guillard F, Lemoine F, *Exp Fluids* 38:123–131, 2005.
- [24] <http://www.bgu.ac.il/~glevi/website/Guides/Lasers.pdf>
- [25] Laser-induced fluorescence measurements of dual plumes and comparison of laser-induced fluorescence and conductivity probe measurements, Thesis by Joseph C. Chrzan, 2012.
- [26] Development of the planar laser-induced fluorescence for temperature measurements of evaporating spray, Thesis by G. Sgarigua, 2011.
- [27] Fluorescence induite par laser multibande appliquée à la mesure de température dans les milieux complexes, Thesis by Alain DELCONTE, 2009.
- [28] How Lasers Work by Lawrence Livermore National Security, LLC, for the Department of Energy’s National Nuclear Security Administration. https://lasers.llnl.gov/education/how_lasers_work

- [29] https://www.visiononline.org/userAssets/aiaUploads/file/CVP_The-Fundamentals-of-Camera-and-Image-Sensor-Technology_Jon-Chouinard.pdf.
- [30] <https://electronics.howstuffworks.com/cameras-photography/digital/question362.htm>.
- [31] <https://www.dantecdynamics.com/measurement-principles-of-piv>.
- [32] A laser-induced fluorescence measurement for aqueous fluid flows with improved temperature sensitivity. Experiments in fluids, Sutton, J. A., Fisher, B. T., & Fleming, J. W. 45(5), 869-881, 2008.
- [33] Investigation on YAG laser dyes for oil film thickness and temperature measurement, Saeki S, Hart DP, In Proceedings of the third pacific symposium of flow visualization and image processing, March 18–21, 2001.
- [34] A temperature sensitive tracer suitable for two-color laser-induced fluorescence thermometry applied to evaporating droplets, Depredurand V, Miron P, Labergue A, Wolff M, Castanet G, Lemoine F, Measurement Science and Technology, 2008, 19, pp.105403 - 105403.
- [35] Temperature measurements of binary droplets using three-color laser-induced fluorescence, Maqua C, Castanet G, Lemoine F, Doue' N, Lavergne G, Exp Fluids 40:786–797, 2006.
- [36] A two-color planar LIF technique to map the temperature of droplets impinging onto a heated wall, Pierre Dunand, Guillaume Castanet, Fabrice Lemoine, Experiments in Fluids, Springer Verlag (Germany), 52 (4), pp.843- 856, 2012.
- [37] New insight into two-color LIF thermometry applied to temperature, Alexandre Labergue, Alain Delconte, Fabrice Lemoine, 15th Int Symp on Applications of Laser Techniques to Fluid Mechanics Lisbon, Portugal, 05-08 July, 2010.
- [38] Planar laser induced fluorescence in aqueous flows. Experiments in fluids, Crimaldi, J. P, 4(6), 851-863, 2008.
- [39] Application of two color LIF for temperature mapping by H.J Kim and K.D. Kihm Texas university. <http://minsfet.utk.edu/publications/2001ASME-Proceedign-NYApplication.pdf>
- [40] Criteria for quantitative PLIF experiments using high-power lasers, Melton, L. A., & Lipp, C. W, Experiments in fluids, 35(4), 310-316, 2003.
- [41] An analysis of long term temperature measurement using laser induced fluorescence, M.Jaszczur et al, J.Physics, 2016.

- [42] Ratiometric, single-dye, pH-sensitive inhibited laser-induced fluorescence for the characterization of mixing and mass transfer, Lacassagne T, Simoëns S, El Hajem M, Champagne J-Y., *Exp. Fluids*,59:21, . 2018.
- [43] <http://www.thermopedia.com/content/1239>
- [44] https://velocimetry.net/ldv_principles.htm.
- [45] Particle image velocimetry using novel, non-intrusive particle seeding a thesis by Charles J. DeLapp, II, BS - Major, USAF in June 2006
- [46] Particle Image Velocimetry A Practical Guide, J Raffel, M., Willert, C.E., Wereley, S., Kompenhans, 1998.
- [47] “2D PIV reference manual.” D. D. A/S.
- [48] Principles and practice of laser-Doppler anemometry, A. M. and J. H. W. R. Durst, 2nd ed. Academic Press Inc, 1981.
- [49] Particle Image Velocimetry Zhang, Chen; Vasilevskis, Sandijs; Kozlowski, Bartosz, 2018
- [50] Tracer Particles & Seeding for Particle Image Velocimetry, Melling A., *Measurement Science Technology*, Vol 8: 1407-1416, 1997.
- [51] Statistical properties of particle image velocimetry measurements in turbulent flow, Adrian R.J., *Laser Anemometry in Fluid Mechanics III*, Springer-Verlag, Berlin Heidelberg : 115-129, 1988.
- [52] Theory of cross-correlation analysis of PIV images, Keane R.D., Adrian R. J., *Applied Science Res.*: 49: 191-215, 1992.
- [53] Experimental Study of Natural Convective Internal Flows, Thesis by Chiara Spaccapaniccia, 2016.
- [54] Particle Image Velocimetry: Fundamentals and Its Applications, Mohsen Jahanmiri; Research report, Division of Fluid Dynamics Department of Applied Mechanics, Chalmers university of technology, Göteborg, Sweden, 2011.
- [55] Combined PLIF-PIV technique for velocity and temperature fields. Hishida K, Sakakibara J, *exp fluids* 29:S129-S140, 2000.
- [56] Combined PIV/LIF measurements in a Rayleigh–Bénard convection cell, Petracci, R. Delfos, J. Westerweel, 13th International Symposium on Applications of Laser Techniques to Fluid Mechanics, 2006.
- [57] Simultaneous PIV/LIF measurements of a transitional buoyant plume above a horizontal cylinder Stig Grafsrønningen, Atle Jensen *International Journal of Heat and Mass Transfer* 55, 4195–4206, 2012.

- [58] Simultaneous temperature and 2D velocity measurements in a turbulent heated jet using combined laser-induced fluorescence and LDA F. Lemoine, Y. Antoine, M. Wolff, M. Lebouche *Experiments in Fluids* 26,315-323, 1999.
- [59] Experimental investigation into a turbulent jet with negative buoyancy R.W. Cresswell and R.T. Szczepura , 11 March 1992.
- [60] Turbulent jets and Plumes, ppt prepared by Monroe L. Weber-Shirk, School of Civil and Environmental Engineering, Cornell University.
- [61] <http://www.lth.se/fileadmin/tvrl/files/vvr176/lecture6.pdf>
- [62] On the physical significance of some dimensionless numbers used in heat transfer and fluid flow, Clovis R. Maliska, Computational Fluid Dynamics Laboratory-SINMEC
- [63] Summary of Dimensionless Numbers of Fluid Mechanics and Heat Transfer by Jingwei Zhu.
- [64] Note on the history of the Reynolds number, Rott, N, *Annual Review of Fluid Mechanics*. 22 (1): 1–11, 1990.
- [65] Shih, Merle C. Potter, Michigan State University, David C. Wiggert, Michigan State University, Bassem Ramadan, Kettering University ; with Tom I-P. (2012). *Mechanics of fluids* (Fourth edition. ed.). p. 105.
- [66] *Boundary-Layer Theory* by Hermann Schlichting and Klaus Gersten - Springer-Verlag 2017, pages 416–419.
- [67] <https://www.britannica.com/science/Richardson-number>.
- [68] Large eddy simulation of three-dimensional mixed convection on a vertical plate (PDF), Garbrecht, Oliver, RWTH Aachen University, August 2017.
- [69] Experimental studies in jet flows and zero pressure-gradient turbulent boundary layers by Ramis Orlu May 2009, Technical Reports from Royal Institute of Technology, KTH Mechanics SE-100 44 Stockholm, Sweden.
- [70] Course on turbulence by Joel Sommeria, Grenoble Alpes University, France, 2016.
- [71] Hussein, H. J., S. Capp, and W. K. George (1994). Velocity measurements in a high-Reynolds-number, momentum-conserving, axisymmetric, turbulent jet. *J. Fluid Mech.* 258, 31-75.
- [72] Wygnanski, I. and H. Fiedler (1969). Some measurements in the self-preserving jet. *J. Fluid Mech.* 38, 577-612.
- [73] *Turbulent flows* by Stephan B. Pope.

- [74] <http://www.dartmouth.edu/~cushman/books/EFM/chap9.pdf>
- [75] Negatively buoyant starting jets C. Marugán-Cruz,¹ Rodríguez-Rodríguez, and C. Martínez-Bazán Grupo de Mecánica de Fluidos, Universidad Carlos III de Madrid, 28911 Leganés, Spain ² Departamento de Ingeniería Mecánica y Minera, Área de Mecánica de Fluidos, Universidad de Jaén, Campus de las Lagunillas, 23071 Jaén, Spain
- [76] An Experimental Study of Vertical Turbulent Jet with Negative Buoyancy ; T. Mizushima, F. Ogino, H. Takeuchi, and H. Ikawa, Kyoto, Japan.
- [77] Turner, J. S.: Jets and plumes with negative or reversing buoyancy. *J. Fluid Mech.* 26 (1966) 779-792.
- [78] LDV Principle, Troolin D., University of Minnesota.
- [79] Seban, R. A.; Behnia, M. M.; Abreu, K. E.: Temperatures in a heated air jet discharged downward. *Int. J. Heat Mass Transfer* 21 (1978) 1453-1458.
- [80] Experimentelle und theoretische Untersuchungen fiber den Einflug der Schwerkraft auf anisotherme, turbulente Freistrahlen. *Haustechnik-BauphysikUmwelttechnik-Gesundheits-Ingenieur,Fleischhacker, G.; Schneider, W*, 101 (1980) 129-140.
- [81] Investigation And Application Of Multistage Hydrajet-fracturing In Oil And Gas Well Stimulation In China, by Li Gensheng, Huang Zhongwei, Tian Shouceng, Niu Jilei, Qu Hai, SPE, and Sheng Mao, China University of Petroleum, Beijing
- [82] The mixing transition in turbulent flows by PAUL E. DIMOTAKIS; Graduate Aeronautical Laboratories, California Institute of Technology, Pasadena, CA 91125, USA
- [83] Dynamic interaction of multiple buoyant jets Adrian C. H. Lai and Joseph H. W. Lee, *Journal of fluid mechanics*, V. 708, 2012.
- [84] Large-eddy simulation of thermal striping in WAJECO and PLAJEST experiments with triocfd, Pierre-emmanuel Angeli, NURETH-16, Chicago, August 30-September 4, 2015.
- [85] Proposal of benchmark problem of thermal striping phenomena in planar triple parallel jets tests for fundamental code validation in sodium-cooled fast reactor development, J. Kobayash et al., NURETH-16, Chicago, August 30-September 4, 2015.
- [86] Study on Thermal Striping Phenomena in Triple-Parallel Jet - Transfer Characteristics of Temperature Fluctuation in Sodium and Water based on Conjugated Numerical Simulation, N. Kimura, H. Kamide, P. Emonot and K. Nagasawa, Proc. of NUTHOS-7, Seoul, Korea, October 5-9, 2008.

- [87] Mixing in coaxial jets by E. Villermaux and H. Rehab. mixing in coaxial jets by E. Villermaux and H. Rehab, *Journal of Fluid Mechanics*, 425:161 - 185, December 2000.
- [88] Fluorescence Worskshop, Quenching and FRET by Joachim Mueller, 2006.
- [89] Heat and mass transfer in a system of plane turbulent jets with diffusion combustion F. Aliev, *Journal of Fluid dynamics*, Vol 3, No 2.
- [90] Mixing enhancement in coaxial jets through inflow forcing: A numerical study, Guillaume Balarac, Olivier Metais, LEGI Grenoble, *Physics of Fluids* 19, 075102 (2007).
- [91] Characterization of mixing in a stirred tank by planar laser induced fluorescence PLIF, A. Fall, O. Lecoq and R. David, *Chemical Engineering Research and Design* Volume 79, Issue 8, November 2001.
- [92] Measurement of mixing processes with combined digital particle image velocimetry and planar laser induced Fluorescence Adrian Wing-Keung Law, Hongwei Wang, *Experimental Thermal and Fluid Science*, 22(3):213-229 · September 2000.
- [93] PLIF and PIV measurements of the self-preserving structure of steady round buoyant turbulent plumes in crossflow, *International Journal of Heat and Fluid Flow* 26 (2005) 873–882.
- [94] Vortex structure and heat transfer in the stagnation region of an impinging plane jet (simultaneous measurements of velocity and temperature fields by digital particle image velocimetry and laser-induced fluorescence), Jun Sakakibara, Koichi Hishidat and Masanobu Maeda, *International Journal of Heat and Mass Transfer*, 40(13), 3163-3176, 1997.
- [95] Some thermal hydraulic challenges in sodium cooled fast reactors D. Tenchine CEA/DEN, CEA Grenoble, France, *Nuclear Engineering and Design*; Journal Volume: 240; Journal Issue: 5, 2010.
- [96] Analysis and comparison of experimental data generated using PIV and UVP in mixing of parallel two jets, Saya Lee, Arturo Carbal and Yasin Hassan. NUTHOS-11: The 11th International Topical Meeting on Nuclear Reactor Thermal Hydraulics, Operation and Safety Gyeongju, Korea, October 9-13, 2016.
- [97] Experimental Study of Free Surface Mixing in Vortical and Chaotic Flows, Thesis by J. M. Garcia de la Cruz Lopez, 2011.
- [98] Application of fluorescent particles for particle tracking velocimetry in wind tunnels Tamara Guimarães¹, K. Todd Lowe¹ 18th International Symposium on the Application of Laser and Imaging Techniques to Fluid Mechanics, Lisbon, Portugal, July 4 – 7, 2016

- [99] Entrainment Models for Laminar Jets, Plumes, and Wakes B. R. Morton
Citation: *Phys. Fluids* 10, 2120 (1967).
- [100] An Experimental Study of Vertical Turbulent Jet with Negative Buoyancy T. Mizushima, F. Ogino, H. Takeuchi, and H. Ikawa, Kyoto, Japan, *Wärme- und Stoffübertragung* 16, 15–21, 1982.
- [101] Investigations of round vertical turbulent jets by Panos and John List, *Journal fluid mechanics*, vol 195, pp 341, 1988.
- [102] Experimental investigation into a turbulent jet with negative buoyancy R.W Cresswell; Center for Dynamical Meteorology, Monash University, Clayton, Victoria 3168, Australia.
- [103] Jets and plumes with negative or reversing buoyancy by J.S.Turner; *Journal fluid mechanics*, vol 26, pp 779-792, 1966.
- [104] Metrologie Laser pour la mecanique des fluides, *Mécanique et ingénierie des matériaux*, Alain Boutier, 2012.
- [105] Velocimetrie Laser pour la mecanique des fluides, *Mécanique et ingénierie des matériaux*, Alain Boutier, 2012.
- [106] Mesures de caracteristiques d'écoulement par imagerie numerique, Dynamique des traceurs dans un écoulement; Jean-Paul SCHON, Thierry FOURNEL, Corinne FOURNIER, Septembre 2007.
- [107] Tracer particles and seeding for particle image velocimetry; Lehrstuhl für Stromungsmechanik, Universität Erlangen-Nürnberg, Cauerstrasse 4, D-91058 Erlangen, Germany; October 1997.
- [108] Turbulent entrainment in jets with arbitrary buoyancy, Edouard Kaminski, Stephen Tait and Guillaume Carazzo, *Journal of fluid mechanics*, February 2005.
- [109] Transient positively and negatively buoyant turbulent round jets L. Pantzlaß, R. M. Lueptow; *Experiments in Fluids* 27, 117-125, 1999.
- [110] General aspects of luminescence spectroscopy, Guilbault, G.G. Ed. , *Practical Fluorescence*. Marcel Dekker, NY, pp. 1–40, 1990.
- [111] Errors in thermochromic liquid crystal thermometry, Roland Wiberga, *Review of scientific instruments*, volume 75, number 9, September 2004.
- [112] New insight into two-color LIF thermometry applied to temperature measurements of droplets Alexandre Labergue, Valérie Deprédurand, Alain Delconte, Guillaume Castanet, Fabrice Lemoine, *Experiments in Fluids*, Springer Verlag (Germany), 2010, 49 (2), pp.547 - 556.

- [113] Transferts de chaleur et de masse lors de l'impact d'une goutte sur une paroi chaude en régime d'ébullition en film - Application de diagnostics optiques et modélisation, Thesis by William Chaze, 2017.
- [114] The saturation of the fluorescence and its consequences for laser-induced fluorescence thermometry in liquid flows, William Chaze, Ophélie Caballina, Guillaume Castanet, Fabrice Lemoine, Experiments in Fluids, Springer Verlag (Germany), 2016, 57 (4), pp.217 - 217.
- [115] Environmental fluid mechanics, turbulent jets, Benoit Cushman-Roisin Thayer School of Engineering, Dartmouth College.
- [116] Impact of buoyancy on urban heat removal at a local scale: a time-resolved PIV-LIF study in a water tunnel, Shah Jigar, Allegrini Jonas, Carmeliet Jan, 18th International Symposium on Flow Visualization Zurich, Switzerland, June 26-29, 2018.
- [117] Review of fluorescent standards for calibration of in situ fluorometers: Recommendations applied in coastal and ocean observing programs, Earp, Alan & Hanson, Christine & Ralph, Peter & Brando, Vittorio & Allen, Simon & Baird, Mark & Clementson, Lesley & Daniel, Paul & Dekker, Arnold & Fearn, Peter & Parslow, John & Strutton, Peter & Thompson, Peter & Underwood, Mark & Weeks, S. & Doblin, Martina., 2011.
- [118] Turbulent fountains in an open chamber, Baines, W. D., Turner, J. S. & Campbell, I. H., Journal of Fluid. Mechanics 212, 557-592, 1990.
- [119] Virtual origin correction for lazy turbulent plumes, Hunt, G. R. & Kaye, N. G. 2001, Journal of Fluid. Mechanics. 435, 377-396.
- [120] Experimental Studies of Two-Phase Negatively Buoyant Plumes By Timothy H. Harrison, June 2001.
- [121] Direct simulation of fountains with intermediate froude and reynolds numbers, Lin, W. and Armfield, S. W. ANZIAM J.45, C66-77, 2004.
- [122] Toxicity of fluorescent tracers and their degradation byproducts, Gombert P., Pandard P., International Journal of Speleology, January 2017.
- [123] Introduction à la turbulence, Olivier Cadot, Introduction à la turbulence, ENSTA-ParisTech, France, 2013.